nature geoscience

SUPPLEMENTARY INFORMATION

https://doi.org/10.1038/s41561-020-0536-y

In the format provided by the authors and unedited.

Constraints on the shallow elastic and anelastic structure of Mars from InSight seismic data

P. Lognonné[1,2]✉, W. B. Banerdt[3], W. T. Pike[4], D. Giardini[5], U. Christensen[6], R. F. Garcia[7], T. Kawamura[1], S. Kedar[3], B. Knapmeyer-Endrun[8], L. Margerin[9], F. Nimmo[10], M. Panning[3], B. Tauzin[11], J.-R. Scholz[6], D. Antonangeli[12], S. Barkaoui[1], E. Beucler[13], F. Bissig[5], N. Brinkman[5], M. Calvet[9], S. Ceylan[5], C. Charalambous[4], P. Davis[14], M. van Driel[5], M. Drilleau[1], L. Fayon[15], R. Joshi[6], B. Kenda[1], A. Khan[5,16], M. Knapmeyer[17], V. Lekic[18], J. McClean[4], D. Mimoun[7], N. Murdoch[7], L. Pan[11], C. Perrin[1], B. Pinot[7], L. Pou[10], S. Menina[1], S. Rodriguez[1,2], C. Schmelzbach[5], N. Schmerr[18], D. Sollberger[5], A. Spiga[2,19], S. Stähler[5], A. Stott[4], E. Stutzmann[1], S. Tharimena[3], R. Widmer-Schnidrig[20], F. Andersson[5], V. Ansan[13], C. Beghein[14], M. Böse[5], E. Bozdag[21], J. Clinton[5], I. Daubar[3], P. Delage[22], N. Fuji[1], M. Golombek[3], M. Grott[17], A. Horleston[23], K. Hurst[3], J. Irving[24], A. Jacob[1], J. Knollenberg[17], S. Krasner[3], C. Krause[17], R. Lorenz[25], C. Michaut[2,26], R. Myhill[23], T. Nissen-Meyer[27], J. ten Pierick[5], A.-C. Plesa[17], C. Quantin-Nataf[11], J. Robertsson[5], L. Rochas[28], M. Schimmel[29], S. Smrekar[3], T. Spohn[17,30], N. Teanby[23], J. Tromp[24], J. Vallade[28], N. Verdier[28], C. Vrettos[31], R. Weber[32], D. Banfield[33], E. Barrett[3], M. Bierwirth[6], S. Calcutt[34], N. Compaire[7], C.L. Johnson[35,36], D. Mance[5], F. Euchner[5], L. Kerjean[28], G. Mainsant[7], A. Mocquet[13], J. A Rodriguez Manfredi[37], G. Pont[28], P. Laudet[28], T. Nebut[1], S. de Raucourt[1], O. Robert[1], C. T. Russell[14], A. Sylvestre-Baron[28], S. Tillier[1], T. Warren[38], M. Wieczorek[39], C. Yana[28] and P. Zweifel[5]

[1]Université de Paris, Institut de Physique du Globe de Paris, CNRS, Paris, France. [2]Institut Universitaire de France, Paris, France. [3]Jet Propulsion Laboratory, California Institute of Technology, Pasadena, CA, USA. [4]Department of Electrical and Electronic Engineering, Imperial College London, London, UK. [5]Institute of Geophysics, ETH Zurich, Zurich, Switzerland. [6]Max Planck Institute for Solar System Research, Göttingen, Germany. [7]Institut Supérieur de l'Aéronautique et de l'Espace—SUPAERO, Toulouse, France. [8]Bensberg Observatory, University of Cologne, Bergisch Gladbach, Germany. [9]Institut de Recherche en Astrophysique et Planétologie, Université Toulouse III Paul Sabatier, CNRS, CNES, Toulouse, France. [10]Department of Earth and Planetary Sciences, University of California Santa Cruz, Santa Cruz, CA, USA. [11]Université de Lyon, Université Claude Bernard Lyon 1, ENS, CNRS, Laboratoire de Géologie de Lyon—Terre, Planètes, Environnement, Villeurbanne, France. [12]Sorbonne Université, Muséum National d'Histoire Naturelle, UMR CNRS 7590, Institut de Minéralogie, de Physique des Matériaux et de Cosmochimie, IMPMC, Paris, France. [13]Laboratoire de Planétologie et Géodynamique, UMR6112, Université de Nantes, Université dAngers, CNRS, Nantes, France. [14]Department of Earth, Planetary, and Space Sciences, University of California, Los Angeles, CA, USA. [15]Space Exploration Institute, Neuchâtel, Switzerland. [16]Institute of Theoretical Physics, University of Zürich, Zürich, Switzerland. [17]DLR Institute of Planetary Research, Berlin, Germany. [18]Department of Geology, University of Maryland, College Park, College Park, MD, USA. [19]Laboratoire de Météorologie Dynamique/Institut Pierre Simon Laplace (LMD/IPSL), Sorbonne Université, Centre National de la Recherche Scientifique (CNRS), École Polytechnique, École Normale Supérieure (ENS), Paris, France. [20]Black Forest Observatory, Stuttgart University, Wolfach, Germany. [21]Department of Geophysics, Colorado School of Mines, Golden, USA. [22]Ecole des Ponts ParisTech, Laboratoire Navier/CERMES, CNRS, Marne la Vallée, France. [23]School of Earth Sciences, University of Bristol, Bristol, UK. [24]Department of Geosciences,Princeton University, Princeton, NJ, USA. [25]Johns Hopkins Applied Physics Laboratory, Laurel, MD, USA. [26]Université de Lyon, École Normale Supérieure de Lyon, UCBL, CNRS, Laboratoire de Géologie de Lyon—Terre, Planètes, Environnement, Lyon, France. [27]Department of Earth Sciences, University of Oxford, Oxford, UK. [28]Centre National d'Etudes Spatiales, Toulouse, France. [29]Institute of Earth Sciences Jaume Almera (ICTJA), Barcelona, Spain. [30]International Space Science Institute, Bern, Switzerland. [31]Division of Soil Mechanics and Foundation Engineering, Technical University of Kaiserslautern, Kaiserslautern, Germany. [32]NASA MSFC, NSSTC, Huntsville, AL, USA. [33]Cornell Center for Astrophysics and Planetary Science, Cornell University, Ithaca, NY, USA. [34]Department of Physics, University of Oxford, Oxford, UK. [35]Department of Earth, Ocean and Atmospheric Sciences, University of British Columbia, Vancouver, BC, Canada. [36]Planetary Science Institute, Tucson, AZ, USA. [37]Centro de Astrobiologia—Instituto Nacional de Tecnica Aeroespacial, Torrejón de Ardoz, Spain. [38]Atmospheric, Oceanic and Planetary Physics, University of Oxford, Oxford, UK. [39]Université Côte d'Azur, Observatoire de la Côte d'Azur, Laboratoire Lagrange, CNRS, Nice, France. ✉e-mail: lognonne@ipgp.fr

Constraints on the shallow elastic and anelastic structure of Mars from InSight seismic data

Supplement Materials

Supplement Material Section S1: Environmental Sensitivity of SEIS (16 pages)

Supplement Materlal Section S2: Subsurface (14 pages)

Supplement Material Section S3: Scattering and attenuation (14 pages)

Supplement Material Section S4: Receiver Function analysis (20 pages)

Supplement Material section S5: Glitches in SEIS' time series data (10 pages)

Supplement Tables: 3 set of Tables (15 pages)

Supplement S1: Environmental Sensitivity of SEIS

W.T.Pike , P.Lognonné, C. Charalambous, R.F. Garcia, A.E. Stott, J.B McClean, D.Mimoun, S.Ceylan, C.Perrin, L.Pou, S.Barkaoui, E.Stutzmann, M.Schimmel , A.Spiga, D.Banfield.

The signal from SEIS[1] contains contributions from the environment as well as seismic signals from the planet. Environmental signals are injected through instrument sensitivity to aseismic sources such as the temperature and magnetic sensitivities of the sensors as well as atmospheric wind and pressure forcing, either on the WTS, the lander or directly on the surface, transmitted to motion of the ground under SEIS. See [2] for a complete noise model of the instrument and [1] for the sensor noise. To validate a signal from the seismometers as being of seismic origin, it is necessary to quantify as well as possible the environmental injection and InSight includes the APSS payload, incorporating wind (through TWINS) and pressure sensors on the lander [Spiga et al., this volume]. In this supplement we describe the environmental and seismic signals over a typical sol, quantify the injection, first for the most important wind and pressure injection, and then for diurnal temperature changes, and illustrate how we determine the seismically distinct nature of three significant events for inclusion in a Mars seismic catalog.

We illustrate the environmental injection into SEIS over a complete diurnal period, sol 194-195. ***Figure 1*** of the main paper shows spectrograms of the three axes of seismic data for this period, covering from the bottom of the seismic detection bandwidth at 0.1 Hz to 50 Hz Nyquist of our sampling. ***Figure S1-1*** shows the polarization over the same period. There are clear differences between the polarization at low frequencies (0.03-0.3 Hz) and high frequencies (0.3-0.99 Hz). These differences are less visible between 17:00 and 00:00 LMST. The majority of the ground motion recorded by SEIS is attributable to wind and pressure, with the main sources being the lander vibrations induced by the wind[6-7] as previously observed on Viking[8,9] and the elastic response of the ground to atmospheric pressure variations[10-14]. Unlike Viking, InSight removes the direct wind forcing with the WTS. The weather on sol 194-5 is typical of early spring conditions at the InSight landing site in Elysium Planitia (see Banfield et al., this volume). The ambient wind direction is from the south, with a component from the west during the night and from the east during the day. The ambient wind speed is below 4 m/s at night and 6-8 m/s during the day. The diurnal variability of pressure is dominated by large-scale thermal tides that have a negligible seismic signal. The pressure signal with this large-scale component detrended shows a typical three-regime diurnal cycle: intense convective turbulence in the daytime (08:00-17:00 LMST); a quiet period (17:00-00:00 LMST) after sunset of low wind speed, most of the time below the TWINS sensor's detection threshold, when Mars is quiet enough to reveal the VBB instrument self-noise[1] and allow the detection of low amplitude events [Giardini et al, this volume]; and, following a transition in wind direction (17:00-19:00 LMST), a night time regime with gravity waves and small-amplitude shear-driven turbulence (19:00-07:00 LMST). Several characteristic pressure drops deeper than 1 Pa

are found in daytime, associated with dust-devil-like convective vortices, one of which has a characteristic pressure drop of 2 Pa and corresponds to a maximum wind speed of 18 m/s. The night time variability of pressure is dominated by low amplitude gravity-wave-like fluctuations with typical periods close to 1000 seconds. Wind gustiness in the night time is about six to eight times less than in the daytime; gusts of about 4 m/s can be witnessed in local times 13:00 to 14:00 LMST, without a clear origin. The transition times between these three SEIS noise regimes vary on a seasonal timescale. Occasionally new regimes emerge such as the appearance, from sol 190 onwards, of an additional quiet period around 06:00 LMST.

The wind excites a number of elastic resonances of the lander, visible as continuous narrowband noise at frequencies above 1 Hz. The modes were also observed, at much larger amplitudes, on the deck by the SP. The modes show variations, of different amplitudes, in their frequencies that are driven by the diurnal temperature variation. This temperature variation, together with the wind excitation, can be used to discriminate between lander and ground-related signals. For periods when environmental injection is minimal, the evolution of the vertical seismic noise over the sol is notably different from that seen on Earth. From 18:00-24:00 LMST the deglitched VBBZ noise falls regularly to a floor of 2×10^{-10} m/s^2/Hz$^{1/2}$ and occasionally 1×10^{-10} m/s^2/Hz$^{1/2}$ (***Figure 2***, main text). The vertical noise however increases with environmental activity and exceeds the noise of the horizontal components during the daytime. Also notable are the coherencies between the VBB axes, even at very low acceleration levels. Such behaviour has been observed in ocean bottom seismometers associated with tilts due to imperfect installation[15]. For InSight, we believe that these tilts are acting on the LVL system, either due to ground deformations generated by the lander or by tilts generated by the tether. The polarization of the seismic signal seen in ***Figure S1-1*** reflects the relative forcing on each axis.

Environmental injection is quantified in terms of coherence and comodulation at low and high frequencies. At low frequencies, partial coherence is observed between the seismic and pressure signals due to the elastic ground deformations[10-13]. However, only large pressure variations such as convective vortices during the day and long period gravity waves in the evening and at night produce ground displacements discernible from other contributions. The coherence between the seismic and pressure signals is plotted in ***Figure S1-2*** and is noticeably higher during the more active day. ***Figure S1-3*** shows in more detail the average coherence between the pressure and seismic signals at various local times. From 09:10 LMST to 16:15 LMST, convective vortices inject coherently into the vertical and horizontal components. The vertical coherence falls off below 0.03 Hz as other contributions dominate, while pressure-induced ground tilt maintains coherence for the horizontal axes[16]. ***Figure S1-4*** shows the SEIS background signal evolution as a function of the square of the wind speed, thus quantifying the statistical wind noise injection associated to wind stress and drag for low wind regime. A high frequency component, above 0.2 Hz, varying as a function of frequency f, is likely induced by wind drag effects acting on the lander. It is stronger on the vertical component than on the

horizontal ones, as predicted[6]. At frequencies lower than 0.1 Hz, lander wind drag model is predicting a tilt effect on the horizontal components, varying as 1/f, which is also observed. The noise source on the vertical component below 0.1 Hz is probably related to wind, but not yet completely understood. The noise is clearly rising as v^2 at high frequency, where v is the wind amplitude, but might only increase with wind speed at long period.

At higher frequencies, including the bandwidth for seismic detection, there is very little coherence between the wind or pressure and the seismic signals. While phase information is lost as overlapping contributions from various sources are combined, the energy of the seismic and pressure signals and the magnitude of the wind speed are strongly related. The seismic acceleration and pressure energy are quantified as the variance of their signal amplitudes over the bandwidth of interest. We characterise this comodulation relationship of seismic and pressure signal energy and wind speed in ***Figure S1-5***. The upper panel shows the variation over the sol of the seismic energy from 0.1 to 0.95 Hz, the pressure energy in the same frequency band, and the wind speed sampled at up to 1 Hz. The means and variances of the three signals have been matched over the entire sol. Inset are the covariation at less and more active periods of the sol. In the lower three panels, the relationships between the energies in the seismic and pressure signals and the wind speed are plotted, colour coded to allow matching to the time in the sol. A lower threshold is expected for the wind measurement of about 2.8 m/s, below which the output is not reliable. This is evident in both the seismic and pressure relationships as is a hysteresis with the wind showing a different sensitivity through the sol, diverging in the morning and evening. Seismic energy scales roughly as wind to the square, thus suggesting an atmospheric drag source for these seismic vibrations. We use the commodulation general relationship established here for the sol to quantify the injection for potential seismic events, but restrict the matching to a shorter window to avoid hysteresis.

Figure S1-6 shows the temperature variations of the subsystems of SEIS over this period. Thermal shielding[2] is effective in mitigating direct injection of diurnal temperature variations into the seismic band, above 0.01 Hz for the VBB and above 0.1 Hz for the SP. The temperature-induced drift below the seismic band is nevertheless much larger than in terrestrial deployments, even after activation of the VBBs' temperature compensation devices to prevent saturation. Despite the large temperature range of operation, all seismic sensors are operating continuously at high gain on all velocity and position outputs. At long period, temperature decorrelation has been performed, providing a 20 dB attenuation of the diurnal variation (***Figure S1-7***).

Glitches are observed regularly, likely associated to sensor's proof mass step-like displacement and/or SEIS assembly step like tilts. They are likely associated to the periodic release of stress built up from thermal mismatch in the SEIS support structure and sensors themselves and are injected into the output of a subset of the VBB and SP sensors. The sensors affected depends on the location of the stress release, with the glitches seen as broad-band features mainly below 1 Hz, but extending in some cases to

higher frequencies. Such glitches were common on Apollo's lunar seismometer, particularly at sunset and sunrise, driven by the large diurnal temperature cycling of the instrument. Supplement 5 discusses these glitches in more detail, as well as methodologies to remove them. Two catalogues of glitches during sol 194-5 are provided: table S5-1 using the identification techniques of MQS (17, Giardini et al., 2019), and table S5-2 using a machine learning algorithm[18].

In addition to the dominant atmospheric and temperature effects, several other features are visible in the spectrograms shown in ***Figure 1*** of the main text. The most prominent is the falling chirp seen from 21:00 UTC, which is an electronics artefact, with other examples at 06:05 UTC and 07:40 UTC. Clock noise is also visible at integer frequencies of the sampling rate of the HK temperatures in the spectrogram, with amplitudes in the time domain below the background noise. This noise is due to interference on the tether line, and readily removable with signal processing. Other features seen, though not in this sol, include IDA movements, UHF transmissions, and HP3 activities such as hammering. No significant magnetic noise has also been identified so far.

The environmental injection can be assessed for the strongest events (S0128, S0173 and S0235).

For the two long period events S0173 and S0235, a first step can be made by comparing the spectra of these events with the apriori wind noise as obtained from the statistical analysis shown in S1-4. This is summarized in ***Fig S1-8***, which confirms the high signal to noise ratio of S0173 and S0235 in the bandwidth 0.2-1 Hz.

For all three events and more in detail, the injection is quantified by matching the mean and variance of the pressure and seismic energy in the event bandwidth together with the wind speed, limiting the matching window to one hour's duration. This window length minimises the hysteresis seen in the wind signal over the full sol. Identification of a potential event as of seismic rather than environmental origin requires that the seismic signal is clearly distinguishable from these two environmental injections. S0128 high frequency event is shown in ***Figure S1-9*** for both the VBBs and SPs, in addition to the APSS records. S0128 occurred during the more active period with a mean wind speed of 4.6 m/s. Wind and pressure injection is the dominant contribution up to 09:34 LMST after which the seismic energy diverges from the environmental signals, indicating that the signal source was not due to environmental injection. The excellent match of the signals above the SP's higher noise floor at lower frequencies demonstrates that aseismic sensitivity at the instrument level is well below signal levels for both the VBB and the SP. See figure caption for full details. ***Figure S1-10*** shows S0173 event. The wind speed was lower and steady at 4 m/s, with some higher amplitude pulses. Pressure was also generally steady, with some periods of a few minutes of higher variance. The seismic signal shows several glitches, short duration excursions with different amplitudes on each axis, and the longer duration seismic event with arrivals at 02:23 and 02:26 LMST.

Although the noise in this bandwidth is considerably higher on the SP, it is able to co-detect the event at the higher signal energies. ***Figure S1-11*** shows S0235 event. The wind was below the threshold for reliable determination, and the pressure shows very little variance. The event is distinct from 12:19 LMST, and is again co-detected on the SP above a higher background. For all three events, the seismic energy is significantly above the environmental injection validating a non-local source for the seismic signal, and the phase picks as marked on each figure are uncontaminated by wind or pressure energy. Hence we have confidence that these events can be included in a seismic catalog of Mars.

References

[1] Lognonné, P., Banerdt, W. B., Giardini, D., Pike, W. T., Christensen, U., et al. (2019). SEIS: Insight's seismic experiment for internal structure of Mars. *Space Science Reviews*, *215*(1), 12.

[2] Mimoun, D., Murdoch, N., Lognonné, P., Hurst, K., Pike, W. T., Hurley, J., ... & SEIS Team. (2017). The noise model of the SEIS seismometer of the InSight mission to Mars. *Space Science Reviews*, *211*(1-4), 383-428.

[3] Schimmel, M., & Gallart J., (2003). The use of instantaneous polarization attributes for seismic signal detection and image enhancement, *Geophysical Journal International*, *155*(2), 653–668.

[4] Schimmel, M., Stutzmann E., Ardhuin F., & Gallart J., (2011). Polarized Earth's ambient microseismic noise, *Geochemistry, Geophysics, Geosystems*, *12*(7), Q07014.

[5] Stockwell, R. G., L. Mansinha, & R. P. Lowe, (1996). Localization of the complex spectrum: The S transform, *IEEE Transactions on Signal Processing, 44*(4), 998–1001.

[6] Murdoch, N., Mimoun, D., Garcia, R. F., Rapin, W., Kawamura, T., Lognonné, P., ... & Banerdt, W. B. (2017). Evaluating the wind-induced mechanical noise on the InSight seismometers. *Space Science Reviews*, *211*(1-4), 429-455.

[7] Murdoch, N., Alazard, D., Knapmeyer-Endrun, B., Teanby, N. A., & Myhill, R. (2018). Flexible mode modelling of the InSight lander and consequences for the SEIS instrument. *Space Science Reviews*, *214*(8), 117.

[8] D. L. Anderson, F. K. Duennebier, G. V. Latham, M. F. Toksöz, R. L. Kovach, T. C. Knight, A. R. Lazarewicz, W. F. Miller, Y. Nakamura, and G. Sutton. (1976). The Viking seismic experiment. *Science*, *194*(4271), 1318-1321

[9] Lorenz, R., Nakamura Y., & Murphy J., (2017). Viking-2 Seismometer Measurements on Mars: PDS Data Archive and Meteorological Applications, *Earth Space Science, 4(11), 681-688*

[10] Sorrells, G. G. (1971). A preliminary investigation into the relationship between long-period seismic noise and local fluctuations in the atmospheric pressure field. *Geophysical Journal International*, *26*(1-4), 71-82.

[11] Sorrells, G. G., McDonald, J. A., Der, Z. A., & Herrin, E. (1971). Earth motion caused by local atmospheric pressure changes. *Geophysical Journal International*, *26*(1-4), 83-98.

[12] Murdoch, N., Kenda, B., Kawamura, T., Spiga, A., Lognonné, P., Mimoun, D., & Banerdt, W. B. (2017). Estimations of the seismic pressure noise on Mars determined from Large Eddy Simulations and demonstration of pressure decorrelation techniques for the InSight mission. *Space Science Reviews*, *211*(1-4), 457-483.
[13] Kenda, B., Lognonné, P., Spiga, A., Kawamura, T., Kedar, S., Banerdt, W. B., ... & Golombek, M., (2017). Modeling of ground deformation and shallow surface waves generated by Martian dust devils and perspectives for near-surface structure inversion. *Space Science Reviews*, *211*(1-4), 501-524.
[14] Spiga, A., Banfield, D., Teanby, N. A., Forget, F., Lucas, A., Kenda, B., ... & Garcia, R. F. (2018). Atmospheric science with InSight. *Space Science Reviews*, *214*(7), 109.
[15] Pillet, R., Deschamps A., Legrand D., Virieux J., Béthoux N., & Yates B., (2009). Interpretation of Broadband Ocean-Bottom Seismometer Horizontal Data Seismic Background Noise, *Bulletin of the Seismological Society of America*, *99*(2B), 1333–1342.
[16] Garcia et al., Pressure effects on SEIS-INSIGHT instrument, improvement of seismic records and characterization of long period atmospheric waves from ground displacements, (in preparation)
[17] Clinton, J., Giardini, D., Böse, M., S. Ceylan, M. van Driel, F. Euchner, R. F. Garcia, S. Kedar, A. Khan, S. C. Stähler, B. Banerdt, P. Lognonne, E. Beucler, I. Daubar, M. Drilleau, M. Golombek, T. Kawamura, M. Knapmeyer, B. Knapmeyer-Endrun, D. Mimoun, A. Mocquet, M. Panning, C. Perrin, N. A. Teanby, The Marsquake Service: Securing Daily Analysis of SEIS Data and Building the Martian Seismicity Catalogue for InSight, Space Sci Rev (2018) 214: 133. https://doi.org/10.1007/s11214-018-0567-5
[18] Barkaoui, S., Lognonné, P., Dehoop M., Drilleau M., Kawamura T., Stutzmann E., van Driel m., Kenda, B., Sainton G., Seydoux L., Clinton J., Schimmel M. and Naomi Murdoch, Unsupervised representation learning for clustering SEIS data in continuous records with deep scattering network (in preparation).

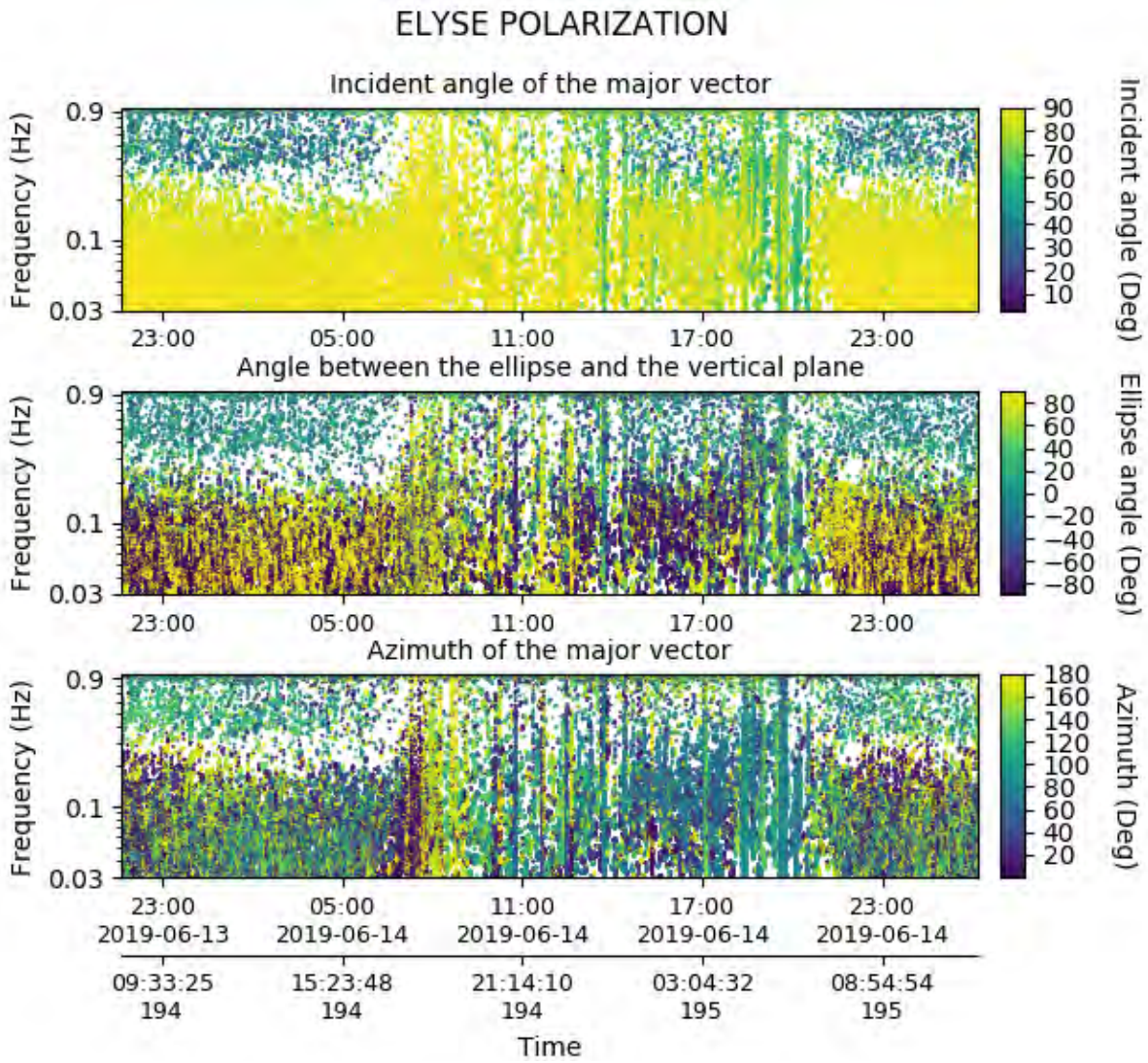

Figure S1-1: Polarization of the VBB broadband signal recorded for sol 194 - 195 (UTC time 2019/06/13 21:59:54.8 to 2019/06/15 02:00:02.0) as a function of time and frequency. Station Name of the SEIS instrument is ELYSE, in reference to its landing site (Elysium Planitia). The upper time axis is in UTC and the bottom axis is in LMST. To examine the polarization of the seismic signal, we construct the cross-spectral matrices from the time-frequency representation of the three-component VBB seismograms and perform eigen analysis of these matrices[3,4]. We then consider the major and minor vectors of the ellipse that best fits the ground motion. In order to select only robust polarization measurements, we use the instantaneous degree of polarization (DOP) which is an instantaneous quality measure based on the stability of an arbitrary polarization state with time[5].

On all 3 panels, there is a clear difference in the polarization between the low frequency band 0.03-0.3 Hz (LF) and the high frequency band 0.3-0.99 Hz (HF). These differences are less visible between 17:00 and 00:00 LMST. The top panel shows the incident angle of the ellipse major axis with respect to the vertical. This angle is close to 90 deg for the LF band which means that the ellipse major axis is horizontal. In the HF band, the angle is between 30 to 50 deg, so the major axis is inclined with respect to the vertical axis. Between 17:00 and 00:00 LMST, the ellipse major axis is mostly close to horizontal in the entire frequency band.

The middle panel shows the angle between the ellipse plane and the vertical plane. In the HF band, this angle is close to 0, which means that the polarization ellipse is in the vertical plane. On

contrary, in the LF band, the angle is close to either +90 deg or -90 deg, so the ellipse is in the horizontal plane, with a motion that is either clock-wise or anti clock-wise.
The bottom panel shows the azimuth of the ellipse major axis. In the HF band, except between 17:00 and 00:00 LMST, the azimuth is 100-140 deg (+-180 deg). In the LF band, we observe variations of the azimuth as a function of local hour. Similar azimuths variations as a function of local hour are observed every days.

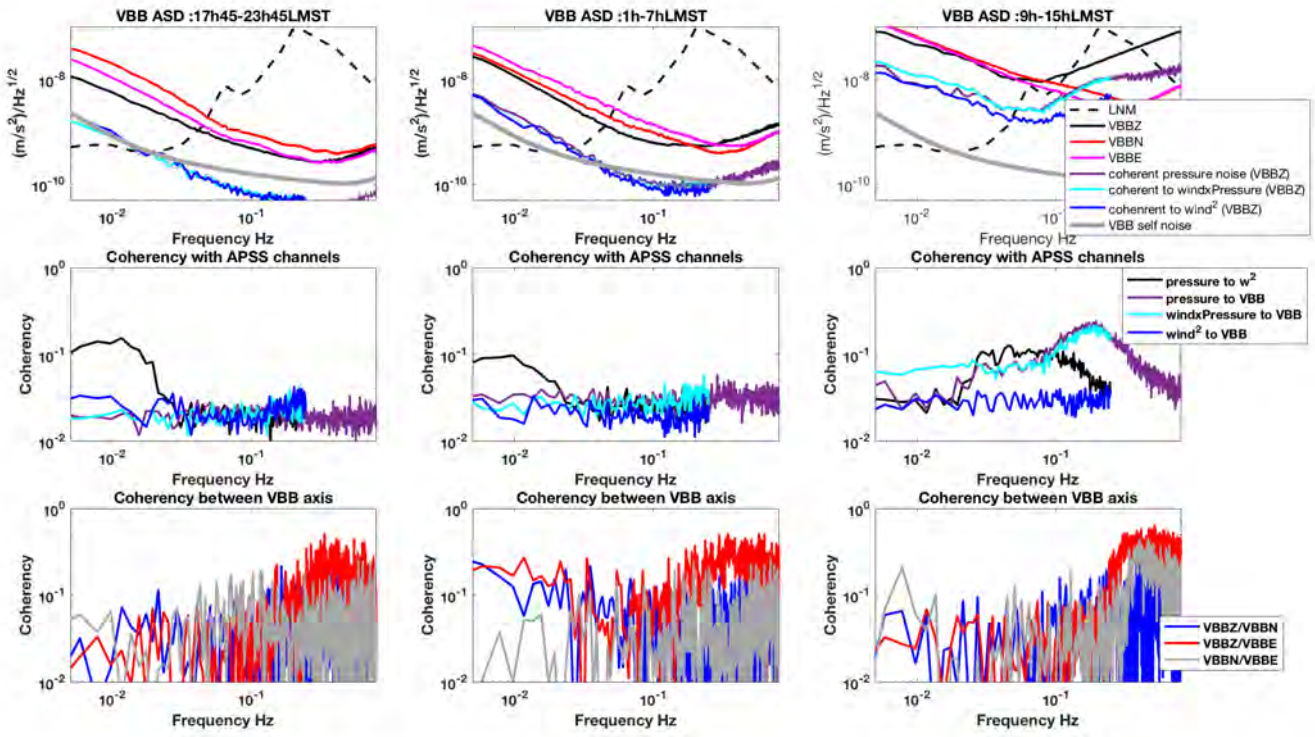

Figure S1-2: Mean noise and coherence to several atmospheric APSS data in three time periods: 17:45-23:45 which is the quietest period, 01:00-07:00, the second part of the night and 09:00-15:00 which is the most active part of the day. The noise evolution is clear. These three levels of noise appear also in the statistical distribution of the noise (see ***Figure 2*** of the main text). During the night, there is very low coherence with the atmosphere, with increased coherence, especially for pressure, during the day. The bottom figure shows the coherence between each VBB axis. While each pair exhibits a level of coherence, between the Z and E components it is notably high. All spectrum and coherencies are calculated for sols 183 to 209.

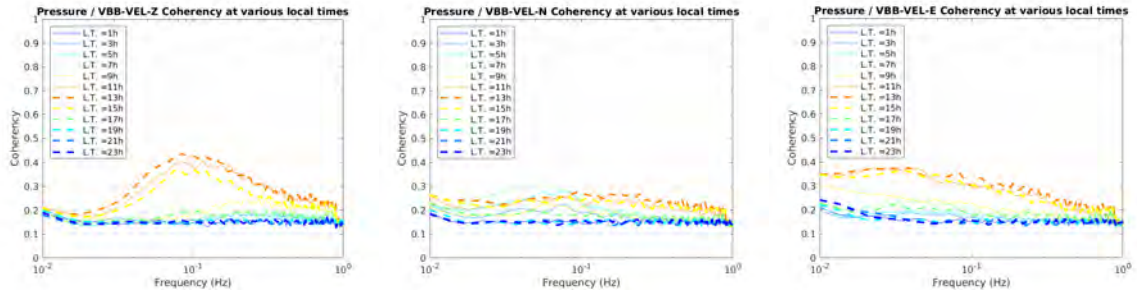

Figure S1-3: From left to right, the average coherence between Pressure and SEIS-VBB-VEL Vertical, North and East components, as a function of local time (colors). The 2 sps data from SEIS-VBB-VEL channels between sol 123 and sol 147 have been used for this analysis.

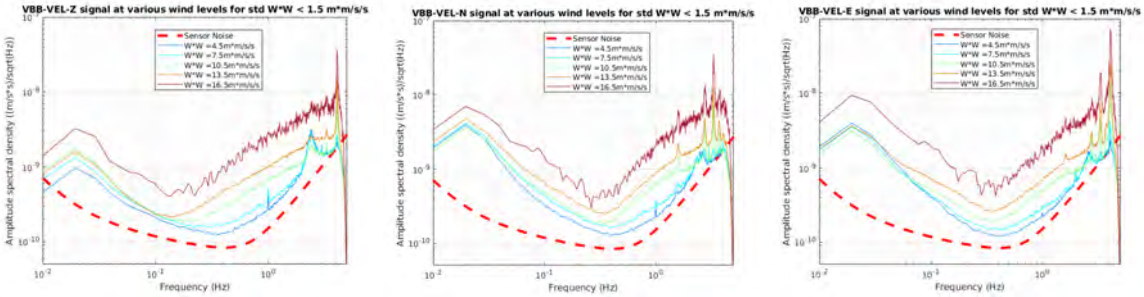

Figure S1-4: From left to right, acceleration spectra of Vertical, North and East channels of SEIS-VBB at various values of the square of wind velocity (color scale). Spectra are obtained by averaging spectra of 400s windows corresponding to mean squared wind values in bins of 3 $(m/s)^2$. The data used was from 6 sols from sol 168 to sol 174 at 10sps.

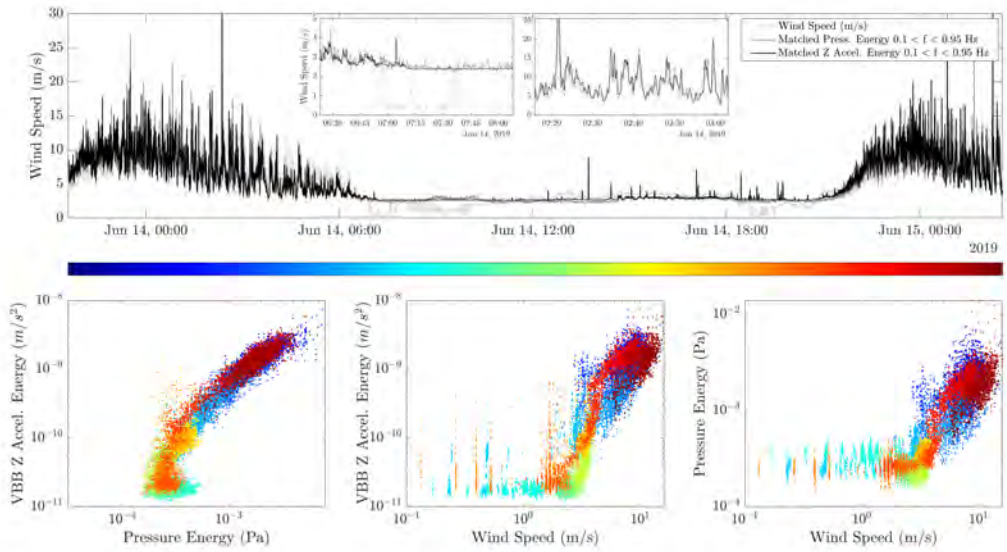

Figure S1-5: Top panel, the variation over sol 194-5 of the wind speed, pressure and seismic energies. The pressure and seismic signals correspond to root mean variance of the pressure and acceleration outputs, respectively, within a 0.1 to 0.95 Hz bandwidth. The insets show that at low wind speeds, TWINS time series are not reliable while for winds above 5 m/s there is a correlation between pressure and seismic energies and wind speed. The three lower panels show the covariation of the three measurements over the sol, color coded to the time in the sol.

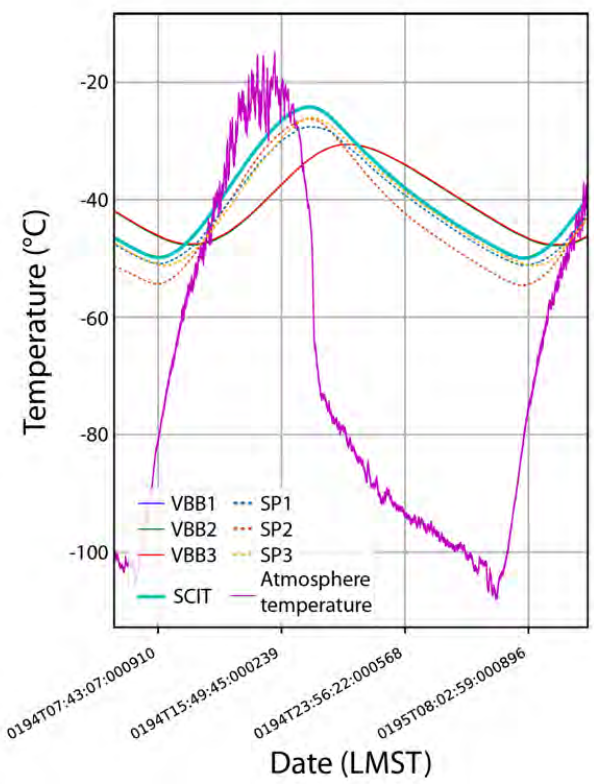

Figure S1-6: Temperature records of the VBBs sensor, the SPs dies, the scientific temperature (SCIT, located below the WBK on the LVL) and of the atmosphere. We observe the delay between atmosphere temperature and SCIT Temperature (due to the common shielding of the VBBs and SPs), the SPs (same as SCIT plus the SP housing) and the VBBs (same as SCIT plus the Evacuated Compartment (EC) shielding). All VBBs temperatures are superimposed to this scale, with daily variations between sensors not exceeding 0.05 K. Note also that all temperature fluctuations of the atmosphere are damped by the multi-layer thermal protections. The tether, located outside the WTS, is expected to have temperature variations slightly higher than the atmosphere.

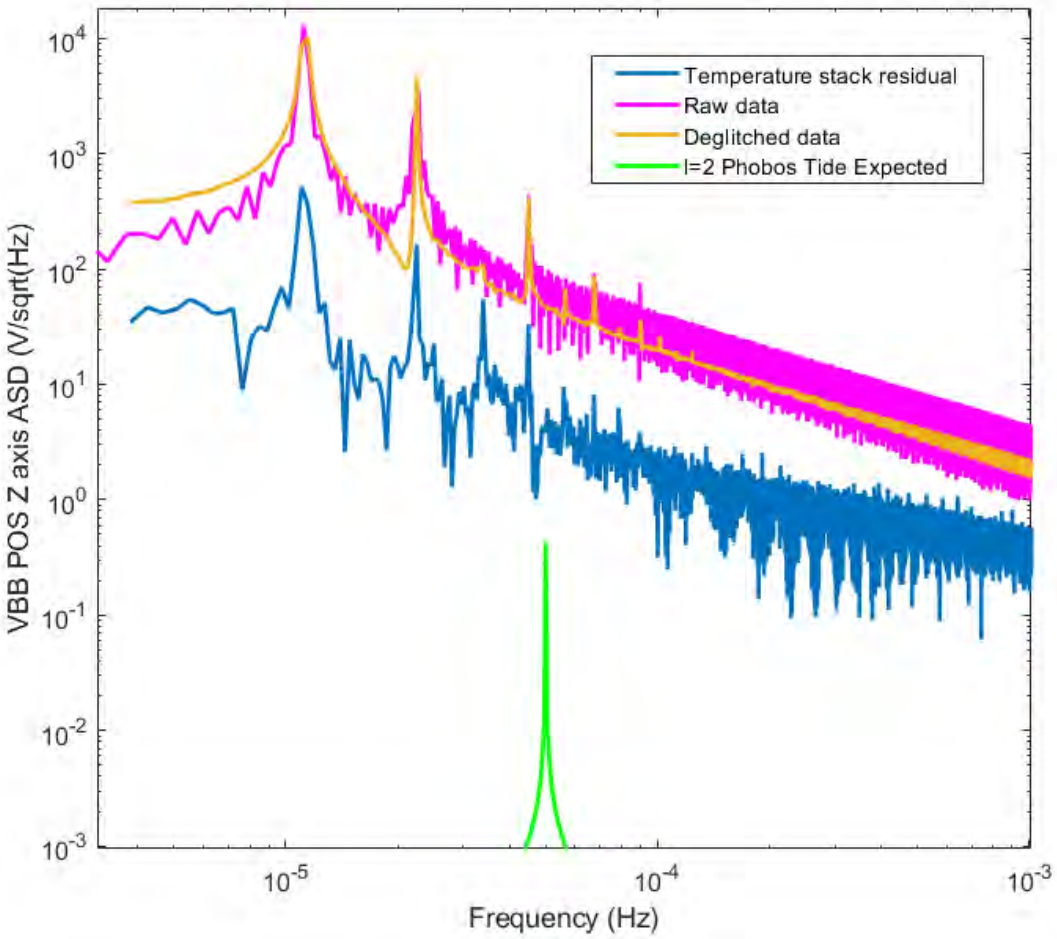

Figure S1-7: Amplitude spectral density of the VBB POS output on the Z axis over the month of June 2019. The noise in the raw data (magenta) is reduced firstly by applying a deglitching code (orange), and then a temperature decorrelation based on data stacking (blue). The expected amplitude of the main Phobos tide (degree l=2) is given as reference (green). The VBB position data for the month of June 2019 were processed in the following way: first, each VBB output was converted from digital units to Volts. Using the transfer functions of the VBB velocity outputs, glitches were modelled and identified in the VBB velocity data using cross correlation between the model and the data. The glitch time locations in the velocity outputs are then exploited to detect the glitches in the VBB position outputs. These glitches are removed by LMS fitting and cross correlation with a synthetic position glitch modelled from the transfer functions of the VBB position outputs, giving the deglitched data. Next, stacking is implemented with a 1 sol time window over the month of June on these deglitched VBB position data, with corrections to eliminate artificial features such as calibrations done by the team during this time range. The resulting stack of 1 sol duration is afterwards extended to the whole month of June and subtracted from the deglitched data, giving the temperature decorrelated data visible in the figure.

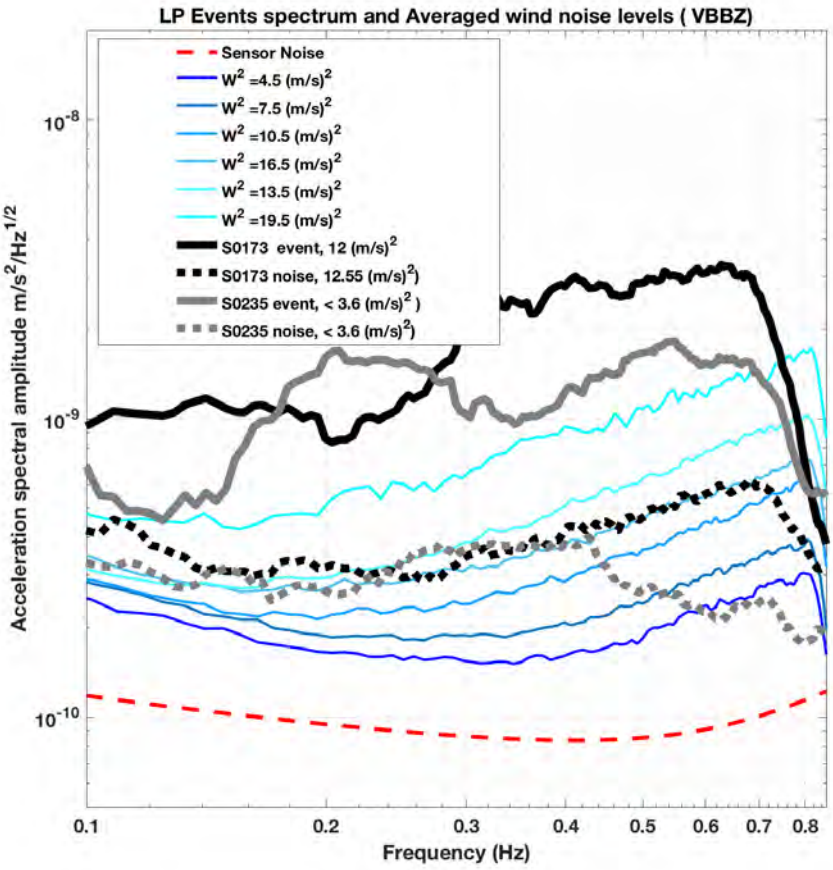

Figure S1-8: VBBZ signals recorded for the 2 long period events (S0173 and S0235) on the continuous 2 sps data between 0.1 and 0.85 Hz, as compared to the mean noise levels of the VBBZ as a function of wind. Wind levels are squared wind. All event and noise spectrum have been made on deglitched, Z data for 4 minutes time windows, either starting at the P arrival time for events or finishing at the P arrival time for noise. The amplitude SNR is about 7.5 at 0.4 Hz (2.5 sec) for S0173 and 2.5 for S0235 at the same frequency.

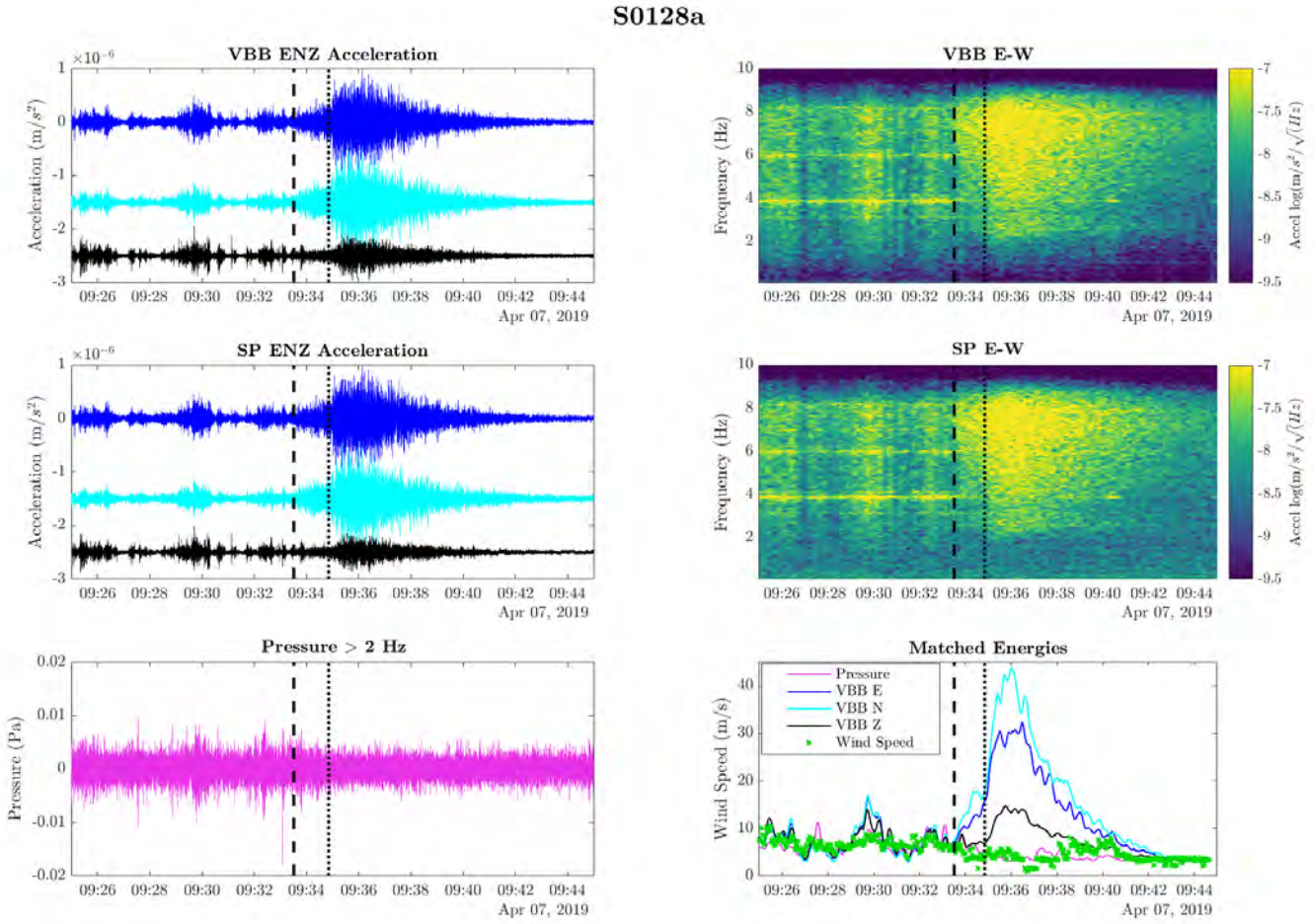

Figure S1-9: S0128 event with associated environmental conditions. Top panels: VBB seismograms for the 3 components (left) and spectrogram of the VBB E component (right)
Middle panels: similar plots for the SP sensor. Bottom left panel: Pressure as a function of time. Bottom right panel: the mean and variance matched time series for pressure, 3 component VBB and wind speed. Pressure and VBB components are converted in wind speed through the matching algorithm, which determine the scaling factor between wind energy and energy of channels possibly contaminated by that wind. The seismic event is identifiable above the environmental contributions between 09:34 and 09:44 LMST, with wind injection evident at 09:40 LMST. The records shown stop before the seismic signal due to the robot arm movement commanded just after this event at 09:48 LMST.

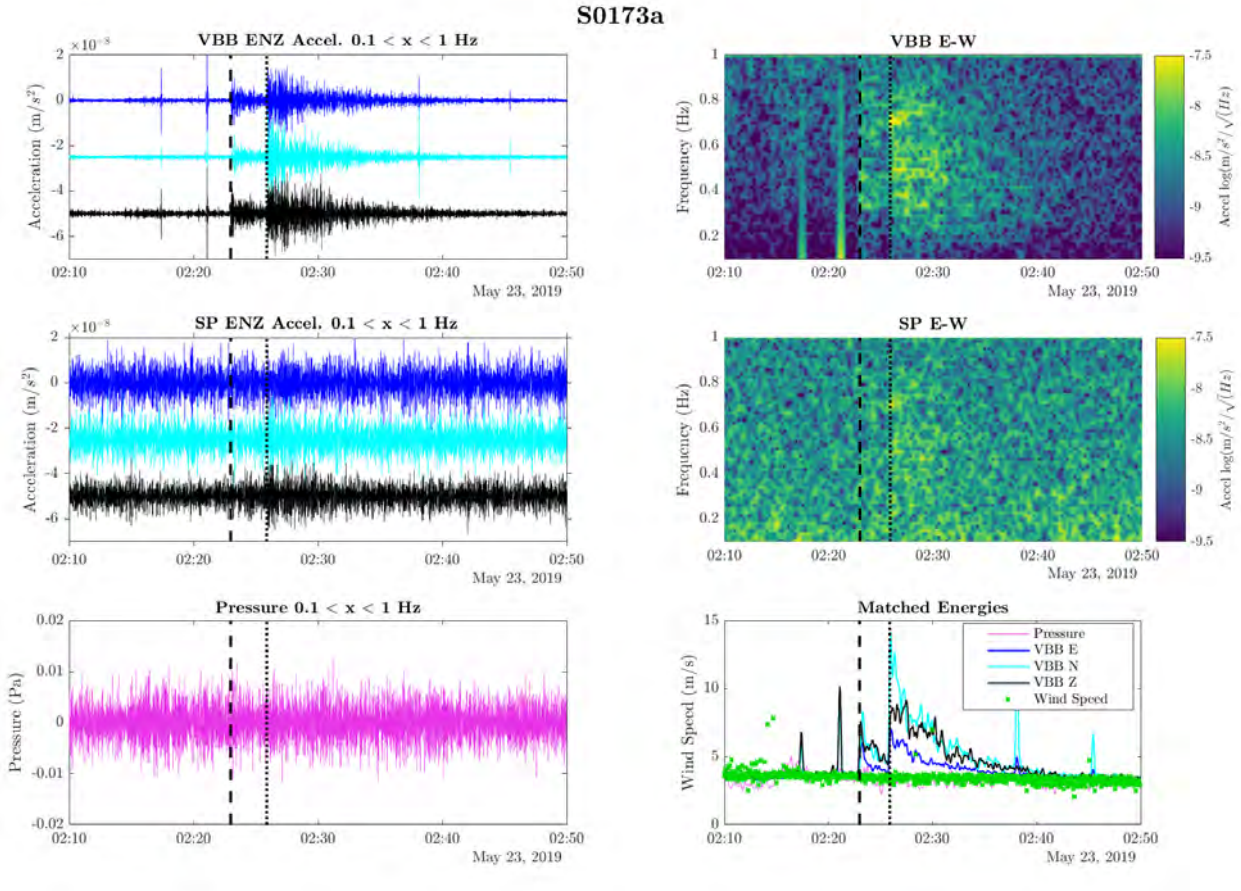

Figure S1-10: S0173 event with associated environmental conditions. Same as for ***Figure S1-9***. The seismic event is identifiable above the environmental contributions from 02:23 LMST.

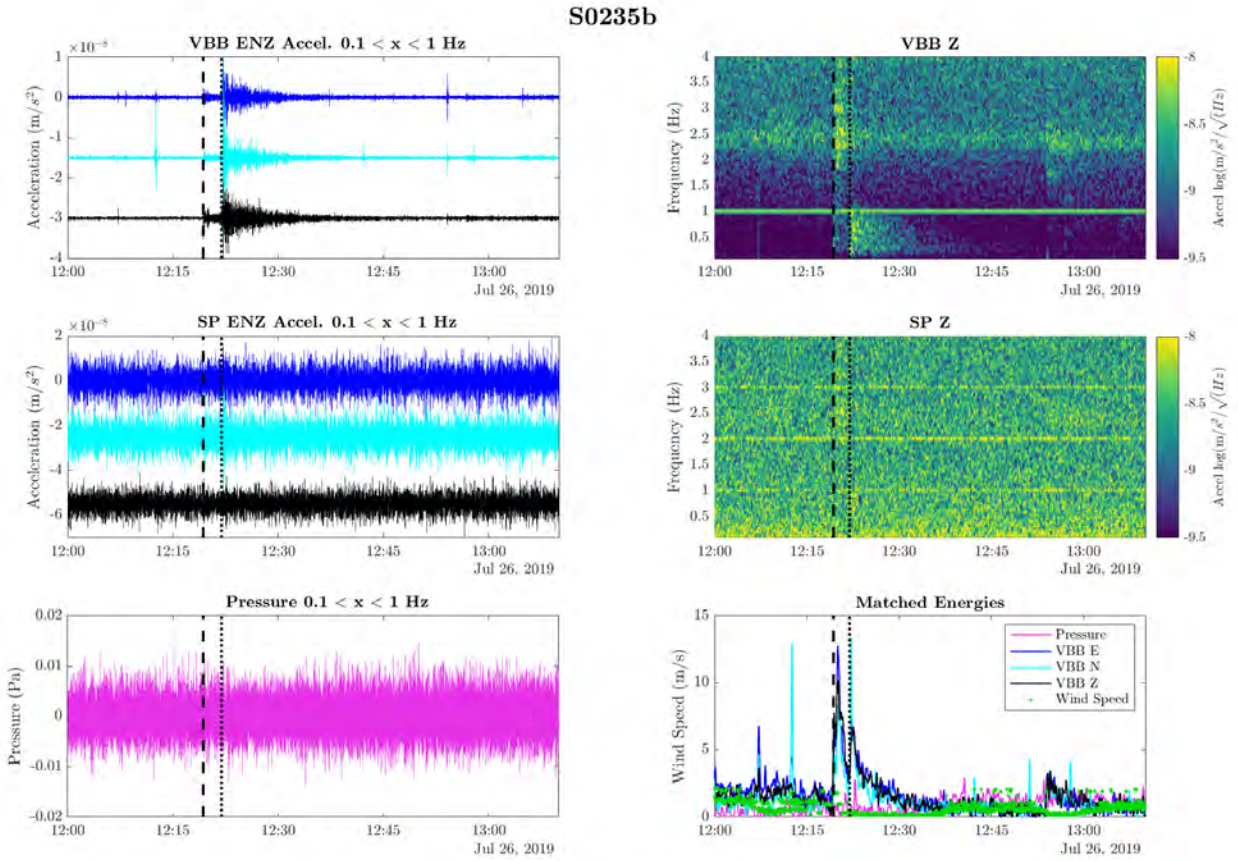

Figure S1-11: S0235 event with associated environmental conditions. Same as for ***Figure S1-9***. The seismic event is identifiable above the environmental contributions from 12:19 LMST.

Type	Amplitude threshold*	Number	Sol	Time(LMST)
Multi-component glitch	>= 1E-07 m/s	12	Sol194	00:38:50,03:08:44,03:16:27,03:52:17,04:22:37, 05:19:43, 05:50:55, 07:37:43,08:36:17,21:53:25, 22:40:12,23:53:19
Single-component glitch	>= 1E-07 m/s	2	Sol194	04:17:39, 04:43:27
Pressure drop	>=0.1Pa	36	Sol194	07:45:53, 08:43:32, 08:48:19, 09:01:32, 09:22:02, 09:29:11, 09:50:23, 10:03:22, 10:23:41, 10:27:16, 10:31:12, 10:37:39, 10:39:41, 10:47:59, 10:53:39, 11:14:24, 11:36:54, 11:53:31, 11:58:07, 12:49:02, 13:08:28, 13:15:22, 13:17:21, 13:24:25, 13:24:59, 13:57:07, 14:15:55, 14:17:26, 14:18:06, 14:27:45, 14:29:09, 14:54:02, 15:08:09, 15:20:31, 15:23:30, 16:19:23
Donk	>=1E-06 m/s	40	Sol194	17:04:19, 17:11:25, 17:17:04, 17:22:31, 17:28:05, 17:32:27, 17:36:23, 17:41:28, 17:42:53, 17:46:44, 17:50:24, 17:52:48, 17:55:13, 18:00:09, 18:00:16, 18:05:41, 18:11:29, 18:13:43, 18:18:19, 18:22:55, 18:25:15, 18:25:20, 18:38:24, 18:38:54, 18:44:36, 18:58:23, 19:13:15, 19:31:15, 19:32:19, 20:07:56, 20:28:02, 20:41:01, 21:20:00, 21:35:16, 21:50:23, 22:20:12, 22:22:06, 23:21:19, 23:42:05, 23:54:09
Multi-component glitch	>= 1E-07 m/s	10	Sol195	01:27:01, 03:08:48, 03:11:44, 04:29:34, 05:45:02, 17:22:08, 17:45:09, 21:33:31, 22:38:01, 23:40:11
Single-component glitch	>= 1E-07 m/s	3	Sol195	02:48:32, 04:39:02, 20:59:05
Pressure drop	>=0.1Pa	17	Sol195	09:18:29, 09:25:47, 09:26:54, 10:15:31, 10:33:06, 10:34:05, 10:35:22, 10:42:59, 10:53:15, 11:11:59, 11:31:44, 12:04:16, 12:37:15, 12:42:13, 14:01:00, 14:08:34, 14:45:02
Donk**	>=1E-06 m/s	20	Sol195	00:47:18, 00:52:55, 02:11:16, 02:54:07, 02:57:11, 03:38:09, 03:41:17, 03:51:53, 04:12:42, 04:27:04, 04:53:05, 04:58:16, 05:03:04, 05:10:59, 17:46:46, 17:48:27, 17:51:59, 17:58:29, 18:01:19, 18:02:40

Table S1-1: Glitch and other transient events detected on sol 195 and sol 196 by the MQS operators. Pressure drop are vortex or dust devils detected on the SEIS instrument. See Supplement 2 for more details. Donk are high frequency transient events of unknown origin. Single component glitch affects only one sensor while multi-component glitches affects at least two sensors and most of the time all sensors. ** Features with amplitudes below the threshold are not annotated. ** Donks are annotated on 100 Hz SP data, which is not complete for Sol195.*

Type	Amplitude threshold*	Number	Sol	Time(LMST)
Multi-component glitch	>= 1E-07 m/s	>60	Sol194	00:38:50, 03:08:44, 03:16:27, 03:52:17, 04:22:37, 05:19:43, 05:50:55, 07:37:43, 08:36:17, 21:53:25, 22:40:12, 23:53:19,11:42:53, 11:54:34,12:18:53, 11:08:49, 13:42:35, 14:26:23,21:49:13,21:49:13,23:52:49,23:41:08 …
Single-component glitch	>= 1E-07 m/s	>12	Sol194	02:48:32, 04:39:02, 20:59:05, 10:47:59, 10:53:39, 11:53:31, 11:58:07, 12:48:02, 13:08:28, 13:15:22, 13:17:21, 13:25:28, 13:24:50, 13:57:10, 11:14:30…
Pressure drop	>=0.1Pa	>12	Sol194	11:53:31, 11:58:07, 12:49:02, 13:08:28, 13:15:22, 17:58:40, 18:01:23, 18:04:51, 18:11:35, 18:11:43, 07:45:53, 08:43:32, 08:48:19, 09:01:30, 09:21:58, 09:29:15, 09:50:15, 10:03:18, 14:15:55, 14:17:26, 14:17:06, 14:27:58, 14:29:10, 14:53:56, 15:07:59, 15:20:26, 15:23:30, 16:19:23…
Multi-component glitch	>= 1E-07 m/s	>55	Sol195	01:27:03, , 07:32:43, 17:22:28, 10:35:10, 21:42:21, 05:43:02,22:41:12, 03:09:46, 03:11:44, 04:29:29, 17:45:09, 21:32:31, 22:38:03, 23:40:12..
Single-component glitch	>= 1E-07 m/s	>14	Sol195	02:48:32, 04:39:02, 21:33:31, 22:39:01, 23:41:10, 20:59:03, 01:42:11, 03:10:49, 07:12:10, 04:29:34, 05:45:02, 11:36:50, 02:48:32, 03:40:10, 20:50:05….
Pressure drop	>=0.1Pa	17	Sol195	09:19:29 10:33:10, 10:34 :03, 10:32:22, 10:42:59, 10:53:15, 11:11:59, 11:31:44, 12:04:16, 12:37:15, 12:42:13, 13:59:58, 14:09:34, 14:43 :10, 09:25:57, 09:27:00 , 10:17:31

Table S1-2: Table S1-2: Glitch and Pressure drop events detected on sol 195 and sol 196 by a learning machine algorithm.

Supplement S2: Subsurface

P.Lognonné, S.Kedar, N.Brinkman, L.Fayon, M.van Driel, M.Drilleau, B.Kenda, N.Murdoch, C.Perrin, C.Schmelzbach, D. Sollberger, F. Andersson, P.Delage, A. Horleston, J. Knollenberg, S.Krasner, C.Krause, J. ten Pierick, J. Robertsson, S.Rodriguez, L. Rochas, T.Spohn, N.Teanby, J.Vallade, N.Verdier, C.Vrettos

S2-1: Duricrust Elastic Properties

The mechanical leveling system (LVL) is the tripod structure on which the SPs and the VBBs are mounted. It ensures correct level placement on the Martian ground under unknown local conditions, and governs the mechanical coupling between SEIS and the ground. We developed an analytical model of the LVL's mechanical behavior and, in particular, of its resonances[1]. As the LVL is much more rigid than the ground, the resonances are mostly dependent on the horizontal stiffness coefficient k^H_g and tilt stiffness torque coefficient C_g that characterizes the mechanical interaction between the ground and the LVL feet. The mostly horizontal resonance frequency was detected after SEIS deployment at 39.35 +/- 1 Hz, and after a first leveling at 39.1 +/- 1 Hz (***Figure S2-1a***), in general agreement with laboratory measurements. It shifted, as predicted, when the legs of the LVL retracted in the LVL low position, to about 52 Hz (***Figure S2-1b***).

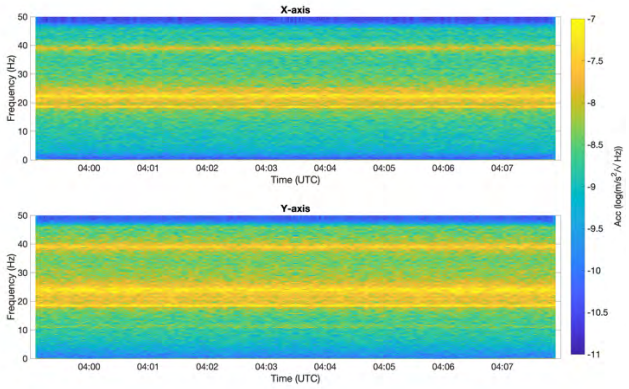

Figure S2-1a: Spectrogram of Martian SEIS data from January, 4 on X and Y axes, by using the 3 SPs and 3 VBBs signals. The 39 +/- 1 Hz resonance is due to the LVL structure.

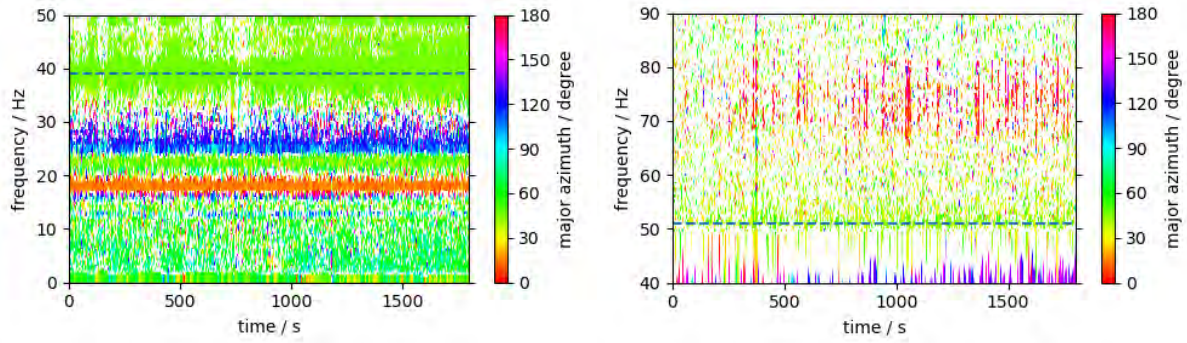

Figure S2-1b: Azimuth of the major axis of the polarization ellipse for wind induced noise pre (left) and post (right) leveling low. While the LVL resonance was not clearly visible in amplitude spectra in the 50-100Hz range, the consistent polarization of noise with the same azimuth suggests the mode has moved to 51 +/- 1 Hz.

The frequency value of the horizontal resonance provides constraints on the ground elastic properties. This is made by a MCM exploration of the Young modulus matching the resonance frequency, for a priori Poisson coefficients ranging from ν= 0.2 to ν=0.3. We used analytical expressions of the elastic solutions[2] for k^H_g and C_g and a function of E and ν, and added an additional source of error related to the small spike on the SEIS feet. We get E=46.8 +/- 10 MPa (20 % of uncertainty) which corresponds to k^H_g =2.7 +/- 0.54 10^6 N/m (***Figure S2-1c***) and C_g =1800 +/- 360 N.m/rad. The ratio between these two model parameters can be expressed as follows:

=

with S = πa^2, the area of the foot disk (of radius a) and the ratio only depends on the Poisson coefficient ν. Laboratory tests carried on Martian sand analogs with the SEIS Martian feet loading provided a smaller C_g mean value of ~1660 N.m/rad. But due to experimental constraints, the measurements were made on only one foot, not like in the tripod configuration and with larger strain than that mobilized during the LVL resonance. This could explain the smaller value obtained[3].

By considering a regolith density ρ=1400 kg/m^3 and a Poisson coefficient of 0.22 at the Martian surface, we find V_p about 137 +/- 15 m/s at 1 kPa which corresponds to about 5 cm depth and possibly of the top of the regolith just below its crust. This nevertheless confirms slightly faster surface velocities than those estimated on HP^3 travel, when extrapolated at the same pressure (118 m/s, see case 2 of the preliminary inversion below). This agrees with stiffer elastic parameters of the crust as compared to the topmost regolith.

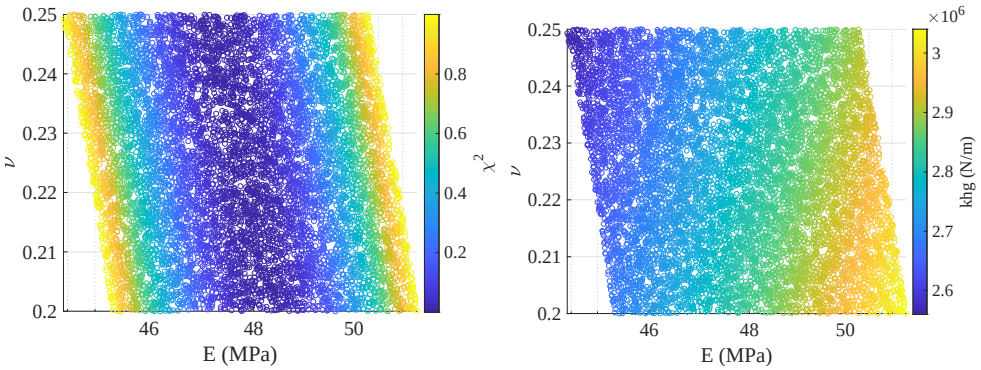

Figure S2-1c: On the left, χ^2 (squared difference between modeled and measured resonances) and on the right, $k_H{}^g$, as a function of the ground Young modulus E and Poisson coefficient ν at 1σ for two different dates: December, 22, 2018 before any leveling and January, 4, 2019 after the first LVL leveling on Mars.

S2-2: Velocity in the Regolith layer

In order to extract near-surface velocities from the HP^3-SEIS seismic recordings by travel time analysis, the location of the mole tip (assumed to act as seismic source) and the location of SEIS (seismic receiver) as well as the trigger time of each hammer stroke need to be accurately known. The spatial locations of SEIS and HP^3 in a local site frame are known with an accuracy of about 1 mm from high-resolution images obtained from the two cameras on the lander. SEIS and HP^3 are horizontally separated by a distance of *x* = 1.18 m (***Figure S2-2***). Because the HP^3 mole did not significantly advance any further

after the first five minutes of hammering session 1 (sol 92), the depth of the mole tip is assumed to remain constant for the remaining time of session 1 and the following sessions 2 (sol 94), 3 (sol 118) and 4 (sol 158). After four hammering sessions carried out up to the time of writing, the HP^3 support structure was lifted on sols 203 to 209 and images of the exposed mole were taken. Based on these images, the mole tip could be located at 32.9 cm depth below the surface. Additionally, the mole is inclined by 20° from the vertical with the mole tip pointing towards SEIS resulting in the configuration shown in ***Figure S2-2***. The distance *s* between the mole tip and SEIS can be calculated using the trigonometric relation $s =$, where *x* is the horizontal distance between SEIS and HP^3, *d* is the depth of the mole and θ is the tilt of the mole with respect to the vertical. Thus, *s* is estimated to be 1.11 m.

The trigger time of the mole hammer strokes can be retrieved with a resolution of 600 Hz from the measurements of the two accelerometers mounted inside the mole[4]. The trigger times were used to align the seismic data and to arrange them into a so-called common-receiver gather with time zero corresponding to the trigger time of each trace (See ***Figure S2-3a*** and ***c***). In total, four datasets are available from the HP^3-SEIS experiment for both the VBB and SP sensor at the time of writing. Here, we only discuss the last two hammer sessions and the SP sensor recordings for the seismic velocity analysis due to issues with the HP^3 trigger calibration in sessions 1 and 2. Furthermore, the SP data acquisition settings for hammering sessions 3 and 4 were specifically adapted to record data with a higher than nominal temporal resolution. During sessions 3 and 4, we recorded temporally aliased SP data by omitting antialiasing filters in the data acquisition chain. Data with a high temporal resolution were then recovered with a sparseness-promoting reconstruction algorithm[5] that exploits the regular structure of the common receiver gather (see high degree of similarity between individual hammer stroke recordings in e.g. ***Figure S2-3a***). In addition, particular care was taken to achieve a high-precision lander-SEIS-HP^3 clock relative knowledge.

For hammer session 3 and 4, we manually picked the first arriving phase (onset) for each hammer stroke, which is assumed to be a near-field motion arriving at the P-wave travel time. The time difference between the picked onset time and the origin time of the signal (i.e. the trigger time) corresponds to the travel time of the seismic phase from the source to the receiver. The apparent seismic P-wave velocity V_P^{app} is found from the relation: $= s/$, where t_P is the P-wave travel time. ***Figure S2-3b*** and d show the picked travel time distribution. The average travel time for sessions 3 and 4 is t_P = 9.40 $\pm$ 2.68 ms. Accordingly, V_P^{app} is determined to be 118 $\pm$ 34 m/s. This estimate represents an average over a certain volume between the mole tip and SEIS.

Overall, the obtained low V_P^{app} is consistent with unconsolidated cohesionless sand[6] with seismic velocities lower than those of several Mars analogues[7]. To date, no reflections from the lower regolith boundary could be identified to constrain the total regolith thickness. Potentially, resonances observed in the seismic data may allow to further constrain the regolith thickness and seismic velocity structure.

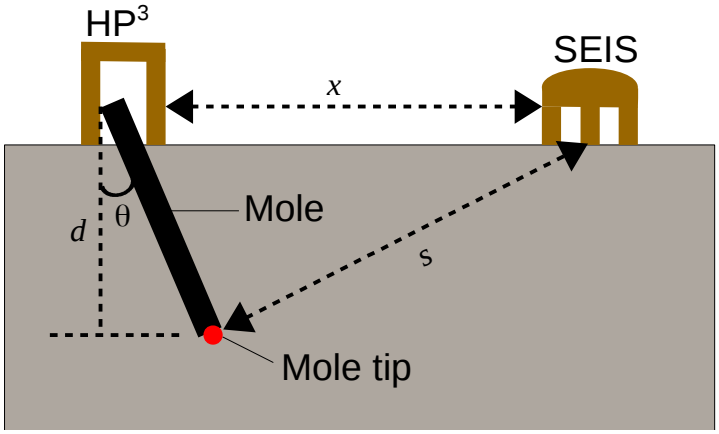

Figure S2-2: Schematic cross-section of the locations of HP^3, the mole with the mole tip in red and SEIS with respect to each other. s is the travel path, *x* is the horizontal distance between SEIS and HP^3, *d* is the depth of the mole and θ is the tilt of the mole with respect to the vertical.

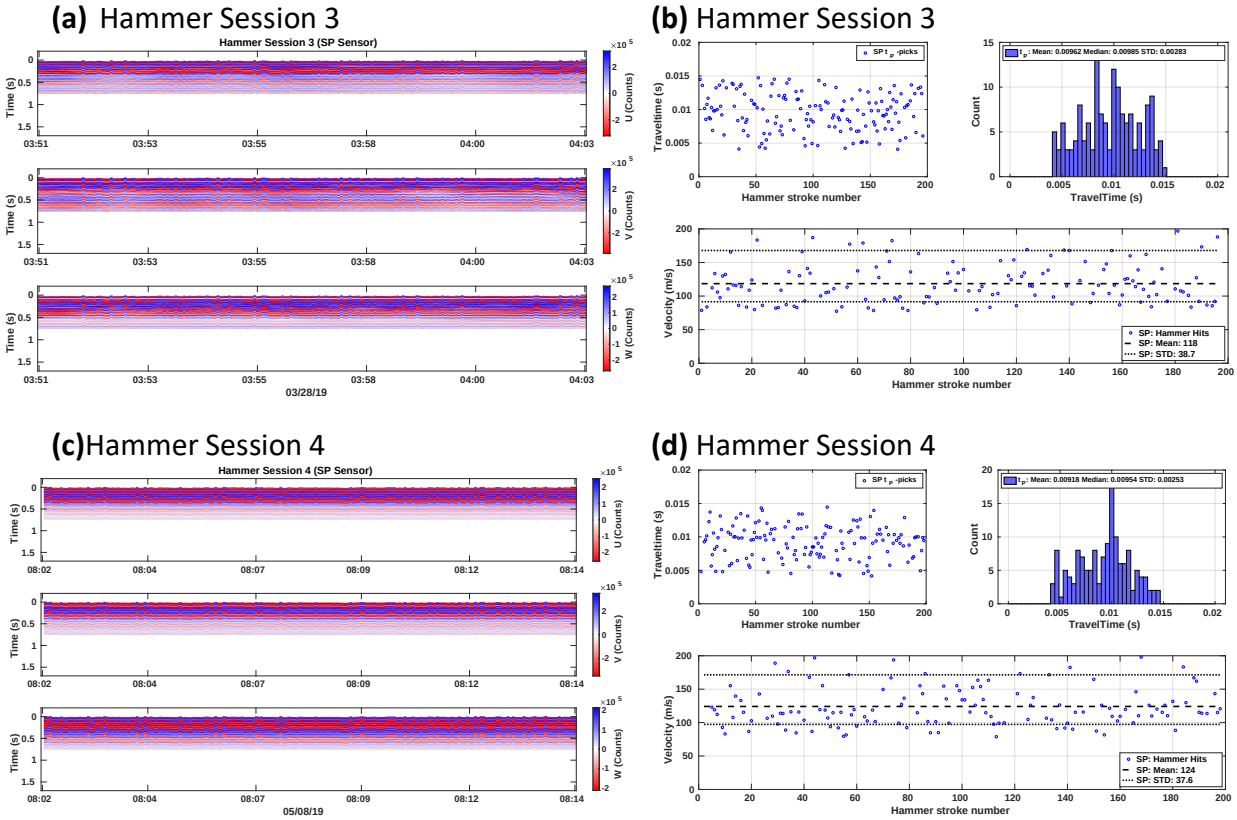

Figure S2-3: **(a)** and **(c)**: Seismic data recorded by the short period sensor (SP) of SEIS arranged as a common-receiver gather with time zero corresponding to the trigger time of each hammer hit. **(b)** and **(d)**: Travel time and P-velocity analysis recorded by the SP.

S2-3: Convective vortex modelling

Convective vortices are characterized by a pressure drop, typically of a few tenths to a few Pa, that induces small deformations of the ground that can be felt by the sensitive VBB seismometer. On the vertical component, the quasi-static ground motion can be modeled based on the pressure and wind time series and the frequency-dependent ground compliance (the ratio between vertical velocity and pressure forcing). The frequency dependency is related to the sensitivity depth to elastic properties, which scales

with frequency. This simple theory[8,9] has been applied to InSight seismic and meteorological data (**Figure 3** in main text) for about 360 vortices between Sol 72 and Sol 168 in different wind and environmental conditions. For each event, a dominant frequency band is determined and the apparent compliance in this band is calculated. The results (Figure S2-4, left panel) show a clear increase of the compliance with frequency that is compatible with an increasing Young's modulus with increasing scale. Examples of broadband vortices also exhibit the same trend of ground compliance with frequency (Figure S2-4, right panel).

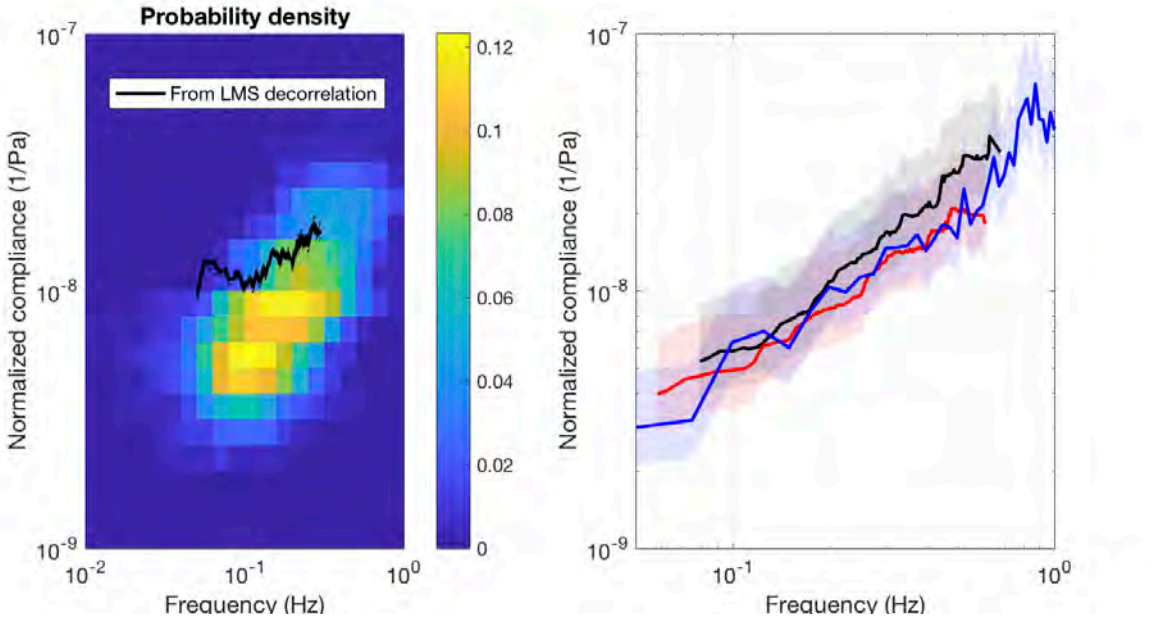

Figure S2-4: Frequency-dependent compliance. Left panel: probability distribution determined from the analysis of about 360 vortices. The black line shows the results from an independent pressure-decorrelation method based on an adaptive least-mean square algorithm. Right panel: apparent compliance for three broadband vortex encounters (black, red and blue curves). The relevant frequency range is defined as the band with coherence between seismic and pressure time series larger than 0.8. The shaded areas represent uncertainties, mainly due to the determination of the advecting wind speed (+/- 3 m/s with respect to the mean values measured by TWINS).

A second method – the vortex model - for modelling the convective vortex makes use of a Green's function approach, which calculates the ground deformation due to the vortex load[10]. Here it is assumed that the total negative load of a convective vortex of diameter D and core pressure ΔP_o can be estimated[11] by $L = (\pi/2)\Delta P_o D^2$. This vortex model, applied to terrestrial dust devil data[11], assumes that the force applied is purely vertical and that the ground is a homogenous half-space defined by a Young's modulus and Poisson's ratio. For simplicity it is assumed that the ground deformation under SEIS is purely vertical. This vertical ground displacement leads to a vertical acceleration (the double time derivative of the ground displacement), and a tilt signature on the horizontal components of SEIS (the local spatial derivative of the vertical ground deformation). Assuming that the vortex follows a simple straight-line trajectory (an approximation observed for high wind and from HiRise observations), the ground deformation, and thus

the seismic signal of the vortex, are calculated at each instant of the trajectory. Fig. 3 (main text) shows example fits to the seismic and pressure data of two events using this vortex model. The solutions are non-unique but only a limited range of ground parameters (specifically, the Young's modulus) can provide a simultaneous simulation to both the seismic and pressure data. As is shown in Fig. 3 of the main text, the transverse horizontal model fits the seismic data better than the parallel horizontal model. There are two reasons for this: First, as the ground tilts away from the vortex, the tilt signature is largest in the direction perpendicular to the vortex closest approach (the transverse direction). Secondly, the longitudinal component is more likely to be influenced by drag forces induced by the vortex winds that are not modelled here: for a typical encounter (i.e., the vortex doesn't pass directly over InSight), at closest approach, the tangential wind velocity is perpendicular to the direction of the horizontal tilt. Any drag force due to the wind[12], therefore, acts in a direction perpendicular to the tilt signal at the closest approach influencing the parallel seismic signal, but not the transverse seismic signal.

(2) Up to 49 new dust devil tracks (DDTs) have been detected in an area of ~12 km^2 around the InSight lander based on the analysis of ratios between three high-resolution satellite images from HiRISE[13] acquired on Dec 6th, 11th, 2018 and Feb 4th, 2019. Semi-automatic track detections, using the radon transform technique, have been performed, where tracks are considered as linear features (with the possibility of slight curvature). Only few tracks possibly passed in the close vicinity of the lander and the seismometer SEIS (three tracks < 50m), while most of the tracks are observed at greater distance (Fig. S2-5).

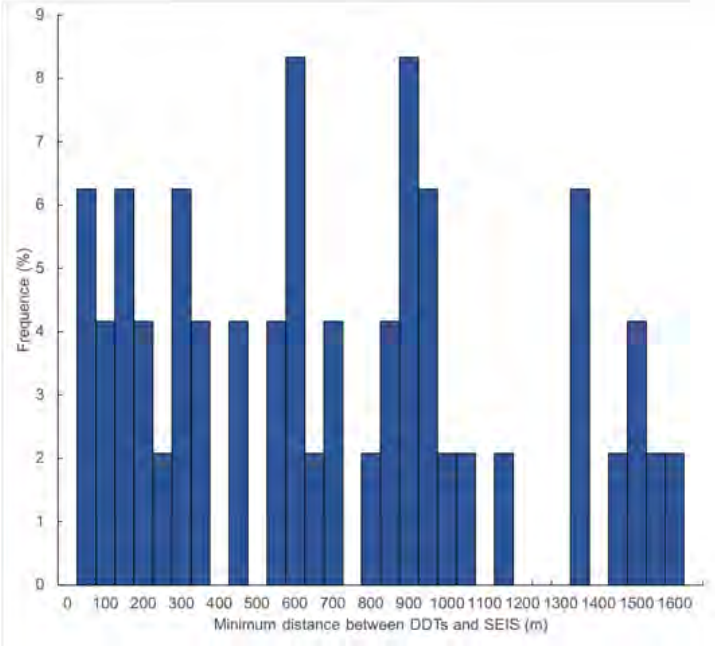

Figure S2-5: Minimum distance between dust devil tracks (DDTs) and SEIS (m) estimated from semi-automatic track detections on HiRISE images.

S2-4: First Inversion

The combination of the compliance measurements from dust devils and the averaged velocity in the regolith estimated from HP^3 hammering allow us to propose first constraints on the subsurface models based on SEIS data records. The inverse problem consists of retrieving both the Young modulus and Poisson's ratio in the first 20 m below the surface from compliance data set and the apparent seismic V_p velocity (see sections **S2-2 and S2-3**). Since the problem is undetermined, in order to study the model uncertainty and non-uniqueness, a Bayesian approach[14] is considered. A Markov chain Monte Carlo algorithm is used[15-17], which yields probability density functions (pdfs) of the elastic parameters as a function of depth. The forward problem is based on Sorrells' theory[8], which links the elastic properties to the compliance as a function of frequency.

Two cases are considered. First, an inversion based only on compliance data (**Figure S2-6, a1-d1**), which is sensitive to spatially integrated properties, and an inversion based on both compliance data and V_p apparent velocity (**Figure S2-6, a2-d2**), the latter being sensitive to very local properties. In both cases, the depth of the regolith/bedrock interface is scanned, as well as Young's modulus and Poisson's ratio in the bedrock. Regolith compaction is assumed using an empirical power law (equations 1 and 20 from [17]), and assuming that the medium is densely compacted. In the first case, a 10 cm regolith crust is fixed with the following properties: V_p = 130 m/s, V_s = 75 m/s, and ρ= 1400 kg/m^3. The effect of the crust on the large scale inversion is expectedly marginal. In the second case the duricrust is removed, and the apparent V_p from HP^3 is taken (V_p = 120 m/s ± 40 m/s). We assume this as averaged seismic velocity in the top 0.8 m, about one wavelength of the 150 Hz central signal of HP^3 (see **section S2-2**). We set the density of the bedrock to 2600 kg/m^3, which is about 15% less than typical basalts[18] for the density in the bedrock. Density is not constrained and is used only for representing the result of the inversions of Young modulus and Poisson ratio in terms of seismic velocity.

The results (**Figure S2-6, a1-c1, a2-c2**) show all possible solutions and illustrate the trade-off between the seismic velocities in the regolith, the bedrock and the depth the regolith/bedrock interface. It nevertheless bounds the range of acceptable models. At 11 cm depth, V_p in the regolith varies between 174 ± 32 m/s and 118 ± 11 m/s in case 1 and 2, respectively. V_p values in the bedrock are spread, but a lower bound of 450 m/s could be estimated and values are in the range of terrestrial volcanic subsurface velocities[19]. Tests done with the density found in Gale crater for the bedrock (1680 kg/m^3)[20], tend to exclude such low density as it will result in high velocities. The data fit (**Figure S2-6, d1, d2**) show that all the models accepted by the algorithm fit the compliance data within their uncertainty bounds. However, the data fit slightly better in the case where the constraint from HP^3 is not taken into account. This is likely for one part because the models have a larger degree of freedom within the parameter space. This also explains why the range of the regolith to bedrock transition is more peaked in case 2 (< 2 m) than in case 1. In case 2, we observe an overall offset of the compliance toward lower values and therefore softer material. One explanation might be related to the fact that HP^3 samples the ground just beneath SEIS, in a crater where low velocity materials tend to accumulate, while the dust devils mostly sample outside this ~20m diameter crater.

The **Figure S2-7a-b** provides an example of nine a priori models, each being obtained from the conditional probability that regolith to bedrock discontinuity occurs at a

depth closest from one of the models depth. All are subsets of the distribution of models shown on **Figure S2-6**. **Figure S2-7a** is for models A from the HP3 and compliance measurement, while ***Figure S2-7b*** is for the models B from only compliance data. These models are provided as ***Supplement Table 1*** for models A and ***Supplement Table 2*** for models B.

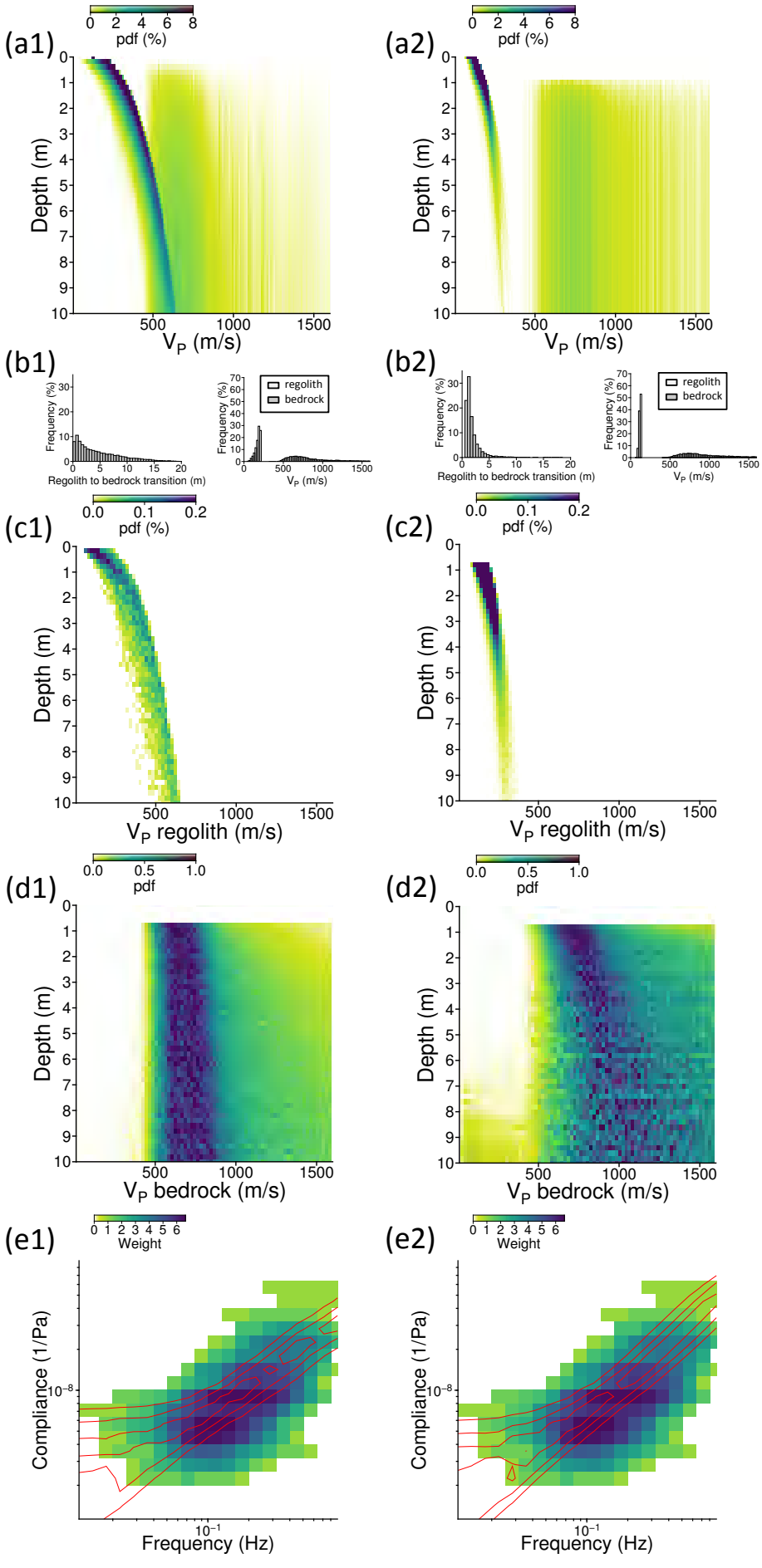
(a1)
(a2)
pdf (%)
Depth (m)
V_P (m/s)
(b1)
(b2)
Frequency (%)
Regolith to bedrock transition (m)
regolith
bedrock
V_P (m/s)
(c1)
(c2)
V_P regolith (m/s)
(d1)
(d2)
pdf
V_P bedrock (m/s)
(e1)
(e2)
Weight
Compliance (1/Pa)
Frequency (Hz)

Figure S2-6: Comparison of the Bayesian inversions results of compliance only (left), and both compliance and V_p apparent velocity (right). (a1-2) shows the probability density function (pdf) of V_p as a function of depth. Yellow and dark purple colors are low and high probability, respectively. The pdfs are computed using 12'000 models. The pdf values are computed by counting the number of models in each 10 m/s V_p interval, every 0.1m depth. For a given depth, the sum of the pdf over all the V_p intervals is equal to 100 per cent. (b1-2, left) show the marginal probabilities of the regolith to bedrock transition. Intervals are 0.5m wide. (b1-2, right) represent the marginal probabilities of V_p in the regolith at 0.11 m depth (light gray) and in the bedrock (dark gray). Intervals are 20 m/s wide. (c1-2) Normalized PDF showing for each depth of the regolith to bedrock transition the V_p distribution at the regolith's basement. The pdf values are computed by counting the number of models in each 20 m/s V_p interval. (d1-2) Normalized PDF showing for each depth of the regolith to bedrock transition the V_p distribution in the bedrock. The normalized pdf values are computed by counting the number of models in each 20 m/s V_p interval every 0.1m depth. For a given depth, the pdf is then divided be the maximum pdf value over all the V_p intervals. (e1-2) are the input probability distribution of the compliance as a function of frequency determined from the analysis of about 360 vortices. The pdf values correspond to **Figure S2-4** divided by the total number of events. In order to obtain a reliable number of models accepted in the inversion algorithm, the pdf is then smoothed by taking its square root and multiplying by 4. The red lines show the output of the probability density function, for which the sum over all the compliance values for a given frequency is equal to one. The contours are plotted every 0.3.

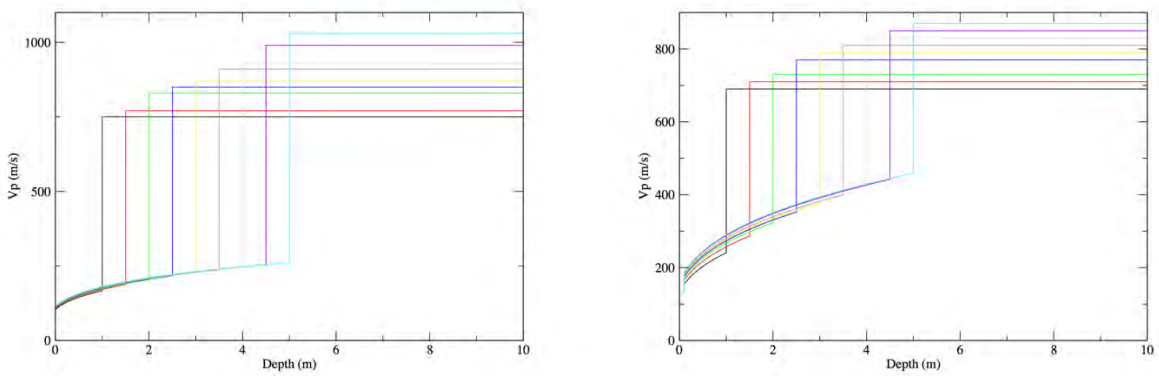

Figure S2-7. (Left). $V_p(z)$, where V_p is the P velocity as function of depth z, for nine models with increasing depth for the regolith to bedrock discontinuity from inversion results jointly made with HP3 and compliance data (models A). (Right). Same for nine models from inversion results made with the compliance only (models B). For both models A and B, depths are 1m, 1.5m, 2m, 2.5m, 3m, 3.5m, 4m, 4.5m, 5m. $V_p(z)$, $V_s(z)$ and $\rho(z)$ are available in **Supplement Table 1** and **Supplement Table 2** for A and B respectively.

References:

[1] Fayon, L., Knapmeyer-Endrun, B., Lognonné, P. et al., A Numerical Model of the SEIS Leveling System Transfer Matrix and Resonances: Application to SEIS Rotational Seismology and Dynamic Ground Interaction, *Space Sci Rev*, **214**, 119, http://doi.org/10.1007/s11214-018-0555-9, (2018).

[2] Poulos, H.G. and Davis, E.H., Elastic solutions for soil and rock mechanics, Wiley, 411 pages, ISBN: 978-0471695653, (1974).

[3] Atkinson, J. H. (2000). Non-linear soil stiffness in routine design. *Géotechnique*, **50**, 487-508

[4] Spohn, T. et al. The heat flow and physical properties package (HP^3) for the InSight mission, *Space Science Reviews*, **214**, 96, http://doi.org/10.1007/s11214-018-0531-4, (2018).

[5] Brinkman, N., C. Schmelzbach, D. Sollberger, M. van Driel, J. ten Pierick, J. O. A. Robertsson, F. Andersson, S. Stähler, D. Giardini, S. Kedar, T. Hudson, K. Hurst, A. KiVely, W. B. Banerdt, M. Grott, T. Spohn, C. Krause, L. Fayon, P. Lognonné, B. Knapmeyer-Endrun, P. Delage, W. T. Pike, A. Horleston, N. Teanby, and C. Vretto, The first active seismic experiment on Mars to characterize the shallow subsurface structure at the InSight landing site, *SEG Technical Program Expanded Abstracts*, 4756-4760, doi: 10.1190/segam2019-3215661.1, (2019).

[6] Golombek, M., N. H. Warner, J. Grant, E. Hauber, V. Ansan, C. Weitz, N. Williams, C. Charalambous, S. Wilson, A. DeMott, M. Kopp, H. Lethcoe-Wilson, L. Berger, R. Hausmann, E. Marteau, A. Trussell, W. Folkner, S. Le Maistre, N. Müller, M. Grott, T. Spohn, S. Piqueux, E. Millour, F. Forget, I. Daubar, N. Murdoch, P. Lognonné, C. Perrin, S. Rodriguez, W. T. Pike, T. Parker, J. Maki, H. Gengl, R. Deen, F. Calef, M. Baker, M. Banks, A. Spiga, D. Banfield, J. Garvin, C. Newman, C. Vrettos, Geology of the InSight landing Site, Mars, *Nature Geosciences*, submitted (2019).

[7] Delage, P., F. Karakostas et al. An investigation of the mechanical properties of some Martian regolith simulants with respect to the surface properties at the InSight mission landing site, *Space Sci. Rev.*, **211**, 191–213, http://doi.org/10.1007/s11214-017-0339-7 , (2017).

[8] Sorrells, G.G., A Preliminary Investigation into the Relationship between Long-Period Seismic Noise and Local Fluctuations in the Atmospheric Pressure Field, *Geophys. J. Int.*, **26**, 71-82, https://doi.org/10.1111/j.1365-246X.1971.tb03383.x , (1971).

[9] Kenda, B., P.Lognonné, A.Spiga, T.Kawamura, S.Kedar, W. Bruce Banerdt, R.Lorenz, Modeling of ground deformation and shallow surface waves generated by Martian dust, devils and perspectives for near-surface structure inversion, *Space Science review*, **211**, 501-524, http://doi.org/10.1007/s11214-017-0378-0 , (2017).

[10] Murdoch, N., B.Kenda, T.Kawamura, A.Spiga, P.Lognonné, D.Mimoun, W.B. Banerdt, Estimations of the seismic pressure noise on Mars determined from Large Eddy Simulations and demonstration of pressure decorrelation techniques for the InSight mission, *Space Science review*, **211**,457-483, http://doi.org/10.1007/s11214-017-0343-y , (2017).

[11] Lorenz, R. D., Kedar, S. Murdoch, N.,Lognonné, P., Kawamura, T.; Mimoun, D., Banerdt, W.B., Seismometer Detection of Dust Devil Vortices by Ground Tilt, *Bull. Seismological Society of America*, **105**, 3015-3023, https://doi.org/10.1785/0120150133 , (2015).

[12] Murdoch, N., D.Mimoun, R. F. Garcia, W.Rapin, T.Kawamura, P.Lognonné, D.Banfield, W.B. Banerdt, Evaluating the Wind-Induced Mechanical Noise on the InSight Seismometers, *Space Science Review*, **211**, 429-455, http://doi.org/10.1007/s11214-016-0311-y, (2017).

[13] McEwen, A. S., Eliason, E. M., Bergstrom, J. W., Bridges, N. T., Hansen, C. J., Delamere, W. A., et al. (2007). Mars reconnaissance orbiter's high resolution imaging science experiment (HiRISE). *Journal of Geophysical Research E: Planets*, *112*(5), 1–40. https://doi.org/10.1029/2005JE002605

[14] Mosegaard, K., A. Tarantola, Monte Carlo sampling of solutions to inverse problems. Journal of Geophysical Research. 1001. 12431-12448., http://doi.org/10.1029/94JB03097 , 1995.

[15] M Drilleau, E Beucler, A Mocquet, O Verhoeven, G Moebs, G Burgos, J-P Montagner, P Vacher, A Bayesian approach to infer radial models of temperature and anisotropy in the transition zone from surface wave dispersion curves, Geophy. J. Int., 195, 1165-1183, 2013.

[16] Panning, M.P, E. Beucler, Drilleau,, Mocquet,, Lognonné, P, Banerdt, W.B. , Verifying single-station seismic approaches using Earth-based data: Preparation for data return from the InSight mission to Mars, *Icarus*, 230-242, **248**, https://doi.org/10.1016/j.icarus.2014.10.035 , (2015).

[17] Panning, M.P., P.Lognonné, W. B. Banerdt, R. Garcia, M. Golombek, S. Kedar, B. Knapmeyer-Endrun, A.Mocquet, N.A. Teanby, J.Tromp, R. Weber, E. Beucler, J.F.Blanchette-Guertin, E.Bozdag, M. Drilleau, T.Gudkova, S. Hempel, A.Khan, V. Leki, N.Murdoch, A.C. Plesa, A.Rivoldini, N.Schmerr, Y.Ruan, O.Verhoeven, C.Gao, U.Christensen, J.Clinton, V.Dehant, D.Giardini, D.Mimoun, W. T Pike, S. Smrekar, M. Wieczorek, M.Knapmeyer, J.Wookey, Planned products of the Mars Structure Service for the InSight mission, Mars, *Space Science review*, **211**, 611–650, https://doi.org/10.1007/s11214-016-0317-5 , (2017).

[18] Morgan, P., Grott, M., Knapmeyer-Endrun, B., Matt Golombek, P. Delage, P.Lognonné, S. Piqueux, I. Daubar, N. Murdoch, C. Charalambous, W. T. Pike, N. Müller, A. Hagermann, M. Siegler, R. Lichtenheldt, N. Teanby, S. Kedar, A Pre-Landing Assessment of Regolith Properties at the InSight Landing Site, *Space Sci Rev*, **214**, 104. http://doi.org/10.1007/s11214-018-0537-y , (2018).

[19] P. Lesage, M.J. Heap, A.Kushnir, A generic model for the shallow velocity structure of volcanoes, Journal of Volcanology and Geothermal Research, 356, 114-126, https://doi.org/10.1016/j.jvolgeores.2018.03.003, (2018).

[20] K.W. Lewis, S. Peters, K. Gonter, S. Morrison, N. Schmerr, A. R. Vasavada, T. Gabriel, A surface gravity traverse on Mars indicates low bedrock density at Gale crater, *Science*, **363**, 535-53, http://doi.org/10.1126/science.aat0738 , (2019).

Supplement S3 : Scattering and Attenuation

L. Margerin, T. Kawamura, E. Beucler, M. Calvet, R. Garcia, P. Lognonné, S. Menina,
M. Panning, T. Pike, N. Schmerr, E. Stutzmann,
C. Beghein, T. Nissen-Meyer, A.-C. Plesa, M. Schimmel, R. Weber

1 Introduction

In this supplement we present the scattering and attenuation results for three seismic events observed by SEIS, S0128a, S0173a and S0235b. Waves from these events traversed the martian crust and mantle (see Figure S3-1) and provide a record of the structure found between the source and SEIS station. From the signal characteristics and modeling of these two example events, we determined the preliminary nature of attenuation and scattering in Mars, both properties that affect the amplitudes of seismic energy as it travels in the interior. As Mars lies between the Earth and Moon in size and mass, possesses a thin atmosphere, and has experienced similar evolutionary processes, we expect the attenuation and scattering of Mars to fall someplace in between the Earth and Moon.

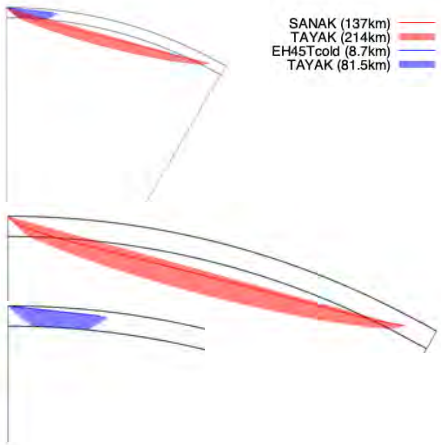

Figure S3-1: Probable ray paths for the S0128a event (in blue) and the S0173a event (in red). The top plot shows the ray trajectories at the same scale for both events. The bottom plots present zoom on the ray paths of each event for convenient visualization. The *a priori* velocity models used to calculate the raypaths and the corresponding turning depth of the ray are indicated in inset. The Moho is delineated by a solid black arc. The Moho depth varies between 32 km and 90 km among the models. See Smrekar et al. (2018) for further details on the *a priori* seismic models.

2 Regional Event (S0128a)

2.1 Signal Characteristics

2.1.1 Signal to Noise ratio

The S0128a event is a more than 5-minute long signal that rises above the noise level for frequencies larger than 2Hz. Figure S3-2 shows the Signal-to-Noise ratio (S/N) of the event in the 0.1Hz-7Hz frequency band. S/N is defined here as the ratio between the total energy contained in a 500s time window starting at the arrival time of the maximum and a 500s time window of noise preceding the signal onset. The S/N ratio rises above the commonly accepted threshold of 4 (Aki & Chouet, 1975) for the horizontal components at frequencies typically higher than 5Hz. The S0128a waveforms did not require any correction for glitches.

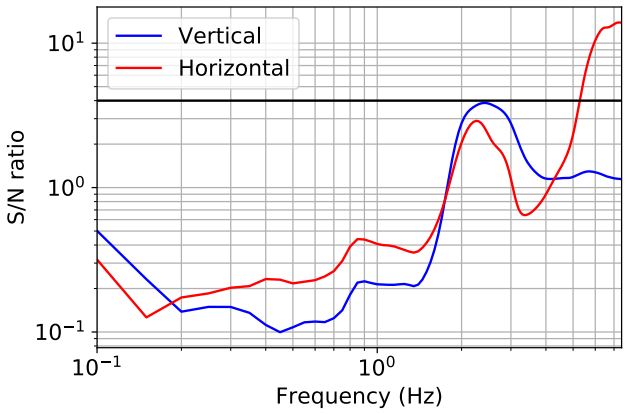

Figure S3-2: Signal-to-Noise (S/N) ratio of the S0128a event on the vertical and horizontal components of SEIS VBB. The thick horizontal black line corresponds to $S/N = 4$.

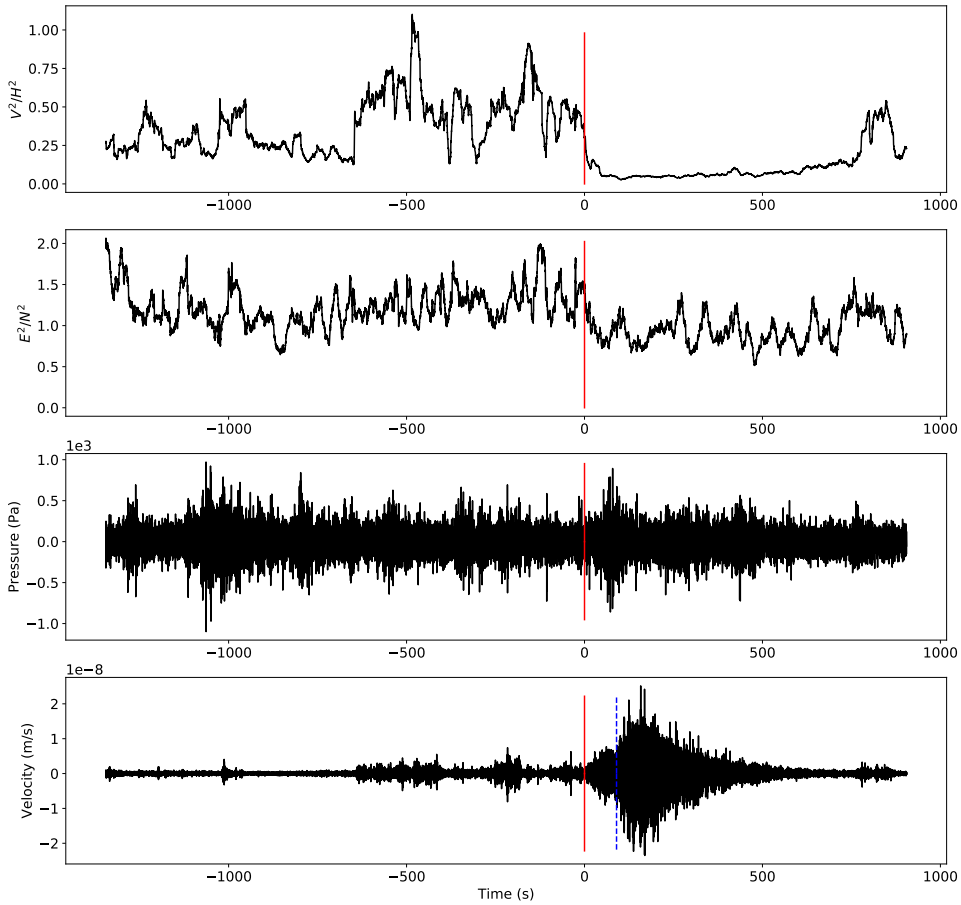

Figure S3-3: Energy partitioning of the S0128a event around 7.5Hz. From top to bottom: Ratio between the kinetic energy on the vertical and horizontal components, ratio between the kinetic energy on the East-West and North-South components, pressure time series, North-South component of the velocity. The red line shows the inferred time of signal onset (at $t = 0$s). The dashed blue line is a tentative onset time for the second energy 'packet'.

2.1.2 Energy Partitioning

There is a distinct manifestation of the transition from noise to signal that is indicated in Figure S3-3 where we show the partitioning of the kinetic energy among the different data components around 7.5Hz. The kinetic energy of a given component is obtained through the following operations: a band-pass filtering of the time-series, squaring and smoothing. In the example shown in Figure S3-3 the smoothing window is typically 15s long. The S0128a event manifests itself as a clear reduction of the variance of the vertical-to-horizontal (V^2/H^2)

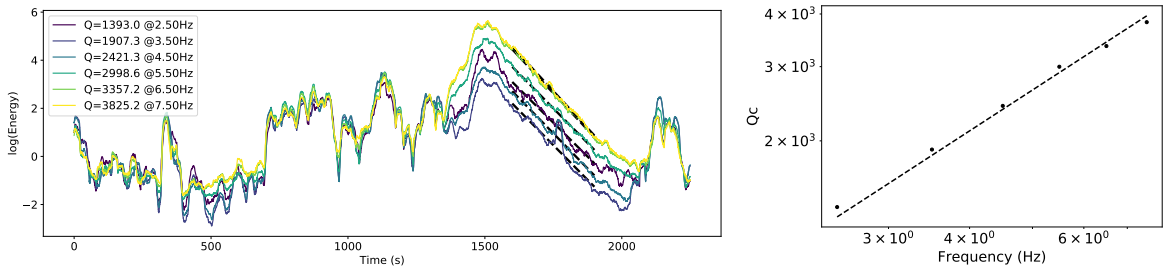

Figure S3-4: Analysis of the frequency dependent coda quality factor Q_c of the S0128a event. Left: Logarithm of energy envelopes as a function of time and fit of the coda decay (black dashed lines). The different colors correspond to different frequency bands. The event is visible around $t = 1500$s. Right: frequency dependence of Q_c in the 2.5Hz-7.5Hz frequency band. The dashed line shows the linear regression $Q_c = 528f$ (f is the frequency).

kinetic energy ratios. We observe that in the noise time window, the V^2/H^2 ratio shows large deviations around a mean value of about 0.44 ± 0.19. Some of these fluctuations are caused by large pressure variations which couple with the seismometer as can be inferred from a comparison of the pressure with the V^2/H^2 energy partitioning ratio. These fluctuations are also jointly visible on the velocity seismograms and the E^2/N^2 ratio. By contrast, in the signal time window, the V^2/H^2 ratio stabilizes around a value close to 0.05 ± 0.01. Such a stabilization is characteristic of a multiply-scattered short-period wavefield as has been previously reported in the literature (e.g. Hennino et al., 2001). The value of the V^2/H^2 partitioning ratio is in the same range as the one observed by Margerin et al. (2009) on weathered granites at Pinyon Flats Observatory. Although the reduction of variance is less obvious on the E^2/N^2 partitioning ratio, the average value shifts from 1.34 ± 0.24 in the noise to 0.93 ± 0.15 during the event, in reasonable agreement with the theoretical value 1 for a diffuse wavefield.

The morphology of the seismogram shown in Figure S3-3 resembles that of a shallow moonquake (Dainty et al., 1974). It appears to be composed of two energy 'packets' or 'bursts' -visible at high-frequency on the horizontal components- although it is impossible to discern ballistic P and S waves by polarization analysis. Furthermore, the signal shows a prolonged coda, characteristic of a scattering medium. This suggests that S0128a has probably propagated in a heterogeneous crust. Possible ray paths are indicated in Figure S3-1. There are at least two possible interpretations for the two energy packets: (1) a double event ('foreshock' followed by a 'mainshock') in a diffusing medium which has totally erased the initial polarization of the source. The foreshock would correspond to a smaller magnitude source which would explain why its energy emerges from the noise at higher frequencies than the mainshock. In this hypothesis, it is impossible to locate the event and only a trade-off relation between diffusivity, absorption and hypocentral distance can be derived. (2) A second possibility is that of a single event in which the initial source information has only been partially erased so that the onset of the first and second energy packets corresponds approximately to the arrival of P and S waves -marked respectively by red and blue lines in Figure S3-3-, respectively. In this hypothesis, the event can be approximately located and the trade-off between attenuation properties and location partially lifted. Besides shallow Moonquakes, as mentioned above, similar diffuse P and S energy packets have been observed in Japan for subduction zone earthquake generated waves propagating through the volcanic front of the Kanto-Tokai area (Obara & Sato, 1995). These two hypotheses are examined in more details below.

2.1.3 Coda quality factor

An empirical characterization of the decay rate of seismogram envelopes is offered by the estimation of the coda quality factor Q_c (Aki & Chouet, 1975). It can be measured by performing a linear regression of the logarithm of the energy of the signal after filtering in a narrow frequency band. Here, we employ four poles Butterworth filters in successive frequency bands $[3f/4, 5f/4]$ centered around frequency $f \in \{2., 3.5, 4.5, 5.5, 6.5, 7.5\}$. Figure S3-4 summarizes our analyses of Q_c in the 2.5Hz-7.5Hz frequency band. The envelopes have been corrected for the noise level and clearly show the emergence of two energy packets as frequency increases. The applied correction simply consists in normalizing the energy of the signal by the average energy of the noise. The decay of the Log Energy in the coda is almost perfectly linear so that the uncertainties on individual Q_c measurements are typically less than 1%. Another striking feature is the fact that in the frequency band of interest the Log Energy curves are all parallel to one another. This implies that the typical coda duration is frequency independent. We find that our Q_c measurements can be conveniently summarized by the simple law $Q_c = 528f$ (see Figure S3-4 right). We obtain a slightly better match to the data by fitting a more general power law $Q = Q_0 f^n$ to the data with $Q_0 = 600 \pm 26$ and $n = 0.93 \pm 0.03$. The almost linear frequency dependence of Q_c is consistent with the observation of an almost frequency-independent absorption time, as discussed below.

2.2 Envelope modeling

2.2.1 Diffusion model

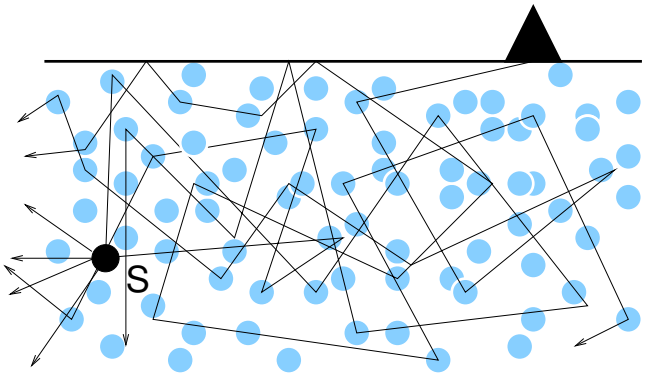

Figure S3-5: Schematic view of the propagation model for the S0128a event. S denotes the source location. Scatterers are represented by the blue circles, with possible raypaths of scattered waves indicated by the lines.

Consider the first scenario where only the most energetic 'packet' is considered as significant and this energy packet propagates in the diffusive regime. Although the earthquake cannot be located, we can establish a trade-off relation between the diffusivity D, the absorption time t_i and the hypocentral distance R. We recall that the point source solution to the following diffusion equation (Akkermans & Montambaux, 2007):

$$\left(\partial_t + t_i^{-1}\right) e(t,\mathbf{r}) - D\nabla^2 e(t,\mathbf{r}) = \delta(\mathbf{r})\delta(t) \tag{1}$$

is given by:

$$e(t,\mathbf{r}) = \frac{e^{-r^2/4Dt - t/t_i}}{(4\pi Dt)^{d/2}}, \tag{2}$$

where d is the space dimension and $e(t,\mathbf{r})$ is the energy density of the signal at time t and position $\mathbf{r}$. In the analysis that follows, we assume that $d = 3$, which corresponds to the transport of energy by body waves in unbounded space. In seismological applications, the absorption time t_i is often expressed in terms of an absorption quality factor $Q_i = 2\pi f t_i$, where f is the central frequency of the signal. For an in-depth discussion of the diffusion approach to energy transport in heterogeneous media, we refer the reader to Akkermans & Montambaux (2007) as a general reference and Sato et al. (2012) for theory and applications to seismology.

The multiple-scattering process for a point-source radiating in a heterogeneous medium is schematically represented in Figure S3-5. In the long lapse-time limit $t \to \infty$, we have $\partial_t \log e(t) \propto -1/t_i$ and we can use the approximation $Q_i \approx Q_c$, with Q_i the absorption quality factor (Shapiro et al., 2000). Although we cannot formally prove that the $t \to \infty$ limit applies, it appears as a very reasonable first guess, attested by the almost perfectly linear decay of the coda in log-linear scale (see Figure S3-4). In other words we assume that Q_c provides a direct constraint on Q_i (hence on t_i), independent of the source location. To constrain the diffusivity, we exploit the arrival time of the maximum of the energy t_{max} characterized by $\partial_t e|_{t=t_{max}} = 0$.

$$\begin{aligned} t_{max}^{-1} =& \frac{3D}{R^2}\left(1 + \sqrt{1 + \frac{4R^2}{9Dt_i}}\right) \quad \text{or:} \\ \frac{R^2}{D} =& 4t_{max}\left(\frac{t_{max}}{t_i} + \frac{3}{2}\right) \end{aligned} \tag{3}$$

Examination of the waveform in Figure S3-3 suggests that the arrival time of the maximum occurs approximately between 75s and 150s after the onset of the signal. From the linear dependence of Q_c we deduce an absorption time $t_i \approx 85$s. For a source located respectively at 1km, 10km and 100km from the station, this gives the corresponding range of diffusivities: 5.1—14×10^{-4}km^2/s, 5.1—14×10^{-2}km^2/s and 5.1—14km^2/s, so that the diffusivity can actually range over several orders of magnitude.

2.2.2 Radiative transfer model

The second scenario we examine is the full envelope modeling of the S0128a event, including the two energy 'packets', as the consequence of a single impulsive source. Explaining double diffuse arrivals can only be

performed in the framework of elastic radiative transfer theory. Here we employ a simplified formulation (Margerin, 2017) where the S waves are considered to be depolarized:

$$
\begin{aligned}
\left(\partial_t + c^p \mathbf{n}\cdot\nabla\right)\rho^p(\mathbf{r},\mathbf{n},t) = &-\left(\frac{1}{\tau^p}+\frac{1}{t_i^p}\right)\rho^p(\mathbf{r},\mathbf{n},t) + \frac{1}{\tau^{pp}}\int_{4\pi} p^{pp}(\mathbf{n},\mathbf{n}')\rho^p(\mathbf{r},\mathbf{n}',t)d^2\mathbf{n}' \\
&+ \frac{1}{\tau^{ps}}\int_{4\pi} p^{ps}(\mathbf{n},\mathbf{n}')\rho^s(\mathbf{r},\mathbf{n}',t)d^2\mathbf{n}' + S^p(\mathbf{r},\mathbf{n},t) \\
\left(\partial_t + c^s \mathbf{n}\cdot\nabla\right)\rho^s(\mathbf{r},\mathbf{n},t) = &-\left(\frac{1}{\tau^s}+\frac{1}{t_i^s}\right)\rho^s(\mathbf{r},\mathbf{n},t) + \frac{1}{\tau^{sp}}\int_{4\pi} p^{sp}(\mathbf{n},\mathbf{n}')\rho^p(\mathbf{r},\mathbf{n}',t)d^2\mathbf{n}' \\
&+ \frac{1}{\tau^{ss}}\int_{4\pi} p^{ss}(\mathbf{n},\mathbf{n}')\rho^s(\mathbf{r},\mathbf{n}',t)d^2\mathbf{n}' + S^s(\mathbf{r},\mathbf{n},t)
\end{aligned}
\tag{4}
$$

In Eq. (4), we have introduced the following notations: $\tau^{\alpha\beta}$ is the mean free time for scattering conversion from mode α to mode β ($\alpha,\beta \in \{P,S\}$), t_i^α, the absorption time of mode α, c^α the velocity of mode α and $\rho^\alpha(\mathbf{r},\mathbf{n},t)$ the energy density of mode α propagating in direction $\mathbf{n}$ at time t and position $\mathbf{r}$, $S^\alpha(\mathbf{r},\mathbf{n},t)$ the source term for mode α. The partitioning of the energy at the source into P and S waves is assumed to be that of a double couple source, which depends solely on the ratio of velocities (c^p/c^s) to the fifth power (Sato et al., 2012). The functions $p^{\alpha\beta}(\mathbf{n},\mathbf{n}')$ represent the (probabilistic) scattering patterns for conversion from mode α to mode β. The total scattering mean free time of a mode α is given by $1/\tau^\alpha = \sum_\beta 1/\tau^{\alpha\beta}$. At a given frequency f, the mean free times and absorption times can be converted to respectively scattering and absorption quality factors by the relations : $Q_{sc}^\alpha = 2\pi f \tau^\alpha$, $Q_i^\alpha = 2\pi f t_i^\alpha$.

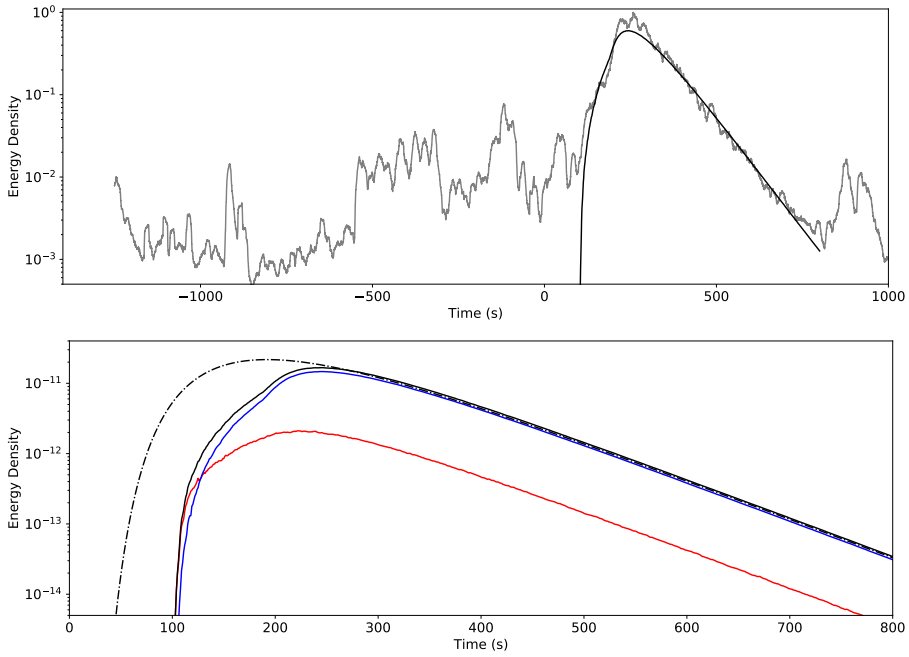

Figure S3-6: Envelope modeling of the S0128a event. Top panel: radiative transfer model (black line) compared to the total energy envelope of the horizontal components. Lower panel: theoretical partitioning of P and S energy for the radiative transfer model shown in the top panel. Blue: S energy. Red: P energy. Solid black line: total energy. Dashed line: diffusion approximation.

In this work, we make the usual assumption that the fluctuations of the elastic parameters are well described by a Von-Karman power spectrum. This assumption has been well verified on Earth based on the analysis of well-log, seismic and laboratory data (Sato, 2019). The key parameters of this model are the correlation length of the fluctuations l_c, as well as the exponent κ controlling the decay of the power spectrum at large wavenumbers. Furthermore, we employ Birch Law to reduce the number of independent parameters. More precisely, we assume perfectly correlated velocity and density fluctuations with $\delta\rho/\rho = \nu\delta c^\alpha/c^\alpha$. We also assume the following ad-hoc relation between the absorption times: $t_i^p = 9t_i^s/4$. This last relation can be justified by assuming that all the dissipation is governed by the rigidity (in a Poisson solid). With these assumptions, scattering theory allows one to calculate all the parameters that enter into Eq. (4), which can subsequently be solved numerically using the Monte-Carlo method.

To fit the energy envelopes of the S0128a event, we first estimate the tentative location of the source based on the difference of traveltime between P and S waves. This location depends on the velocities c^p and c^s. For a shear wave velocity of 3km/s in a Poisson solid and a difference of arrival time $T^s - T^p$ of 75s (compatible with the value $84 \pm 28s$ reported by the Mars Quake Service), the source would be at a distance of the order of 530km. Note however, that there are large uncertainties on this estimate. If the scattering is caused by a fractured medium, the velocity sensed by the waves could be much lower and, in turn, the event would be closer. As an example, for a shear wave velocity of 2.5km/s and a V_p/V_s ratio of 2, the hypocentral distance would be equal to 375km. Hence, our primary goal is not to locate precisely the event but rather to show that its characteristics are broadly compatible with a scattering hypothesis.

In a second step, we estimate a typical scattering mean free time and a typical absorption time of S waves using the diffusion analysis. If we extrapolate the trade-off relation (3) to 500km, we find a diffusivity in the range D =125.5—350km^2/s. The lower bound is actually quite close to the value we report below. We then simulate a series of random media with different correlation distance l_c but roughly the same diffusivity in order to match the data envelope by trial and error. We only use the horizontal components of the signal since they have the highest S/N ratio.

An example of envelope fit at a frequency of 7.5Hz is shown in Figure S3-6 (top panel). We find that the radiative transfer model, while not perfect, captures well the overall shape of the data envelope. In general, we find that strong forward scattering is required to appropriately fit the whole envelope including the two energy bursts. As an example, the model shown in Figure S3-6 uses the following parameter: $l_c = 500$m, $\kappa = 0.1$, $\nu = 0.2$, $\tau^s = 1.7$s, $\tau^p = 2.8$s, $\tau_i^s = 80$s. All these values are subject to trade-off that will be studied in future works. The value $\kappa = 0.1$ describes a medium rich in small-scale heterogeneities thought to be representative of heterogeneous media such as the crust (Sato, 2019). The choice $\nu = 0.2$ is somewhat arbitrary but has been reported for various rocks such as volcanic tuffs (Sato et al., 2012). The scattering mean free times are rather short, which means that the coherent waves are completely converted to coda waves at a distance of a few tens of kilometers from the source. This does not imply that all source information has been erased at the same distance though. The reason is that the scattering anisotropy in the model is rather strong with $\langle\cos(\theta^{SS})\rangle = 0.94$, $\langle\cos(\theta^{PP})\rangle = 0.9$ and $\langle\cos(\theta^{SP})\rangle = 0.54$, where $\langle\cos\theta^{\alpha\beta}\rangle$ is the mean cosine of the scattering angle for the α-to-β mode conversions. This implies that at each scattering event most of the energy is deflected in a small cone around the forward direction and explains why two energy packets can still be distinguished at large distance from the source.

From the scattering properties, we can deduce both the equivalent diffusivity and absorption time of a diffusion model (see Weaver, 1990; Margerin, 2012, for details): $D = 93$km^2/s, $t_i = 84.1$s, which is close to the one of shear waves ($t_i^s = 80$s). The fact that $t_i > t_i^s$ comes from the fact that coda waves spend roughly 10% of their time as P waves which have a larger absorption time than S waves. When translated to a quality factor, the inferred absorption time yields the relation $Q_i = 528f$, which agrees with the empirical relation proposed from the coda decay. Note that whereas the inferred diffusivity is strongly dependent on the assumed quake location, the absorption time is not. For instance, for a quake at 375km distance (as inferred if $V_s = 2.5$km/s and $V_p/V_s = 2$), the diffusivity is reduced by a factor roughly equal to 2 but the absorption time is essentially unchanged.

Figure S3-6 (bottom panel), shows on the same graph the contribution of P and S energy as well as the diffusion approximation to the radiative transfer model. The latter predicts seismically non-causal arrivals, which is a well-known feature of the diffusion model which has no upper bound for the group velocity. In the coda, the diffusion approximation matches the full solution rather well as expected. It is worth noting that except in a small time window at the onset of the signal, the energy is dominantly transported by shear waves, so that the first energy packet appears to be composed of P-to-S converted phases. This, in turn, may explain the drop of the V^2/H^2 ratio during the S0128a event. Note that a full-space multiple-scattering model predicts $V^2/H^2 = 0.5$ which is larger than the value of V^2/H^2 seen in the data at 7.5Hz. However, taking into account layering effects in the sub-surface may reconcile the two values (Margerin et al., 2009).

2.3 Discussion

2.3.1 Diffusivity.

Compared to other scattering environments, the diffusivity derived from the radiative transfer model appears intermediate. However, it should be kept in mind that all we can derive from a single measurement is an apparent value averaged over the volume sampled by the coda waves. If the scattering is associated with the presence of a fractured megaregolith, it may well be that the heterogeneity is strongly depth dependent with stronger scattering in the near-surface environment. Such complexities are currently not resolvable from the data. The assumed seismic wavespeeds also play a role in our estimate. Assuming slower velocities pushes the event closer to the station and entails a decrease of the diffusivity. Hence, the uncertainty on D remains large, all the more so as the location of the event is uncertain. We finally note that the parameters l_c, ν and κ cannot

be precisely determined as they are subject to trade-off.

2.3.2 Partitioning ratio

We have seen that a multiple-scattering model predicts well the drop of the V^2/H^2 ratio at 7.5Hz. However, it is important to note that the observed V^2/H^2 is actually frequency dependent and increases as frequency decreases. There are several possible interpretations of this observation. The simplest one is that the variation of the partitioning ratio is related to the signal-to-noise ratio. Since the noise has much more energy on the vertical component than on the horizontal ones, low S/N ratio would imply higher V^2/H^2 which agrees qualitatively with the observations. Another possibility is related to the stratification of the velocity or other not yet understood structural effects. Indeed, at the time of writing, a so far unexplained amplification of the signals has been detected at 2.4Hz, which appears to be stronger on the vertical than on the horizontal components. This would again contribute to the frequency dependence of V^2/H^2 but further investigations are needed to clarify the origin of the amplification.

2.3.3 Absorption

We have previously noted that the coda absorption time appears to be remarkably constant over the frequency band of interest. This is equivalent to stating that the coda quality factor varies linearly with frequency. Such a simple feature is in fact well predicted by the model of energy leakage (Dainty et al., 1974; Margerin et al., 1999). In this model, besides dissipation, the exponential decay of the coda is explained by the transmission of energy from a heterogeneous scattering crust to a transparent mantle. In the diffusion regime, the leakage quality factor Q_l may be expressed as:

$$Q_l = \frac{2\pi H^2 f}{D\xi^2} \tag{5}$$

where D is the diffusivity, H is the thickness of the scattering layer and ξ is a parameter which depends on the contrast of elastic properties at the crust/mantle boundary but is bounded between 0 and $\pi/2$ (Margerin et al., 1999). If the diffusivity does not vary significantly in the frequency band of interest, leakage predicts an apparent coda decay which is proportional to frequency, in good agreement with our data. If we assume that the velocity contrast between crust and mantle is similar on Mars and on Earth, the computations of Margerin (2017) (Figure 4, left-hand panel) suggest that for a diffusivity $D = 90\text{km}^2/\text{s}$, a scattering anisotropy of 0.9 and a crustal thickness in the range 30km-90km, the leakage effect would be negligible so that the decay time of the S0128a event could be almost entirely ascribed to absorption. However, if only a trade-off between diffusivity and hypocentral distance is considered as significant, the decay rate of S0128a could be entirely explained by leakage by appropriately tuning the mean free path with respect to the crustal thickness. This would imply that absorption is negligible in the crust. In any case, leakage implies that our estimates of the absorption quality factor Q_i should be interpreted as a lower bound only. In order to confirm the absorption level in the crust, we investigate in the next section two teleseismic events, which offer an independent estimate of the scattering and attenuation properties of the crust.

3 Teleseismic Events (S0173a and S0235b)

3.1 Data analysis

3.1.1 Polarization analysis

The S0173a and S0235b events are more than 10-minute long signals emerging from the ambient noise in the 0.2-0.9Hz frequency band. S0235b also appears to have energy at higher frequencies but with a signal-to-noise ratio, which is very low. Because the two events share similar characteristics we present the analysis for only one of the two. Figure S3-7 presents an analysis of the polarization characteristics of the S0173a event. One observes a first arrival with an approximately linear polarization that lasts during roughly 10 seconds, which is compatible with a P wave. This P wave can be detected in the entire frequency band 0.2Hz-0.7Hz with a high degree of polarization (DOP). The corresponding semi-major azimuth is mostly E-W (93.0°) and the incident angle is 27.4°. The P wave arrival is followed by a coda with a duration of about 3 minutes, which is disrupted by a second more energetic arrival that is compatible with an S wave arrival. The S-wave polarization is more complex and associated with a lower DOP. Over a short duration of 10s in the frequency band 0.3Hz-0.4 Hz, the semi-major azimuth is about N-S (181.4^o) and the incident angle is 77.6° whereas in the frequency band 0.4-0.7Hz, the semi-major azimuth is 163.1° and the incident angle is 79.1°.

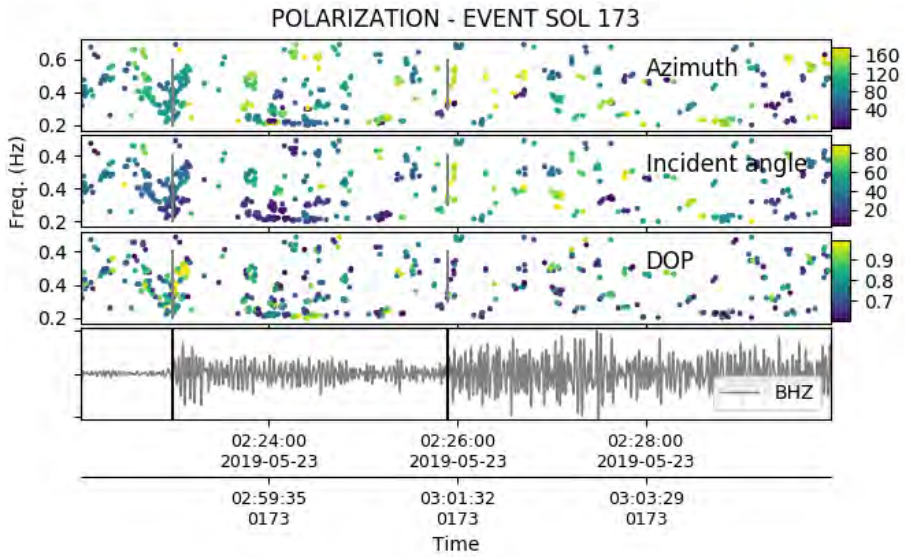

Figure S3-7: Polarization analysis of the S0173a event as a function of time and frequency. The upper time axis is in UTC and the lower axis is in LMST. Eigen-analysis of the 3 component cross-spectra as a function of time and frequency enables to determine the characteristics of the ellipse of polarization that best fit the ground motion. Here we select ellipses with linearity larger than 0.5. The first and second panels show the semi-major axis azimuth and the semi-major axis incident angle with respect to the vertical in degrees. The stability of the measurement is given by the degree of polarization (third panel). It is computed as in Schimmel et al. (2011), and can vary between 0 and 1. The bottom panel is the vertical component seismic trace filtered in the frequency band 0.1-0.9 Hz (0-phase filter). Vertical lines are the P and S arrival times.

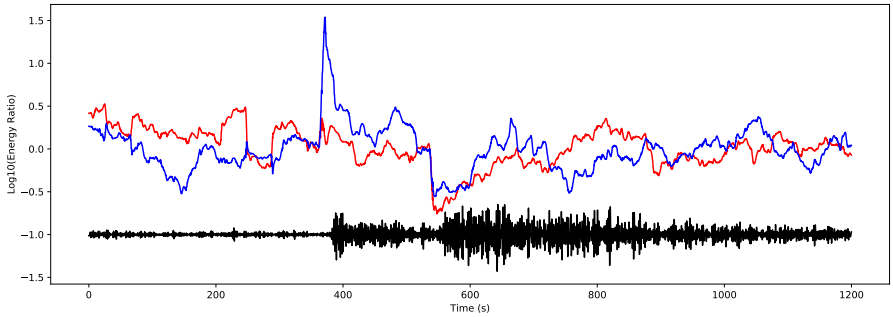

Figure S3-8: Energy partitioning of the S0173a event at 0.5Hz. Red: V^2/H^2, blue: E^2/N^2. The vertical component of the velocity is also shown in inset (arbitrary units). Note the logarithmic scale on the energy ratio axis.

3.1.2 Energy partitioning

The polarization analysis is very compatible with the energy partitioning ratios shown in Figure S3-8. At the onset of the signal the kinetic energy is predominantly on the $E-W$ component, which agrees with a back-azimuth of approximately 90 degrees. The kinetic energy of the S-arrival appears to be predominantly distributed on the $N-S$ component, which is most logically explained as a shear wave with an SH signature. The S wave is followed by a coda lasting several hundreds of seconds, in which it is difficult to discern other coherent arrivals. The travel time difference between plausible P and S waves is of the order of 3 minutes, which suggests that the source of S0173a is located at a teleseismic distance of the order of 28-30 degrees (1650km-1750km according to Giardini et al., 2020).

The long-lasting coda, as well as the overall lack of polarization of the signal -apart from the two main arrivals- is an indication that some scattering is involved in the generation of the S0173a waveforms. It is also worth noting that the frequency bands of the S0128a and S0173a events do not overlap. In comparison to S0128a, the S0173a event is depleted in high-frequencies although it enjoys a much higher S/N ratio, typically larger than 10. The lack of high-frequency as well as the observation of relatively distinct ballistic arrivals strongly suggests that S0173a has propagated in a more attenuating and less scattering medium than S0128a before reaching the InSight station. The ensemble of *a-priori* models of seismic attenuation presented by Smrekar et al. (2018) seem to favor the idea that most of the propagation of S0173a occurred in the mantle and that the

excitation of coda waves occurs as the teleseismic waves impinge on a shallow scattering layer. This scenario becomes our working hypothesis in the modeling section. Finally we note that, from the point of view of Earth standards, S0173a is a curiosity. Indeed, the 1-10s period band is the realm of ocean generated micro-seismic noise on Earth. This very energetic signal usually hampers the detection of weak seismic events. For this reason, our knowledge of attenuation in the 1s-10s period band on Earth is limited.

3.1.3 Coda quality factor

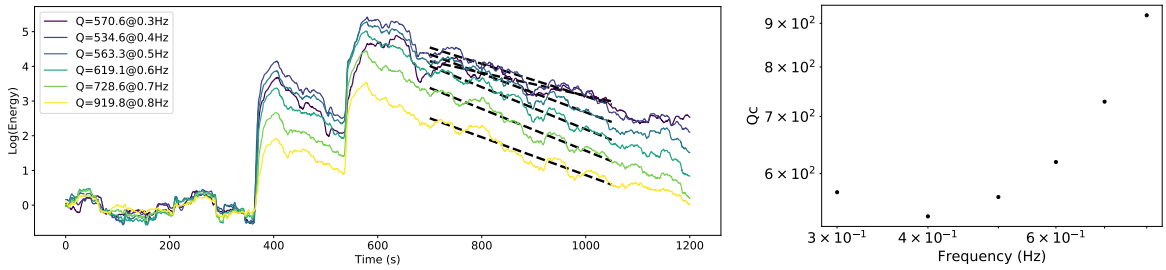

Figure S3-9: Analysis of the frequency dependent coda quality factor Q_c of the S0173a event. Left: Logarithm of energy envelopes as a function of time and fit of the coda decay. The different colors correspond to different frequency bands. Right: frequency dependence of Q_c in the 0.3Hz-0.8Hz frequency band.

The noise corrected and de-glitched seismogram energy envelopes in successive frequency bands $[2f/3, 4f/3]$ with $f \in \{0.3, 0.4, 0.5, 0.6, 0.7, 0.8\}$ are represented in Figure S3-9 (left). This figure shows S/N ratio is highest around 0.4-0.5Hz. In Figure S3-9 (right), we show the S coda quality factor between 0.3Hz and 0.8Hz. The frequency dependence is more complex than for the S0128a event. Q_c seems to plateau around a mean value of 557 ± 23 at frequencies lower than 0.5Hz and then increases rapidly to reach a value of about 900 at 0.8Hz. For frequencies above 0.5Hz, the coda quality factor shows an approximately linear increase of the form $Q_c = Q_0 f^n$, with $Q_0 = 1098 \pm 79$ with $n = 1.03 \pm 0.17$. Extrapolated to a nominal frequency of 1Hz, the coda quality factor of the S0128a and S0173a differ by a factor roughly equal to 2. For teleseismic events, the interpretation of Q_c in terms of scattering and attenuation properties is ambiguous (Korn, 1990). Therefore, we propose below a simple modeling of the S wave energy envelope to estimate the propagation properties in the crust.

3.2 Envelope inversion of teleseismic events

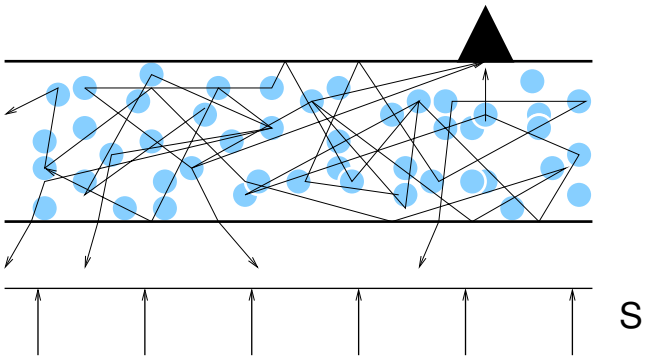

Figure S3-10: Schematic view of the propagation model for the S0173a event. S denotes the incoming plane shear wave from below the station. Scattering is confined to a shallow layer. Scatterers are represented by the blue circles, with possible raypaths of scattered waves indicated by the lines.

Based on the observations summarized above, we propose a simple conceptual model to explain the S0173a and S0235b events (see Figure S3-10). A coherent teleseismic plane wave is incident from below the station. As the plane wave propagates and reverberates in the heterogeneous layer, scattered waves are excited giving rise to a seismic coda. The observation of coherent waves discards the possibility to model the seismogram envelope with a diffusion equation. We shall therefore consider a radiative transfer model. For simplicity, we focus primarily on the dominant S wave arrival and deactivate the coupling with P waves. Furthermore, we make the assumption that the scattering can be considered as isotropic in a first approximation. This hypothesis contrasts with the one adopted for S0128a but is not necessarily contradictory. Indeed, the scattering pattern is strongly frequency dependent and tends to become isotropic as the frequency decreases (Sato et al., 2012).

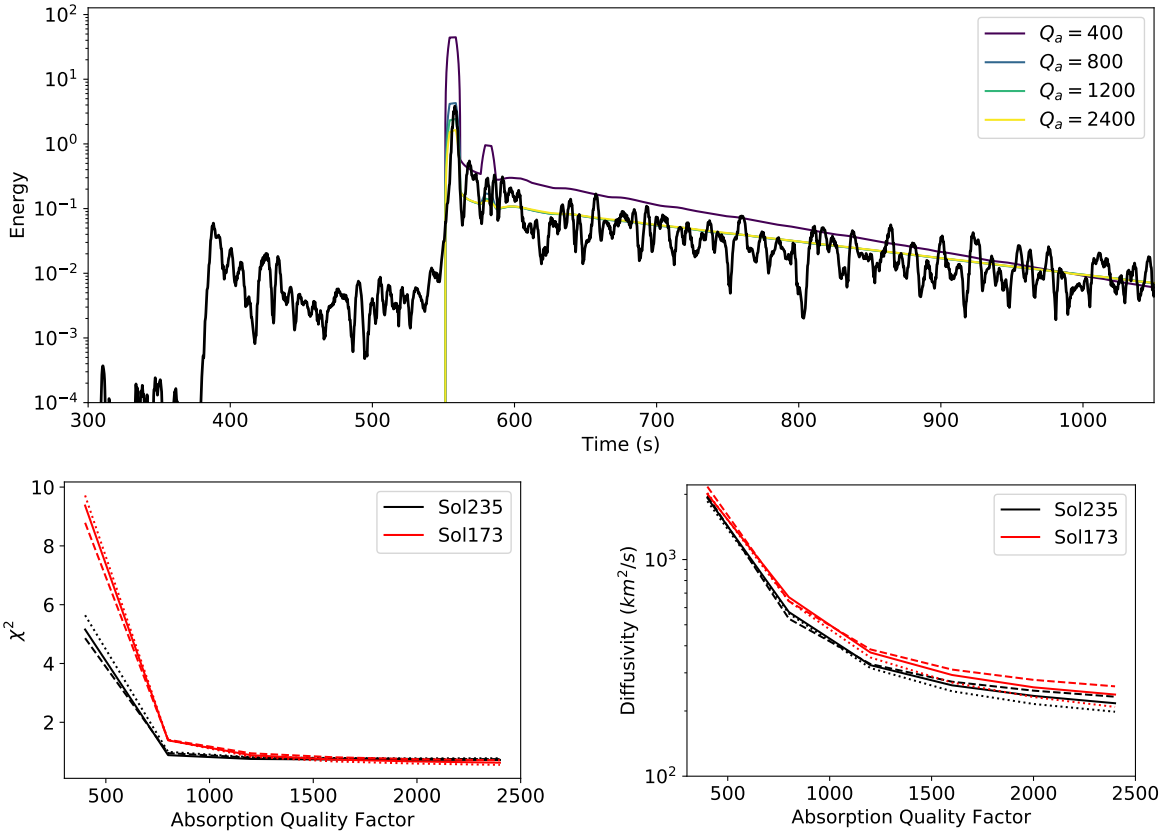

Figure S3-11: Constraint on Diffusivity and Absorption from envelope modeling of the S0173a and S0235b events. The top panel shows the smoothed total kinetic energy envelope of the S0235b event (black line) as well as the best fitting Radiative Transfer models obtained for different values of the absorption quality factor (see inset). The assumed layer thickness is 40kms and the velocity contrast is 3/4.2. The lower panels show the dependence of the minima of the misfit function χ^2 (left) and of the diffusivity D (right) on the absorption quality factor. The dashed, solid and dotted lines correspond to increasing crustal thickness: $H = 20, 40, 60$km.

For a correlation distance of 500m and a typical wavelength of 6km for S waves at 0.5Hz, isotropic scattering is a reasonable first guess. Reverberations are taken into account by introducing a velocity jump at the lower boundary of the model. Different velocity contrasts and crustal thickness were tested with $c^s = 3$—3.2km/s in the upper part and $c^s = 4.2$—4.5km/s in the lower part. The attenuation of the coda takes place through two processes: leakage of energy back to the mantle and absorption of seismic energy. In spite of the considerable simplification of the physics, both effects are taken into account in the modeling. An important unknown parameter is the thickness of the scattering layer H. Here, we use a pragmatic approach and interpret the data assuming $H = 20$km, 40km and 60km. We are then only left with two free parameters: the scattering mean free time and absorption time of S waves τ^s and t_i^s, or equivalently the diffusivity D and absorption quality factor Q_i of shear waves.

To invert for D and Q_i, we first cut the signal into non-overlapping time windows and measure the following energy integrals:

$$\begin{aligned} E_j &= \int_{T^s+(j-1)\Delta t}^{T^s+j\Delta t} \left(V^2(t) + H^2(t)\right) dt \; j = 1, \cdots, 25 \\ E_n &= \int_{T^s+600s}^{T^s+400s} \left(V^2(t) + H^2(t)\right) dt, \end{aligned} \tag{6}$$

where $\Delta t = 15$s is the window duration, and T^s is the arrival time of the ballistic S wave. The averaging procedure smooths out the fluctuations of the signal envelopes. The purpose of the last time window is to normalize the signal for the magnitude of the source and for site effects. This procedure is known as 'Coda Normalization' and has proven very effective in attenuation studies (Aki & Chouet, 1975; Rautian & Khalturin, 1978). We then seek to minimize the difference between the observed and theoretically predicted normalized

energies using the following norm:

$$\chi^2(\tau^s, t_i^s) = \sum_j \left(\log\left(\frac{E_j}{E_n}\right) - \log\left(\frac{E_j^{RT}(\tau^s, t_i^s)}{E_n^{RT}(\tau^s, t_i^s)}\right)\right)^2, \quad (7)$$

where $E_j^{RT}(\tau^s, t_i^s)$ denotes the energy integrals predicted by the radiative transfer model for a set of scattering/absorption mean free times. To achieve the best fit between data and model, we follow the idea of Carcolé & Sato (2010) and employ the Levenberg-Marquardt algorithm. The partial derivatives of the observables with respect to the model parameters are computed using a differential Monte-Carlo approach (Lux & Koblinger, 1991). These computations are instructive since they show that the sensitivity to absorption is about 2 orders of magnitude larger than the sensitivity to scattering. This lack of sensitivity to scattering seems to be related to the plane wave incidence but further investigation is needed. To address the trade-off between absorption and energy leakage, we perform a series of inversions where we fix the value of $Q_i \in \{400, 800, 1200, 1600, 2000, 2400\}$ and invert for D alone. The lowest and highest values of Q_i correspond, respectively, to Earth-like (hydrated lithosphere) and Moon-like (dehydrated lithosphere) situations. In Figure S3-11, we present the results of the inversions for both S0173a and S0235b, assuming a velocity contrast 3/4.2 at the bottom of the scattering layer. The top plot allows the reader to compare the predicted and observed envelopes for $H = 40$km and different values of Q_i. It is apparent that for $Q_i \geq 800$, all scattering models explain equally well the data. This is confirmed in the plot of the misfit function χ^2 as a function of the quality factor Q_i for different crustal thicknesses. We observe a clear drop of χ^2 for $Q_i = 800$, suggesting that this value is the most probable lower bound for Q_i around 0.5Hz. We also illustrate the dependence of the diffusivity on the assumed value of absorption. Our inversions suggest $D \geq 200\text{km}^2/\text{s}$ at 0.5 Hz.

3.3 Discussion.

A general uncertainty in our analysis comes from the fact that we have considerably reduced the complexity of the incoming wavefield by not considering the P-wave. Furthermore, we cannot exclude that energy is being injected into the crust by other phases that have failed to be detected.

3.3.1 Diffusivity.

There is a factor 2.5 to 5 difference between the diffusivity estimated from the regional event S0128a and from the teleseismic events S0173a-S0235b. This gap may naturally be explained by the difference in frequency bands: around 0.5Hz for S0173a-S0235b and around 7Hz for S0128a in the framework of scattering theory. Indeed, calculation of the diffusion constants of elastic waves in Von-Karman type inhomogeneous media generally show a decrease of the diffusivity with frequency, which in the details depends on the richness of the medium in small-scale heterogeneities (Sato et al., 2012). We also note that the diffusivity is only marginally sensitive to the crustal thickness. The trade-off between diffusivity and absorption is further discussed below.

3.3.2 Absorption.

Absorption is strongly correlated with scattering properties. In other words, the trade-off between absorption and energy leakage can only be partially lifted. A lower bound of 800 for the absorption quality factor at 0.5Hz is obtained independently for S0173a and S0235b which is encouraging. Only a better constraint on the diffusivity and velocity structure of the crust could further reduce the range of admissible Q_i.

4 Comparison with Earth and Moon

In Figure S3-12 we show a preliminary comparison between the scattering and absorption properties of Earth, Moon and Mars. The left-hand panel shows the distribution of diffusivity and intrinsic quality factor at 1.5Hz in various geological media on Earth. The seismological literature rarely uses diffusivity to quantify the scattering attenuation on Earth, at the exception of volcanic areas. Therefore, we have converted the scattering quality factor Q_{sc} to diffusivity using the formula $D = c^2 Q_{sc}/3\omega$, with $\omega = 2\pi \times 1.5$ and $c = 3$km/s. The factor 3 in the denominator corresponds to the space dimension. For Mars, we have reported the estimates of the diffusivity and absorption at 0.5Hz (filled red squares) and at 7Hz (filled red square with error bars). For the Moon, attenuation has been estimated in the 0.5Hz-1.5Hz frequency band. The seismograms on the right-hand side illustrate the variability of waveforms depending on the strength of scattering and attenuation. The diffusivity, although not well constrained, appears to be moderate. However, the reported values are not necessarily representative of the possible lateral and depth variability. Attenuation is not strong but the observed coda durations are shorter than on the Moon. The estimated lower bound of absorption is compatible with the presence of small amounts of volatiles in the crust of Mars.

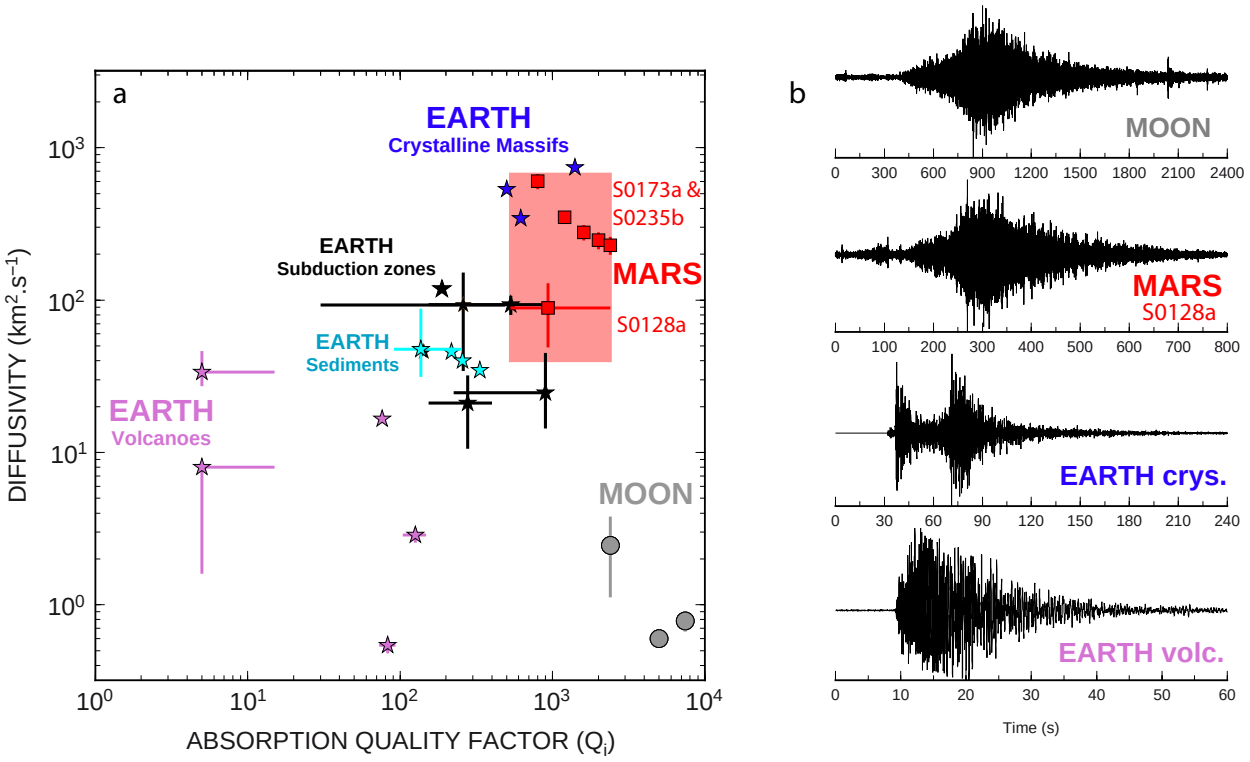

Figure S3-12: Comparison of seismic scattering and attenuation on Earth Moon and Mars. a: Diffusivity and attenuation. Except for Mars and the Moon the diffusivity is given in the 1-2Hz frequency band. See the text for details. b: Several illustrative seismograms showing the impact of the geological environment on the anatomy of the seismogram. Figure compiled after the following articles: Mayeda et al. (1992), Ugalde et al. (2010), Wegler (2003), Del Pezzo et al. (2001), Badi et al. (2009), Hoshiba et al. (2001), Yoshimoto et al. (2006), Lemzikov (2007), Chung et al. (2009), Lacombe et al. (2003), Sens–Schönfelder et al. (2009), Sens-Schönfelder & Wegler (2006), Carcolé & Sato (2010), Pujades et al. (1997), Dainty et al. (1974), Gillet et al. (2017), Menina (2019).

References

Aki, K. & Chouet, B., 1975. Origin of coda waves, sources and attenuation, *Journal of Geophysical Research*, **80**, 3322–3342.

Akkermans, E. & Montambaux, G., 2007. *Mesoscopic Physics of Electrons and Photons*, Cambridge University press, Cambridge.

Badi, G., Del Pezzo, E., Ibanez, J., Bianco, F., Sabbione, N., & Araujo, M., 2009. Depth dependent seismic scattering attenuation in the nuevo cuyo region (southern central andes), *Geophysical Research Letters*, **36**(24).

Carcolé, E. & Sato, H., 2010. Spatial distribution of scattering loss and intrinsic absorption of short-period S waves in the lithosphere of Japan on the basis of the Multiple Lapse Time Window Analysis of Hi-net data, *Geophysical Journal International*, **180**(1), 268–290.

Chung, T. W., Lees, J. M., Yoshimoto, K., Fujita, E., & Ukawa, M., 2009. Intrinsic and scattering attenuation of the Mt Fuji Region, Japan, *Geophysical Journal International*, **177**(3), 1366–1382.

Dainty, A. M., Toksoz, M. N., Anderson, K. R., Pines, P. J., Nakamura, Y., & Latham, G. V., 1974. Seismic scattering and shallow structure of the Moon in Oceanus Procellarum, *Moon*, **9**, 11–29.

Del Pezzo, E., Bianco, F., & Saccorotti, G., 2001. Separation of intrinsic and scattering q for volcanic tremor: An application to etna and masaya volcanoes, *Geophysical research letters*, **28**(16), 3083–3086.

Giardini, D., Lognonné, P., Pike, T., Banerdt, B., Christensen, U., & al., 2020. The seismicity of mars, *Nature Geosciences*, **This Issue**.

Gillet, K., Margerin, L., Calvet, M., & Monnereau, M., 2017. Scattering attenuation profile of the Moon: Implications for shallow moonquakes and the structure of the megaregolith, *Physics of the Earth and Planetary Interiors*, **262**, 28–40.

Hennino, R., Trégourès, N., Shapiro, N. M., Margerin, L., Campillo, M., van Tiggelen, B. A., & Weaver, R. L., 2001. Observation of equipartition of seismic waves, *Physical Review Letters*, **86**, 3447–3450.

Hoshiba, M., Rietbrock, A., Scherbaum, F., Nakahara, H., & Haberland, C., 2001. Scattering attenuation and intrinsic absorption using uniform and depth dependent model–Application to full seismogram envelope recorded in Northern Chile, *Journal of seismology*, **5**(2), 157–179.

Korn, M., 1990. A modified energy flux model for lithospheric scattering of teleseismic body waves, *Geophysical Journal International*, **102**, 165–175.

Lacombe, C., Campillo, M., Paul, A., & Margerin, L., 2003. Separation of intrinsic absorption and scattering attenuation from Lg coda decay in central France, *Geophysical Journal International*, **154**, 417–425.

Lemzikov, V., 2007. Intrinsic attenuation and scattering of shear waves in the lithosphere of Kamchatka, *Journal of Volcanology and Seismology*, **1**(3), 185–197.

Lux, I. & Koblinger, L., 1991. *Monte Carlo particle transport methods: neutron and photon calculations*, CRC Press.

Margerin, L., 2012. Diffusion approximation with polarization and resonance effects for the modelling of seismic waves in strongly scattering small-scale media, *Geophysical Journal International*, **192**(1), 326–345.

Margerin, L., 2017. Computation of Green's function of 3-D radiative transport equations for non-isotropic scattering of P and unpolarized S waves, *Pure and Applied Geophysics*, **174**(11), 4057–4075.

Margerin, L., Campillo, M., Shapiro, N., & van Tiggelen, B. A., 1999. Residence time of diffuse waves in the crust as a physical interpretation of coda Q : application to seismograms recorded in Mexico, *Geophysical Journal International*, **138**, 343–352.

Margerin, L., Campillo, M., Van Tiggelen, B., & Hennino, R., 2009. Energy partition of seismic coda waves in layered media: Theory and application to Pinyon Flats Observatory, *Geophysical Journal International*, **177**(2), 571–585.

Mayeda, K., Koyanagi, S., Hoshiba, M., Aki, K., & Zeng, Y., 1992. A comparative study of scattering, intrinsic, and coda Q^{-1} for Hawaii, Long Valley, and central California between 1.5 and 15.0 Hz, *Journal of Geophysical Research: Solid Earth*, **97**(B5), 6643–6659.

Menina, S., 2019. *Inversion of the attenuation and scattering of the seismic data of Apollo: comparison Earth - Moon - Mars*, Master's thesis, Institut de Physique du Globe de Paris, Paris, France.

Obara, K. & Sato, H., 1995. Regional differences of random inhomogeneities around the volcanic front in the Kanto-Tokai area, Japan, revealed from the broadening of S wave seismogram envelopes, *Journal of Geophysical Research*, **100**, 2103–2121.

Pujades, L., Ugalde, A., Canas, J., Navarro, M., Badal, F., & Corchete, V., 1997. Intrinsic and scattering attenuation from observed seismic codas in the Almeria Basin (southeastern Iberian Peninsula), *Geophysical Journal International*, **129**(2), 281–291.

Rautian, T. & Khalturin, V., 1978. The use of the coda for determination of the earthquake source spectrum, *Bulletin of the Seismological Society of America*, **68**(4), 923–948.

Sato, H., 2019. Power spectra of random heterogeneities in the solid earth, *Solid Earth*, **10**(1), 275–292.

Sato, H., Fehler, M. C., & Maeda, T., 2012. *Seismic wave propagation and scattering in the heterogeneous earth*, vol. 496, Springer.

Schimmel, M., Stutzmann, E., Ardhuin, F., & Gallart, J., 2011. Polarized Earth's ambient microseismic noise, *Geochemistry, Geophysics, Geosystems*, **12**(7).

Sens-Schönfelder, C. & Wegler, U., 2006. Radiative transfer theory for estimation of the seismic moment, *Geophysical Journal International*, **167**, 1363–1372.

Sens–Schönfelder, C., Margerin, L., & Campillo, M., 2009. Laterally heterogeneous scattering explains Lg blockage in the Pyrenees, *Journal of Geophysical Research*, **114**, B07309.

Shapiro, N. M., Campillo, M., Margerin, L., Singh, S. K., Kostoglodov, V., & Pachero, J., 2000. The energy partitionning and the diffuse character of the seismic coda, *Bulletin of the Seismological Society of America*, **90**, 655.

Smrekar, S. E., Lognonné, P., Spohn, T., Banerdt, W. B., Breuer, D., Christensen, U., Dehant, V., Drilleau, M., Folkner, W., Fuji, N., Garcia, R. F., Giardini, D., Golombek, M., Grott, M., Gudkova, T., Johnson, C., Khan, A., Langlais, B., Mittelholz, A., Mocquet, A., Myhill, R., Panning, M., Perrin, C., Pike, T., Plesa, A.-C., Rivoldini, A., Samuel, H., Stähler, S. C., van Driel, M., Van Hoolst, T., Verhoeven, O., Weber, R., & Wieczorek, M., 2018. Pre-mission insights on the interior of mars, *Space Science Reviews*, **215**(1), 3.

Ugalde, A., Carcolé, E., & Vargas, C. A., 2010. S-wave attenuation characteristics in the Galeras volcanic complex (south western Colombia), *Physics of the Earth and Planetary Interiors*, **181**(3-4), 73–81.

Weaver, R. L., 1990. Diffusivity of ultrasound in polycrystals, *J. Mech. Phys. Solids*, **38**, 55–86.

Wegler, U., 2003. Analysis of multiple scattering at Vesuvius volcano, Italy, using data of the TomoVes active seismic experiment, *Journal of volcanology and geothermal research*, **128**(1-3), 45–63.

Yoshimoto, K., Wegler, U., & Korn, M., 2006. A volcanic front as a boundary of seismic-attenuation structures in northeastern Honshu, Japan, *Bulletin of the Seismological Society of America*, **96**(2), 637–646.

Supplementary Material 4

B. Knapmeyer-Endrun, B. Tauzin, M. Panning, D. Antonangeli, F. Bissig, P. M. Davis, R. Joshi, A. Khan, M. Knapmeyer, V. Lekić, P. Lognonné, L. Pan, C. Perrin, B. Pinot, J.-R. Scholz, S. C. Stähler, S. Tharimena, C. Beghein, N. Fuji, M. P. Golombek, J. Irving, A. Jacob, R. Garcia, C. Michaut, C. Quantin-Nataf

S4-1: Deglitching

Broad-band glitches have been observed in both VBB and SP data. Their signal properties and the methods developed to remove them from the data are discussed in more detail in Supplementary Material 5. As a glitch occurred on all three components of the VBB data about 15 s after the P-wave onset of S0173a, application of these deglitching methods was also necessary before the calculation of receiver functions (RFs). This allows for comparing the effects of the deglitching algorithms (Figure S4-1) on the resulting RFs (Figure S4-2a). Methods labelled IPGP, UCLA and ISAE here are based on the instrument transfer function approach, while the method labelled MPS is using a discrete wavelet transform.

S4-2: Receiver Function Methods

Here the five techniques used to calculate RFs for the two broadband events are detailed. Method A is a probabilistic technique, which produces an ensemble of RFs. Methods B-E provide a range of different deterministic RFs, some of which employ multiple sub-techniques (e.g. Figure S4-3 for S0173a). All methods are applied to each of the four deglitched datasets for S0173a (Figure S4-1) and methods A, C, D and E are also applied to S0235b. Figure S4-2 shows RFs calculated using methods B-E gathered by common deglitching technique in part **a** and by common processing method in part **b**. Methods D and E provide transverse RFs in addition to the radial RFs, although these do not show any clear phases above the amplitude of the noise (Figure S4-5).

Supplementary Method A: Data were rotated to the Z-R-T system and bandpass-filtered between 0.1 and 1.0 Hz. Upgoing P and SV waveforms were obtained from the Z and R waveforms for the P-wave coda by applying a free-surface transfer matrix[1]. The free-surface transfer matrix

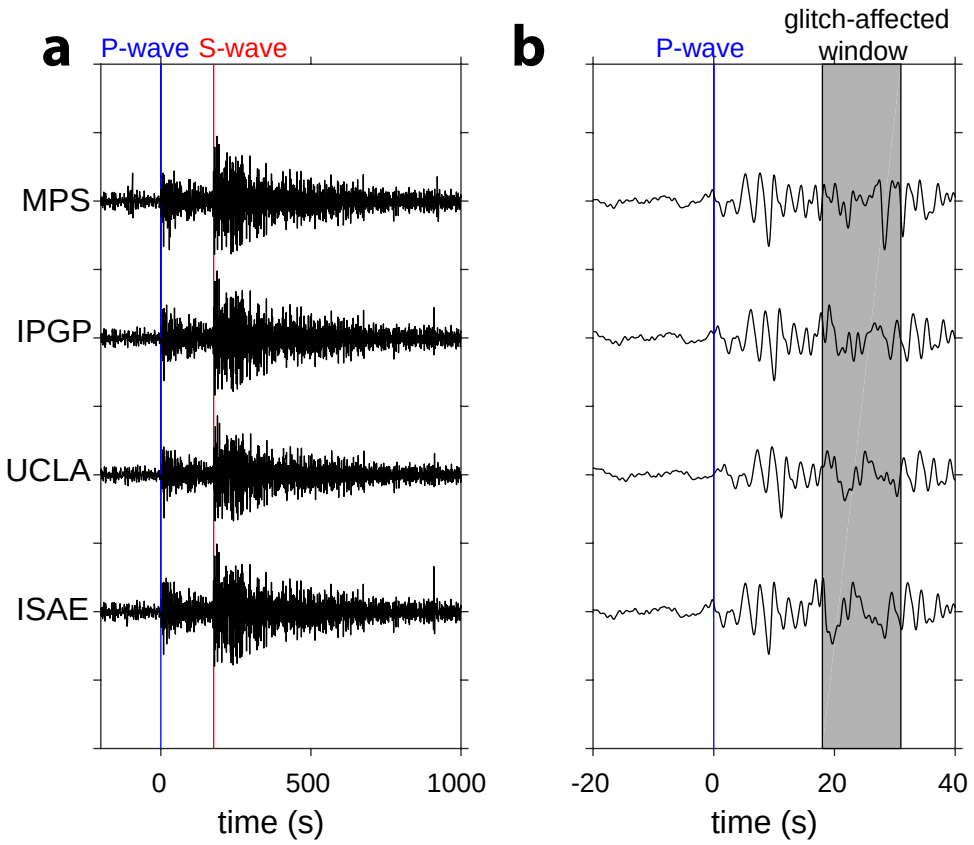

Figure S4-1. Comparison of different deglitched versions of the S0173a P-wave train recorded on the vertical component of SEIS. Traces are marked by the institution where the corresponding deglitching algorithm was developed. **a** Time window showing both P- and S-wave trains. **b** Zoom-in of P-wave train. The records have been filtered with a 4th-order Butterworth filter with 0.1-1.0 Hz passband. The P- and S-wave onsets have been picked and the records subsequently aligned on the P-wave. The time window affected by the glitch is emphasized in gray.

depends on the ray parameter and near-surface P- and S-wave velocities, which we estimate by minimizing the energy on the SV component during the first 2 seconds of the P-wave arrival, following the approach of Abt et al[2]. To obtain the RFs and assess uncertainty, we apply the trans-dimensional hierarchical Bayesian deconvolution (THBD) method[3] to deconvolve the first 15 s of the P waveform from the SV waveform. The method uses a reversible jump Markov Chain Monte Carlo algorithm to sample one million random realizations of RFs, represented by Gaussians of unknown width, lag-time, and amplitude. The number of these pulses in the RFs is an unknown determined during the sampling process. Because the level of complexity in the RFs that is justified by the data depends on noise levels, these are also estimated during the sampling process. The

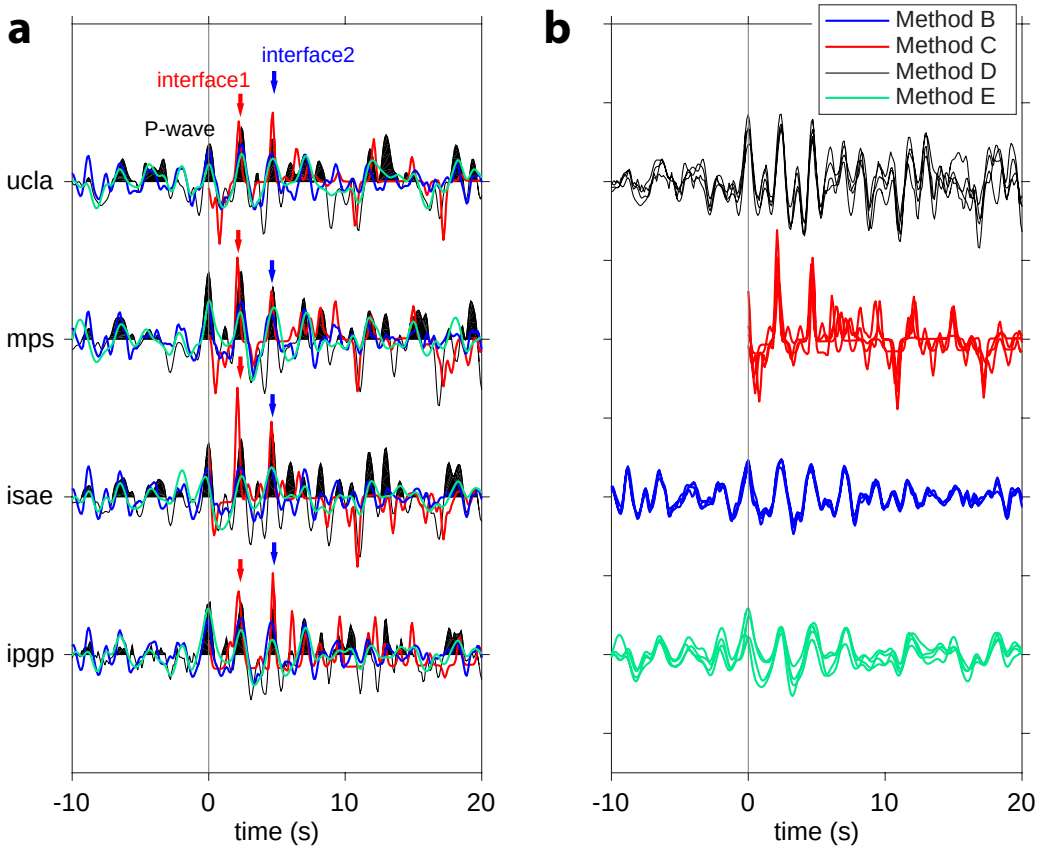

Figure S4-2. Comparison of radial RFs for S0173a for **a** different deglitching methods (UCLA, MPS, ISAE, IPGP) and **b** different processing methods (B-E).

THBD method yields an ensemble of RFs compatible with the data; features common across the ensemble can be considered robust. The result of THBD is shown in Figure 6c in the main text.

Supplementary Method B: Data were rotated to the Z-N-E system and bandpass-filtered between 0.1 and 1.0 Hz. The optimum back-azimuth was determined by polarization analysis within a time window of 7 s length from the P-wave onset, resulting in values between 89.2 and 91.8° for the different deglitched data sets. Three different methods of deconvolution were tested: (i) water-level deconvolution[4], (ii) iterative time-domain deconvolution[5], and (iii) spectral whitening and auto- and cross-correlation[6;7]. The comparison between RFs obtained with these three methods is shown in Figure S4-3. The vertical component waveform, 10 s before until 100 s after the onset of the P-wave, was used as source function in each case. Different lengths of the source functions were tested and found to give similar results. For the water-level deconvolution, the water level was set to c=10^{-3} and a parameter of a = 5.0 rad/s to determine the width of the Gaussian fil-

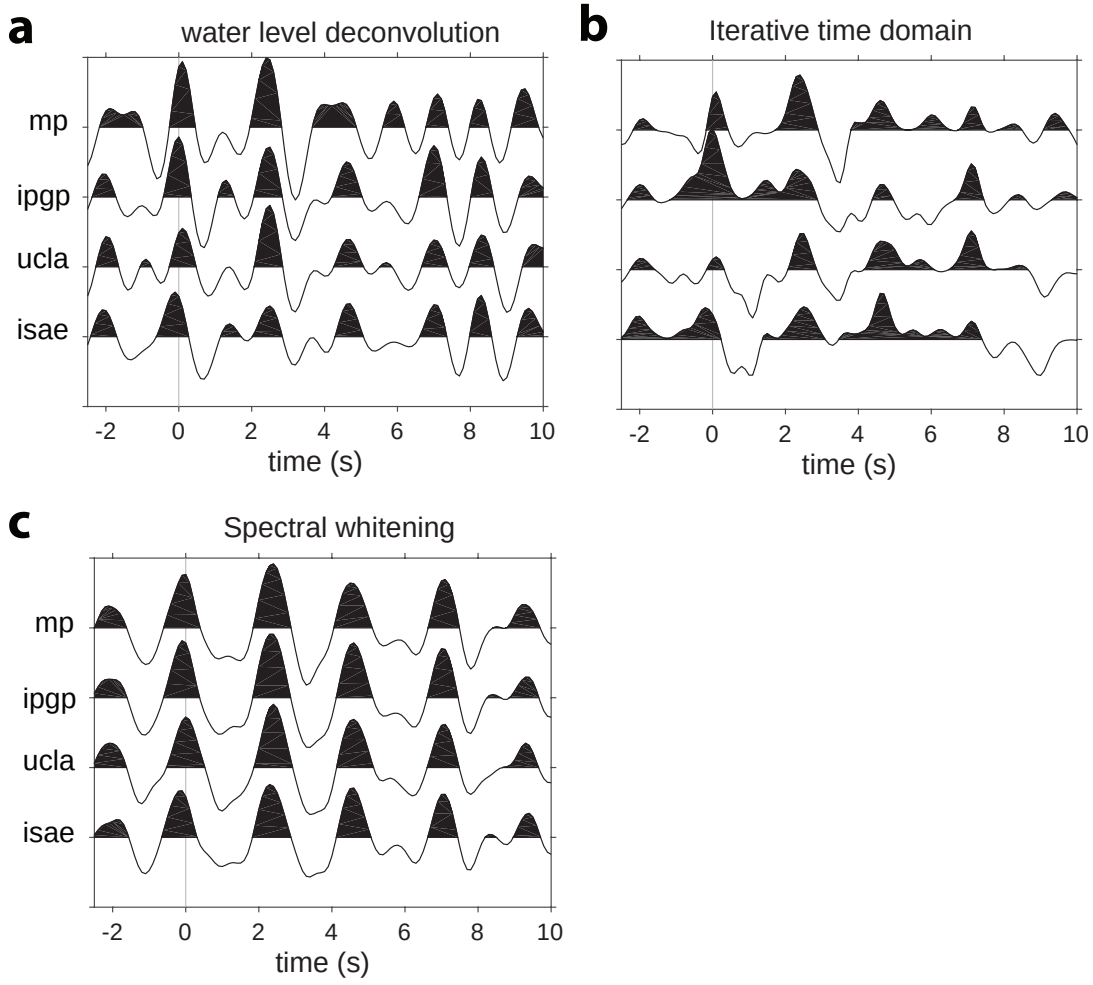

Figure S4-3. Comparison of radial RFs for S0173a for the different processing methods described in Supplementary Method B.

ter was used. A second-order Butterworth high-pass with a cut-off of 0.5 Hz was applied to the resulting waveforms. For the iterative time-domain deconvolution, a pulse width of 0.5 s at half the maximum amplitude was used for the Gaussian pulses that make up the RF waveform. For the deconvolution by spectral whitening and correlation, the processing used a width of W=0.7 Hz for the frequency window used to smooth the vertical component spectrum. In contrast to the other methods, the iterative time-domain deconvolution tends to give plateaus of zero amplitude in-between pulses, whatever the number of pulses chosen for the RFs. Figure S4-2 and Figure 6b include the results for spectral whitening and cross-correlation.

Supplementary Method C: The deglitched data were corrected for instrument response in the U-V-W system, and the resulting velocity seismograms were trimmed to 5 min before the P-wave

arrival and 5 min after the S-wave arrival as reported by MQS. Data were rotated to the Z-N-E system and then the Z-R-T system, using back-azimuths of 91° and 74°, respectively, based on the event locations reported by MQS. Data were bandpass filtered between 1 and 10 s. To calculate the RFs, iterative time-domain deconvolution[5] and extended-time multi-taper frequency domain deconvolution[8] methods were tested. For iterative time-domain deconvolution, the waveform in a time window 0s to 60s after the P-wave arrival on the vertical component was chosen as source function and a Gaussian filter parameter of 5 rad/s was used. For the extended-time multi-taper deconvolution, the source waveform was chosen on the vertical channel by manually selecting a window around the visible P-wave arrival. Deconvolution is then performed using a 30s window, a time-bandwidth product of 3 (translating to a frequency bandwidth of permissible spectral leakage of 0.2 Hz), and 4 tapers[9]. For both methods, the source function was deconvolved from the radial component in the Z-R-T system. Different time windows for the source function were tested and found to produce similar results. Figure S4-2 and Figure 6b include the results for iterative time-domain deconvolution.

Supplementary Method D: The transfer functions of the individual VBB components were removed from the deglitched data in the U-V-W system and the data were filtered between 0.1 and 2 Hz, the frequency band that contains the main energy of the events. Additional restitution of the data to ground displacement led to similar results. Data were then rotated to the Z-N-E and Z-R-T system, using the back-azimuths of 91° and 74° based on the event locations by MQS. RFs were calculated by using a time-domain Wiener filter that transforms the complex P-wavetrain on the Z component into a band-limited spike[10;11]. This Wiener filter was applied to all three components of the seismogram. Various window lengths for the P-wave train, damping factors, and spike positions within the window were compared (see examples for S0173a in Figure S4-4). The parameters used are a deconvolution window length of 35-40 s, with the spike position at the centroid of the signal (i.e. at 16-17 s), and a damping factor of 0.5. Whereas a lower damping results in more high-frequency noise, a damping larger than 1 leads to a significant increase of the side-lobes e.g. of the zero-time peak in the vertical RF (Figure S4-4a,b). Choosing a spike position at the front of the deconvolution-window leads to a very noisy deconvolution result as the P-wave train of the

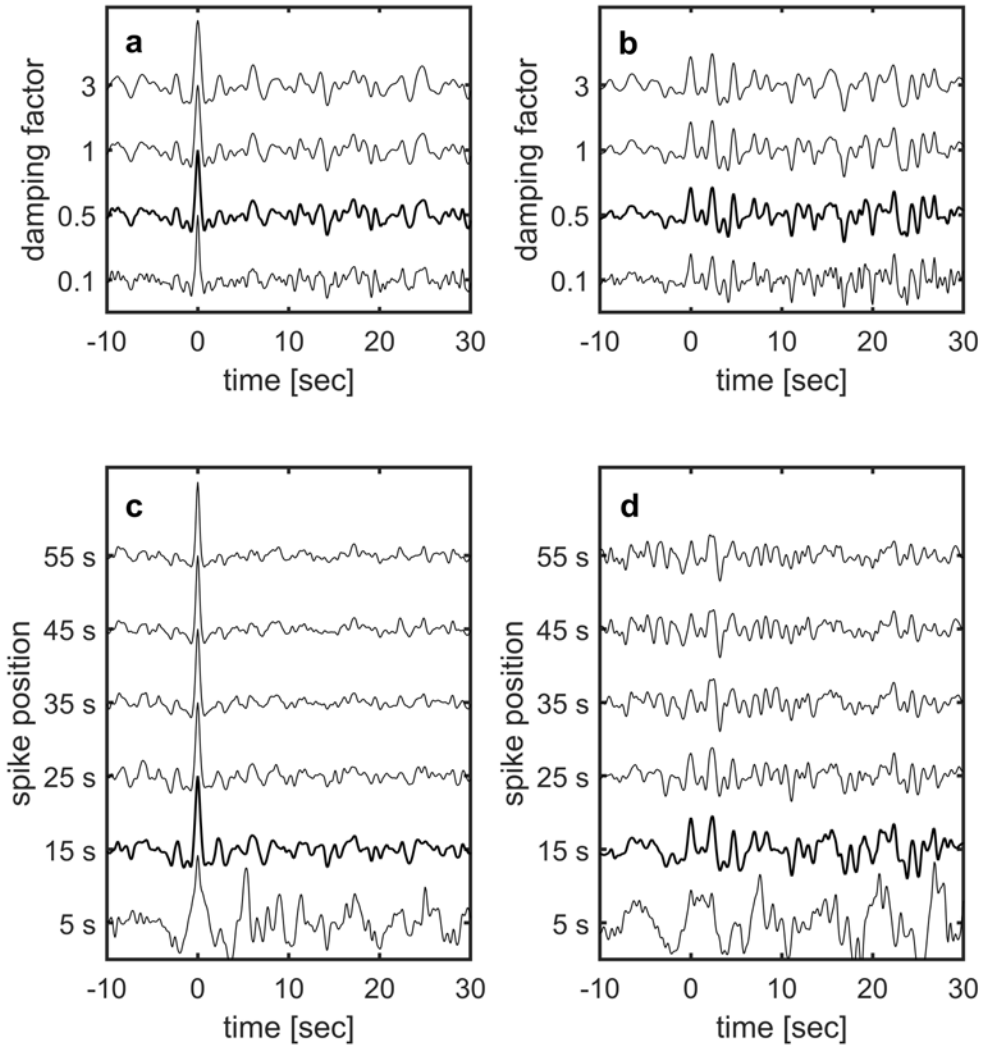

Figure S4-4. Comparison of radial RFs for S0173a for different parameter settings for the Wiener filter deconvolution. One example of a deglitched waveform is shown. **a** Vertical RFs for different damping factors. **b** Radial RFs for different damping factors. **c** Vertical RFs for a deconvolution window length of 100 s with variable spike positions. **d** Radial RFs for a deconvolution window length of 100 s with variable spike positions. The choice of parameters is discussed in Supplementary Method D and the results for the chosen parameters are plotted as thick lines.

event is not minimum phase. A position at 35 s or later results in a smoother vertical RF, but also increases the noise before the P-wave onset on the radial RF, as well as broadens and decreases the amplitude of the P-wave onset and of later phases on the radial RF (Figure S4-4c,d). For a deconvolution window length of 100 s, the centroid of the signal, where the spike is positioned in

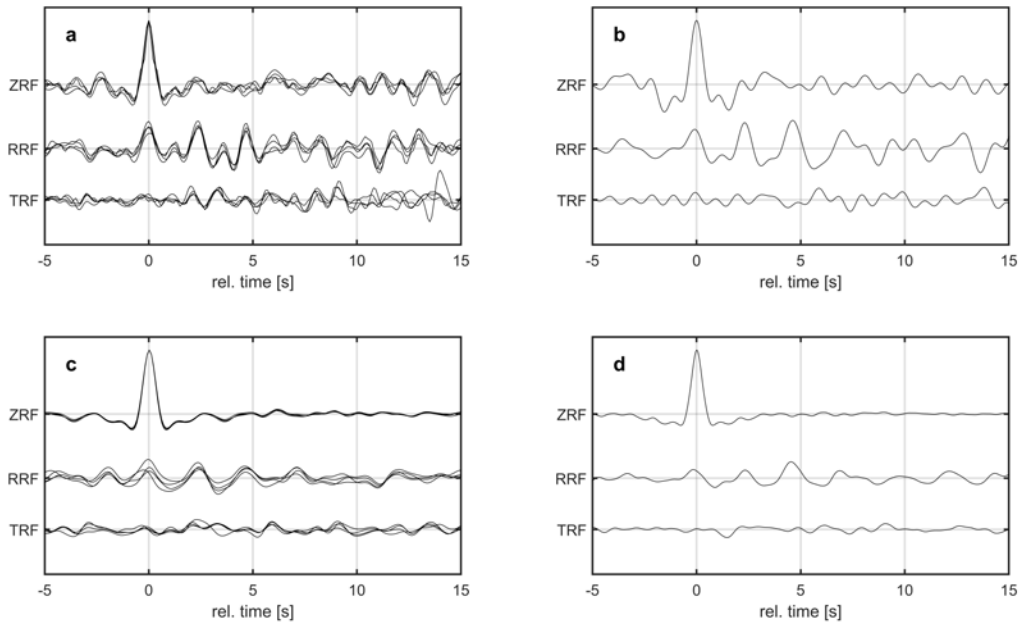

Figure S4-5. Vertical (ZRF), radial (RRF), and transverse (TRF) components of the RFs for S0173a (**a,c**) and S0235b (**b,d**). RF traces were obtained using Wiener filter deconvolution (**a,b**) and iterative time-domain deconvolution (**c,d**). Plots **a** and **c** combine results from various deglitching methods. For both events and RF processing methods, amplitudes on the transverse component are significantly smaller than those on the radial component within the time range considered here.

automatic mode, is at 47 s. Parameters used for S0235b are similar, with a deconvolution window length of 33 s (spike position at 13.5 s), and a damping factor of 0.1. Resulting vertical, radial and transverse RFs are shown in Figure S4-5a, b.

Supplementary Method E: To compute P-to-s RFs, the waveforms are first filtered using a 2nd order Butterworth band-pass filter with corner periods of 0.5 and 20 s, respectively, and then rotated to the Z-R-T system on the basis of the MQS-estimated event location. To isolate source- and response-wavelets, the waveforms are trimmed using a window of [-50, +150 s] relative to the estimated P-wave arrival and tapered with a 5%-Hanning-window for both source- and response traces. Applying iterative time-domain deconvolution[5] to the waveforms eliminates the source-signature in the response trace and results in the RF, which is subsequently band-pass filtered with corner periods of 1 and 10 s, respectively. Resulting RF waveforms for S0173a and S0235b

are shown in Figure S4-5c and S4-5d, respectively. Different passbands and signal windows were tested, but resulted in similar RFs.

Comparison of Results: RFs for the different deglitching and processing methods are compared in Figure S4-2 and Figure 6. The results for different deglitching methods, but using the same processing method, for S0173 show little variability within the first 5 s (Figure S4-2 b) and are in general more similar than the results for different processing methods, but using the same deglitched data set (Figure S4-2 a). While the timing of the main phases in the receiver functions is in close agreement for both cases, the main variability when comparing different processing methods lies in the amplitudes of these phases. This is expected as the amplitudes are more dependent on the specifics of the processing, e.g. filtering, and the details of the deconvolution method and inherent assumptions on the RF frequency content, than the timing of phases. The phase timing is in general considered the more stable information contained in RFs, as amplitudes will also vary depending for example on azimuth (e.g. for dipping layers or anisotropy) and incidence angle. Therefore, we also take into account a larger uncertainty in amplitude when inverting the RF waveform. When comparing results for S0173a and S0235b, there are some differences in azimuth and incidence angle between the two events, which will influence the amplitudes of phases in the single event waveforms. On Earth, this variability between events is usually little remarked-upon, since it is common to stack many events (either in the time domain or in the physical domain by projecting the data and migrating to depth) and only interpret the cumulative result. Due to the limited amount of Martian events that can be used for RF processing so far, this is not possible here.

S4-3: Forward Seismic Modeling

Forward modeling of different low-velocity layers is performed to assess the extent to which different structures are compatible with the RFs generated for S0173a and S0235b.

Results from testing the effect of variable regolith layer thickness are shown in Figure S4-6. The regolith layer has a P-wave velocity of 120 m/s near the surface, to be consistent with the value derived in Supplementary Material 2-2, and increasing with depth[12], and a Vp/Vs ratio of

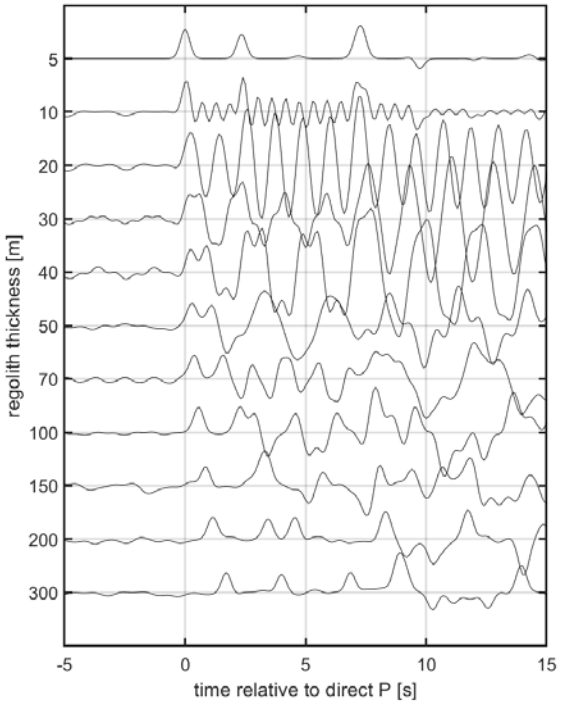

Figure S4-6. Modeled influence of variable regolith layer thickness on radial RFs.

1.669 as derived from lab measurements on analog material[13]. The thickness of the regolith layer is increased stepwise from 5 to 300 m. The layer beneath the regolith has an S-wave velocity of 2 km/s, as derived from the RF inversion (Section S4-4) , and extends to 10 km depth, followed by a faster layer with a Moho at 40 km depth. Modeling is performed using a simple reflectivity code that calculates the impulse response of a stack of layers[14]. A ray parameter of 7.05 s/deg is used in the modeling, and the frequency content is chosen so as to match that of the observed RFs.

No effect of the regolith layer is observed for a 5 m thick regolith, and the timing of the first peak at 2.35 s matches well with the available data. Reverberations in the regolith layer start to show up already for a regolith thickness of 10 m and become very pronounced for 20 m thickness. For larger thicknesses, a 'ringing' effect is still perceived, but from 70-100 m thickness, the regolith layer produces a well-defined conversion that distinctly offsets the direct P-wave peak on the radial RF from zero time. For thicknesses of 200 m and more, the original conversions are again clearly identifiable, but are all shifted to later times corresponding to the travel time within the regolith layer and followed by a distinct regolith multiple. None of the regolith effects modeled here are

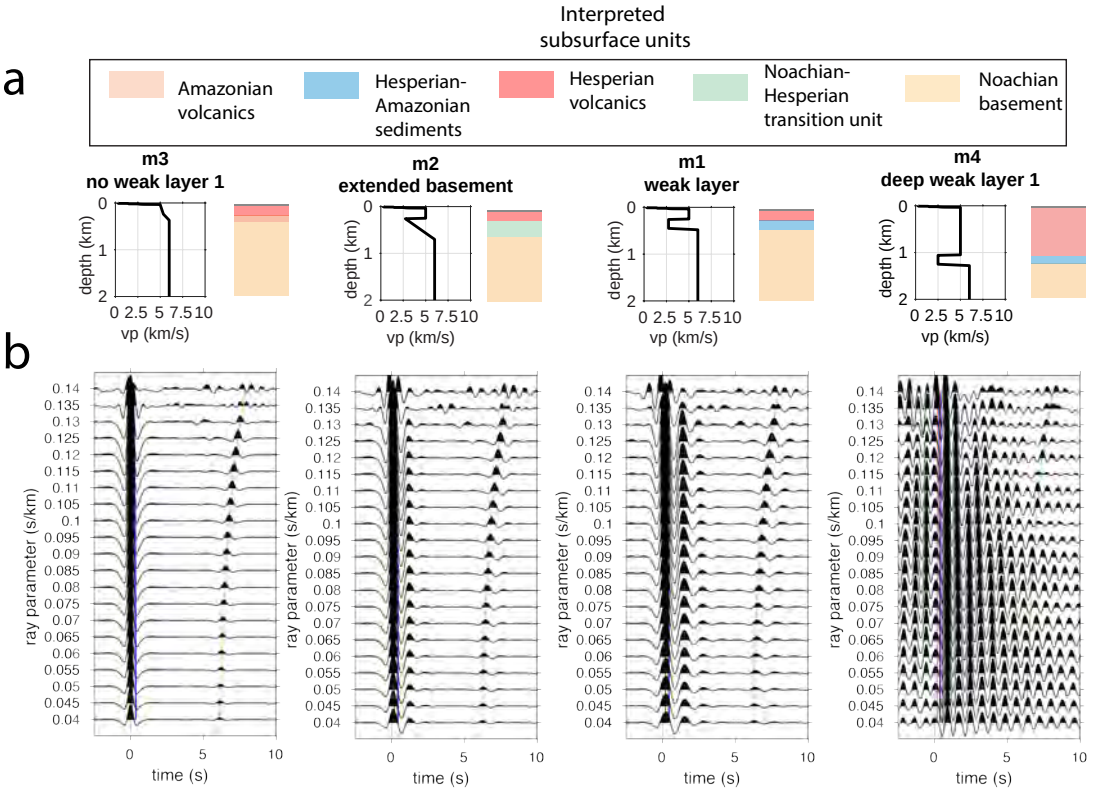

Figure S4-7. Effects of a priori geological models on RF waveforms. **a** Four selected a priori geological models[16]; legend indicates subsurface units. **b** Predicted radial RF waveforms are shown for models m3, m2, m1 and m4. Waveforms are calculated and plotted as a function of slowness of the input plane P-wave. Green curves indicate predicted travel times of a direct Ps conversion from a mid-crustal interface at $\sim$ 47 km depth.

observed in the data, so within the velocity range considered, and for a simple 1D-model, a regolith thickness of 20 m and more can be excluded, consistent with the results from compliance inversion and predictions from geology for the landing site[15].

Results from testing the effect of different a priori geological models on radial RF waveforms are shown in Figure S4-7. The four tested models are presented in detail in Pan et al.[16]. These models are based on observations of subsurface materials from orbit, elastic properties of Martian regolith and Earth analogs, and the density and porosity of Martian meteorites[12;13;17;16]. The effect of temperature and pressure with depth has been evaluated and shown to be insignificant[16]. Radial RF waveforms are predicted for various slownesses of incoming plane P-waves. None of the predicted RF waveforms provides a good fit to the data. Models with a shallow low-velocity zone

only affect the first 3 s of the radial RFs, whereas the model with a 200-m thick low-velocity zone at 1 km depth generates a strongly reverberating wavefield.

S4-4: Seismic inversion

The receiver functions are also used to obtain the apparent S-wave velocity as a function of period, and inverted to obtain an average velocity for an upper crustal layer as described by a layer-over-half-space model.

For the inversion, apparent S-wave velocities are used as an additional constraint jointly with the RF waveforms. Apparent S-wave velocities as a function of period are derived from the apparent P-wave incidence angles with respect to the vertical measured from the vertical and radial RF waveforms filtered with second-order zero-phase Butterworth low-pass filters with logarithmically-distributed corner periods[18;19]. In order to calculate apparent S-wave velocities from the apparent incidence angles, an estimate of the ray parameter is needed. For S0173a, the probabilistic distribution of ray parameter values as provided by MQS is given in Figure S4-8a. A grid search is done over possible combinations of event depth, epicentral distance and velocity model, calculating a ray parameter for each possible solution. The histogram is weighted by the travel-time misfit of the solutions. A detailed description can be found in Böse et al.[20]. The resulting four probability distributions for the four different deglitching algorithms and the Wiener filter deconvolution (supplementary method D) are shown in Figure S4-8b. Periods covered for each curve are those where the signal-to-noise ratio of both vertical- and radial-component RFs is larger than 5[17].

The curves based on the deglitching by MPS and IPGP are broadly similar, whereas the other two curves look rather atypical with values decreasing below zero. For comparison, the apparent velocities resulting from apparent P-wave incidence angles against the vertical measured from polarization analysis[21] of the waveform filtered between 2 Hz and 10 s for different deglitching methods is also given. The measured incidence angles vary between 29° and 32° for the different methods. The resulting apparent velocity values, based on the most probable ray parameter of 7.05 s/deg, are larger than the apparent S-wave velocity curves at periods shorter than 5 s. This could

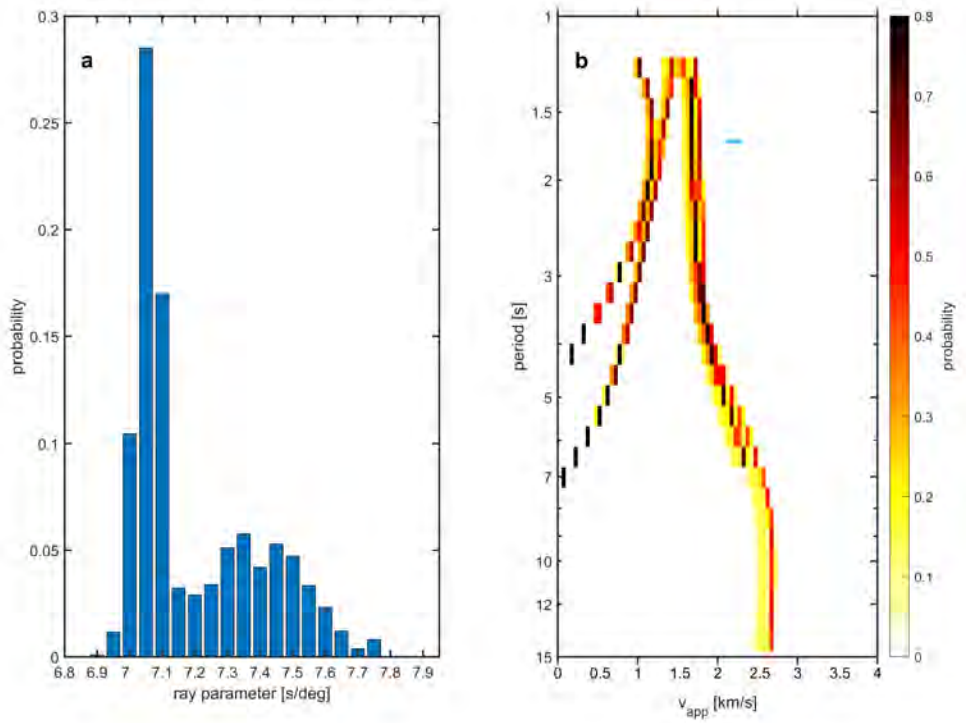

Figure S4-8. Apparent S-wave velocities for S0173a. **a** Probability distribution of the ray parameter of the incident P-wave. **b** Apparent S-wave velocity curves for various deglitching methods for S0173a, derived from apparent incidence angles measured on filtered RFs[22]. Color shading indicates probability based on the ray parameter used, normalized individually for each deglitching method. The light blue bar indicates the most probable range of apparent velocities based on incidence angles derived from polarization analysis of the P-wave onset for the different deglitched data sets and the most likely ray parameter.

be because they were measured on broad-band waveforms and might average over the velocities within the upper two layers.

The apparent velocity curve for the MPS deglitching (Figure S4-8b) was jointly inverted with the first 6 s of the corresponding radial RF waveform for S0173a, using a modified Neighbourhood Algorithm[23;24], a direct search method that provides an ensemble of models that can explain the given data. As inversions were only aiming for the properties of the first layer associated with the converted phase observed at 2.2-2.4 s, the models were parameterized as a layer over a half-space, using both a constant layer velocity and a linear velocity increase within the layer. In addition to the layer thickness and the S-wave velocity within the layer and the half-space, the Vp/Vs ratios of both layer and half-space were also inverted for. The misfits of both data sets were weighted

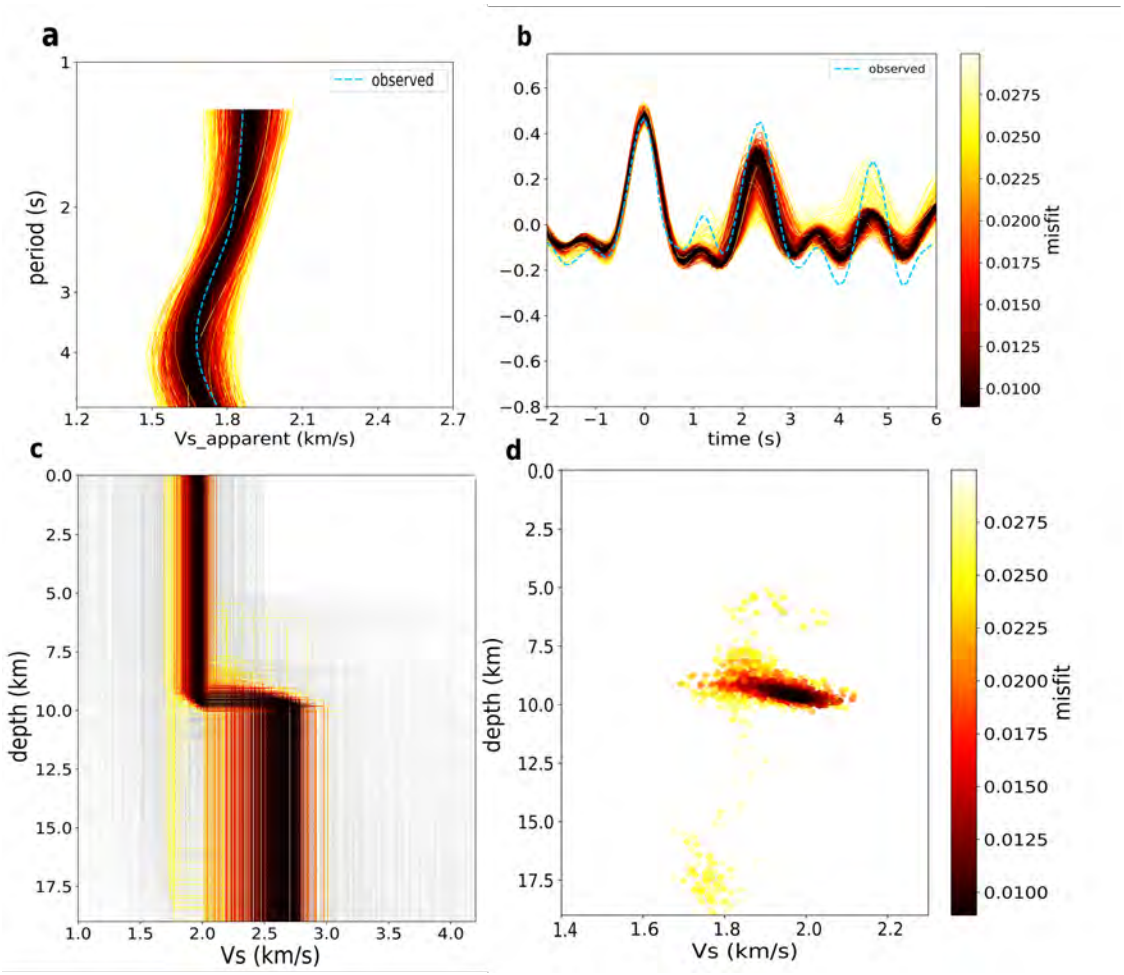

Figure S4-9. Results of the inversion of apparent S-wave velocities and the first 6 s of the radial RF of S0173a (MPS deglitching) for a layer-over-a-half-space model. **a** Fit to apparent S-wave velocity curve **b** Fit to RF waveform **c** Resulting velocity models. Gray lines indicate models also investigated which have a larger misfit than the colored range. **d** Trade-off plot between depth and S-wave velocity of the first layer. Minimum, maximum and best fit S and P velocities for the two layers are provided in **Supplementary Table 3**.

equally in the inversion, using an L1 misfit norm. A ray parameter of 7.0 s/deg was used. Figure S4-9 shows results for a constant velocity in the upper layer, but results for a gradient layer are broadly similar: the best-fitting models do not require a velocity increase in the topmost layer, and values for the S-wave velocity at the top of the layer and the layer thickness are similar to the constant case (1.7 to 2.1 km/s and 8 to 11 km, respectively), whereas those for the S-wave velocity at the bottom lie between 1.9 and 2.4 km/s. When deriving these ranges from the inversion results (e.g. Figure S4-9), we consider a comparatively large uncertainty in the amplitude of the conversion

at 2.2 to 2.4 s, as warranted by the differences in the various RF estimates (Figure 6). This also means that Vp/Vs ratios in both layers are not constrained by the data within the investigated range (1.6 to 2.1), as this would require the use of multiple reflections, well-constrained amplitudes, and apparent S-wave velocities that extend to longer periods. The main constraint on the velocity in the topmost layer (and hence its thickness, as the phase arrival in RFs only yields a travel time which equals the ratio of layer thickness to velocity) is provided by the apparent S-wave velocity curve and the amplitude of the direct P arrival at 0 s on the radial RF. The full uncertainty of these data (Figure S4-8, Figure 6) further increases the possible model range. However, for the reasons mentioned above, the two right-most apparent velocity curves in Figure S4-8b and the corresponding RF waveforms were considered the most reliable.

S4-5: Seismic Velocities and Expected Rock Types in the Martian Crust

We investigate the range of rock types and related seismic velocities that are expected in the Martian crust, and more specifically around the InSight landing site. Figure S4-10 presents a variety of relevant materials consistent with orbital and rover observations of the Martian surface together with their seismic velocities based on terrestrial observations. The Martian crust seems to host a wide range of rocks (sedimentary, volcanic, unconsolidated and impact related) associated with compressional seismic velocities from 0.1 to 7 km/s. Crustal composition and structure (e.g., sediments and/or volcanic layering, mineral fabric, faults, and distribution of fractures) are expected to vary with depth and will therefor impact the P- and S-wave velocities directly (see Table S4-1 and Smrekar et al.[25] for details).

Around the InSight landing site, independent lines of evidence point to the presence of about 200-300 m of Hesperian to Early Amazonian basaltic volcanic flows that are underlain by weaker sedimentary rocks rich in phyllosilicates. Arguments include local geological mapping[26], the presence of rocky ejecta craters $\sim$0.5-2 km in diameter[15], mafic mineral spectra of shallow exposed outcrops in fresh crater walls in CRISM data[16], the presence of wrinkle ridges produced by asymmetric folding in strong, but weakly bonded layered material[15;26], and, at larger scale, Gamma-Ray Spectrometer chemical analysis[27]. The thickness of the sedimentary rocks is unknown, but in

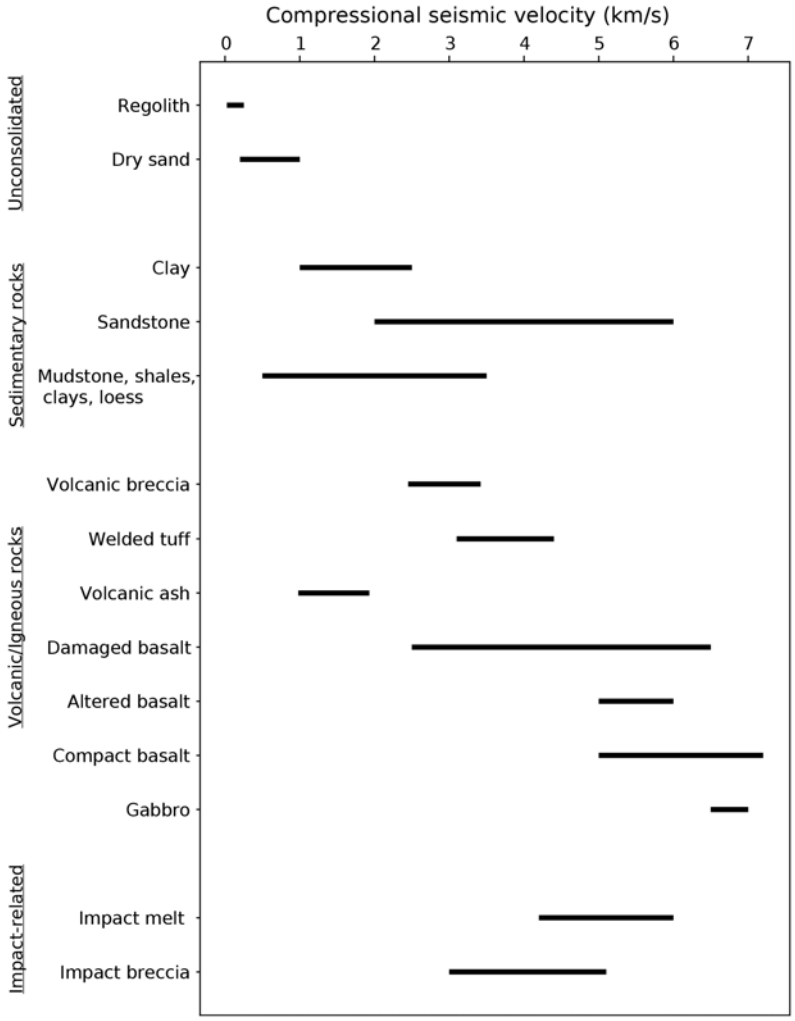

Figure S4-10. A list of Mars-relevant materials consistent with orbital and rover observations of the Martian surface and their seismic velocities based on terrestrial observations, including regolith[12], dry sand[28], clay[28], sandstone[28], mudstone/shale[25], volcanic breccia[29], welded tuff[30;31], volcanic ash[32], damaged basalt[25], altered basalt[25], compact basalt[25], gabbro[28],impact melt[33;34] and impact breccia[33;34].

some cases their presence in crater central peaks indicates depths of 4-5 km[16]. The relatively low S-wave velocities found in our study from receiver functions analysis (e.g. 1.7 to 2.1 km/s in the upper crustal layers) imply that the upper volcanic rocks (likely basalts) might be highly altered and/or damaged, causing a reduction of their seismic velocities by up to 50%[25].

Seismic observations suggest a discontinuity between 8 and 11 km depth where S-wave velocities increase to values between 2 and 3 km/s. These results are in good agreement with expected seismic velocities and lithologies (altered basalts) proposed by ref.[25] (Table S4-1).

The seismic observations indicate that the regolith at the landing site is significantly thinner

Range of depth (km)[25]	Expected lithologies	Range of density[25]	Range of V_P (km/s)[25,a]	Range of V_S (km/s)[25,a]	Estimated V_S (km/s) (this study)	Expected lithologies/structures (this study)
0 to 5-7	Basaltic lava flows (0 to 0.2-0.3 km deep) and sedimentary rocks (0.2-0.3 to 5-7 km deep)	1.5 to 3.1	1.1 to 6	0.2 to 3.4	1.7 to 2.1	Top layers around the landing site . mainly composed of altered/fractured volcanic rocks
5-7 to 15-20	Altered basaltic rocks	2.4 to 2.8	4.5 to 6	2.5 to 3.3	2 to 3	Altered, iron-rich basaltic rocks
15-20 to 100	Compacted basalts	2.7 to 3.1	5 to 7.2	2.8 to 4	?	-

[a] Note that seismic velocities can be affected by anisotropy, layering, martian lithostatic pressure, damage zones around faults and fractures, etc. inducing possible increase/decrease of Vp and Vs (+15/-50% between 0 and 5-7 km ; +15%/-15% between 5-7 to 15-20 km)[25]

Table S4-1. Plausible range of lateral crustal variations in density, P -wave and S-wave velocities within Martian crust region[25] and estimated S-wave velocity and lithology at the InSight landing site.

than on the Moon, where seismic models contain a 1 km thick surficial layer with S-wave velocities of a few 100 m/s[35;36;37]. The derived range of S-wave velocities in the upper-most crust of Mars is however comparable to more recent models for the Moon at 1-12 km depth[36;37].

References

[1] Kennett, B. L. N. The removal of free surface interactions from three-component seismograms. *G*eophys. J. Int., **104(1)**, 53-163 (1991)

[2] Abt, D. L., Fischer, K. M., French, S. W., Ford, H. A., Yuan, H., and Romanowicz, B. North American lithospheric discontinuity structure imaged by Ps and Sp receiver functions. *J. Geophys. Res.*, **115(B9)** (2010)

[3] Kolb, J. M. and Lekić, V. Receiver function deconvolution using transdimensional hierarchical Bayesian inference. *Geophys. J. Int.* **197**, 1719-1735 (2014) doi:10.1093/gji/ggu079

[4] Clayton, R. W. and Wiggins, R. A. Source shape estimation and deconvolution of teleseismic bodywaves. *Geophys. J. Int.* **47**, 151-177 (1976)

[5] Ligorria, J. P. and Ammon, C. J. Iterative deconvolution and receiver-function estimation. *Bull. Seism. Soc. Am.* **89**, 1395-1400 (1999)

[6] Phạm, T. S. and Tkalčić, H. On the feasibility and use of teleseismic P wave coda autocorrelation for mapping shallow seismic discontinuities. *J. Geophys. Res.* **122**, 3776-3791 (2017)

[7] Tauzin, B., Phạm, T. S. and Tkalčić, H. Receiver functions from seismic interferometry: a practical guide. *Geophys. J. Int.* **217**, 1-24 (2019)

[8] Helffrich, G. Extended-time multitaper frequency domain cross-correlation receiver function estimation. *Bull. Seism. Soc. Am.* **96**, 344-347 (2006)

[9] Shibutani, T., Ueno, T., Hirahara, K. Improvement in the extended-time multitaper receiver function estimation technique. *Bull. Seis. Soc. Am.* **98**, 812-816 (2008)

[10] Kind, R., Kosarev, G. L. and Petersen, N. V. Receiver functions at the stations of the German Regional Seismic Network (GRSN). *Geophys. J. Int* **121**, 191-202 (1995)

[11] Hannemann, K., Krüger, F., Dahm, T. and Lange, D. Structure of the oceanic lithosphere and upper mantle north of the Gloria Fault in the eastern mid-Atlantic by receiver function analysis. *J. Geophys. Res.* **122**, 7927-7950 (2017)

[12] Morgan, P., Grott, M., Knapmeyer-Endrun, B., Golombek M., Delage P., et al.. A Pre-Landing Assessment of Regolith Properties at the InSight Landing Site. *Space Sci. Rev.*, **214(6)**, 104 (2018)

[13] Delage, P., Karakostas, F., Dhemaied, A., Belmokhtar, M., Lognonné, P., Golombek, M., De Laure, E., Hurst, K., Dupla, J.-C., Cui, Y. J. and Banerdt, B. An investigation of the mechanical properties of some Martian regolith simulants with respect to the surface properties at the InSight mission landing site. *Space Sci. Rev.* **211**, 191-213 (2017)

[14] Shibutani, T., Sambridge, M. and Kennett, B. Genetic algorithm inversion for receiver functions with application to crust and uppermost mantle structure beneath eastern Australia.

Geophys. Res. Lett. **23**, 1829-1832 (1996)

[15] Golombek, M., Kipp, D., Warner, N., Daubar, I. J., Fergason, R., Kirk, R., Beyer, R., Huertas, A., Piquuex, S., Putzig, N. et al. Selection of the InSight landing site. *Space Sci. Rev.* **211**, 5-95 (2017)

[16] Pan L., Quantin-Nataf, C., Tauzin, B., Michaut, C., Golombek, M., Lognonné, P., Grindrod, P., Langlais, B., Gudkova, T., Stepanova, I., Rodriguez, S. and Lucas, A. Crust stratigraphy and heterogeneities of the first kilometers at the dichotomy boundary in western Elysium Planitia and implications for InSight lander *Icarus* **338**, 113511 (2020) doi:10.1016/j.icarus.2019.113511

[17] Knapmeyer-Endrun, B., Murdoch, N, Kenda, B., Golombek, M. P., Knapmeyer, M., Witte, L., Verdier, N., Kedar, S., Lognonné, P. and Banerdt, W. B. Influence of body waves, instrumentation resonances, and prior assumptions on Rayleigh wave ellipticity inversion for shallow structure at the InSight landing site. *Space Sci. Rev.* **214**, 94 (2018)

[18] Svenningsen, L and Jacobsen, B. H. Absolute S-velocity information from receiver functions. *Geophys. J. Int.* **170**, 1089-1094 (2007)

[19] Hannemann, K., Krüger, F., Dahm, T. and Lange, D. Oceanic lithospheric S wave velocities from the analysis of P wave polarization at the ocean floor. *Geophys. J. Int.* **207**, 1796-1817 (2016)

[20] Böse, M., Clinton, J. F., Ceylan, S., Euchner, F., van Driel, M. Khan, A., Giardini, D., Lognonné, P. and Banerdt, W. B. A probabilistic framework for single-station location of seismicity on Earth and Mars. *Phys. Earth and Planet. Int.* **262**, 48-65 (2017) doi:10.1016/j.pepi.2016.11.003

[21] Jurkevics, A. Polarization analysis of three-component array data. *Bull. Seism. Soc. Am.* **78**, 1725-1743 (1988)

[22] Knapmeyer-Endrun, B., Ceylan, S. and van Driel, M. Crustal S-wave velocity from apparent incidence angles: a case study in preparation of InSight. *Space Sci. Rev.* **214**, 83 (2018)

[23] Sambridge, M. Geophysical inversion with a neighbourhood algorithm - I. Searching a parameter space. *Geophys. J. Int.* **138**, 479-494 (1999)

[24] Wathelet, M. An improved neighborhood algorithm: Parameter conditions and dynamic scaling. *Geophys. Res. Let.* **35** (2008)

[25] Smrekar, S. E., Lognonné, P., Spohn, T., Banerdt, W. B., Breuer, D., Christensen, U., et al. Pre-mission InSights on the Interior of Mars. *Space Sci. Rev.*, **215(1)**, 3 (2019)

[26] Golombek, M., M. Grott, G. Kargl, J. Andrade, J. Marshall, et al. Geology and physical properties investigations by the InSight Lander. *Space Sci. Rev.* **214**, 84 (2018). doi: 10.1007/s11214-018-0512-7.

[27] Baratoux, D., Toplis, M., Monnereau, M., and Gasnault, O. Thermal history of Mars inferred from orbital geochemistry of volcanic provinces. *Nature*, **472**, 338-341 (2011)

[28] Kearey, P., and Brooks, M. *An introduction to geophysical prospecting*. Blackwell, Boston (1991)

[29] Barrett, P. J., and Froggatt, P. C. Densities, porosities, and seismic velocities of some rocks from Victoria Land, Antarctica. *New Zealand J. of Geol. Geophys.*, **21(2)**, 175-187 (1978)

[30] Hill, D. P., Kissling E., Luetgert, J. H., Kradolfer, and U. Constraints on the upper crustal structure of the Long Valley-Mono Craters Volcanic Complex, Eastern California, from seismic refraction measurements. *J. Geophys. Res.*, **90(B13)**, 11135-11150 (1985)

[31] Vinciguerra, S., Trovato, C., Meredith, P. G., Benson, P. M., Troise, C., and De Natale, G. Understanding the seismic velocity structure of Campi Flegrei caldera (Italy): from the laboratory to the field scale. *Pure Appl. Geophys.*, **163(10)**, 2205-2221 (2006)

[32] Kienle, J. Depth of the ash flow deposit in the Valley of Ten Thousand Smokes, Katmai National Park, Alaska. *Geophys. Res. Lett.*, **18(8)**, 1533-1536 (1991)

[33] Kukkonen, I. T., Kivekäs, L., and Paananen, M. (1992). Physical properties of kärnäite (impact melt), suevite and impact breccia in the Lappajärvi meteorite crater, Finland. *Tectonophysics*, **216(1-2)**, 111-122 (1992)

[34] Brittan, J., Morgan, J., Warner, M., and Marin, L. Near-surface seismic expression of the Chicxulub impact crater. *Special Papers-Geological Society Of America*, 269-280 (1999)

[35] Nakamura, Y. Seismic velocity structure of the lunar mantle. *J. Geophys. Res.*, **88**, 677 686 (1983) doi:10.1029/JB088iB01p00677

[36] Gagnepain-Beyneix, J., Lognonn, P., Chenet, H., Lombardi, D. and Spohn, T. A seismic model of the lunar mantle and constraints on temperature and mineralogy, *Phys. Earth Planet. Int.* **159**, 140-166 (2006) doi:10.1016/j.pepi.2006.05.009.

[37] Garcia, R. F., Gagnepain-Beyneix, J., Chevrot, S. and Lognonné, P. Very preliminary reference Moon model. *Phys. Earth Planet.* Int. **188**, 96-113 (2011) doi:10.1016/j.pepi.2011.06.015.

Supplementary Material 5

J.-R. Scholz, P. Davis, R. Widmer-Schnidrig, F. Nimmo, P. Lognonné, K. Hurst, L. Pou, B. Pinot, R. F. Garcia, S. Barkaoui, E. Stutzmann, T. Pike, S. Kedar, S. Stähler, M. van Driel, S. Ceylan, A. Horleston, J. Clinton, A. Stott, J. McClean, C. Charalambous

Glitches in SEIS' time series data

In the following we define a glitch as a particular type of transient instrumental self-noise. Its duration is controlled by the transfer function and since both SEIS' very broad-band (VBB) and short-period (SP) sensors are second order high pass filters for ground velocity, the glitch shape and duration is related to the corner period and damping: 16 seconds and 76% damping for the VBB while the SP is overdamped with 110% damping and a 6 db decay in about 37.5 seconds. In the raw data, high amplitude glitches appear with subsequent decay. The glitch onset is often immediately preceded or concurrent with high frequency spikes. Glitches occur at all times of the Martian day (sol) and include very broadband frequency content. They are recorded on both the VBB and SP sensors, and may or may not be present on all six of these seismic components. Glitches influence many of the standard seismological analyses and understanding their character and providing a corrected time series therefore is important. A glitch example for one of the VBB components is shown in Fig. S5-1a.

The glitches seen on VBB and SP can be consistently modelled as a step in the measured ground acceleration (Fig. S5-2b, blue line). Similar glitches are common in terrestrial broad-band seismic data where their absence is one criterion for the quality of the sensor, its installation, and its installation site. A number of physical processes can lead to glitches but on Mars our analyses suggest the primary glitch culprits are thermal stresses and, to a lesser extent, compliant soil. This is because both VBB and SP are exposed to daily temperature cycles at least 5 orders of magnitude larger than for a well shielded, terrestrial vault seismometer. The glitches we observe are highly linearly polarized (Fig. S5-2) and cluster in preferred directions (Fig. S5-3). As probable glitch causes we consider:

(i) Glitches occurring on all VBB sensors but not on the SPs, and that are large enough to be above the SP noise, must be attributed to the suspension of the VBBs inside the sphere (e.g., glitch 2 in Tab. S5-1).

(ii) Glitches that occur on the VBB and SP horizontals but not on the verticals (when components are rotated), must be attributed to a nano-settling of the foot of SEIS' levelling system (LVL) into the surface. The acceleration of these glitches points away from the direction of the respective LVL foot (e.g., glitch 20 in Tab. S5-1 and Fig. S5-2).

(iii) Glitches on all components with polarization pointing in the direction of the tether (cable connecting SEIS and the InSight lander) must be attributed to the tether - except that the load shunt assembly (LSA) should attenuate the effect of an expanding and contracting tether.

(iv) Single component glitches on the VBB must be attributed to stress relaxation in the leaf spring, the suspension, or a relaxation in the thermal compensation device (TCD). For the LCD, there exists no experience from Earth regarding the likelihood of glitch generation as thermal test chambers are too noisy in terms of their seismic background noise.

(v) Besides the mechanical processes causing glitches, there is the possibility of an electrically generated glitch. On Earth, humidity entering connectors can lead to glitch-like signals. On Mars, humidity is not a concern but electrostatic discharge may, however, be. Glitches with electronic causes need not mimic a step in acceleration. We have no indication of such glitches.

Assuming that the glitches are caused by pure steps in acceleration, they can be used to determine the parameters of the instrument response. In doing so, we have found that while the estimated corner period is consistent with our best VBB model, the damping parameter, h, is lower than when determined via voice coil calibration. This indicates the glitches are not caused by a pure step in acceleration but likely by a ramp - albeit a very short one. Alternatively, a low signal-to-noise ratio could also lead to a lower than nominal damping (this is still a work in progress). On sols 194 and 195 (2019-06-13T13:09:00 to 2019-06-15T14:30:00), we observed 30 glitches on VBB and SP with at least one out of the six components exceeding an amplitude of 1e-7 m/s (Tab. S5-1). For this period of time, we count 24 glitches on VBB of which 62% are also seen on SP,

and 22 glitches on SP of which 73% are also seen on VBB. Usually, glitches on VBB are visible on all three components but in rare cases they occur only on one component. These glitches often have an amplitude lower than 1e-7 m/s, which is why they do not show in Table S5-1. We found some of the largest VBB glitches occur every sol within the morning hours (glitch 10 and 23 in Tab. S5-1). These glitches coincide with a critical, outside Martian temperature of roughly -97° C. As these glitches are not (well) seen on SP, they could be attributed to the suspension of the VBB sensors inside the sphere in agreement with glitch model (1).

Glitch removal techniques

We developed three different techniques to remove the glitches from SEIS' time series data.

Instrument Transfer Function: To remove the glitches from the RAW data, we first model the glitches in shape and amplitude and subtract those from the original glitches. Our modeling is based on the assumption that the glitch shape is well represented by the instrument's finite response to a source function. Indeed our analyses show, in most cases a δ-function as source function models the glitches closely, in some cases, however, a source function of finite width is the better choice. We use Lagrangian multipliers to avoid artificial data offsets that may occur after subtracting the modeled from the original glitches. This method was developed by three different sub-groups whose overall approach was equal but differed in the definition of source function and subtraction strategy of the modeled from the observed glitches. These slightly different approaches are labeled "IPGP", "UCLA" and "ISAE" in the Supplementary Material 4.

Deep Scattering Network: This deep learning tool helps to automatically cluster all different signal families observed in typical SEIS data (glitches, dust devils, donks, ...). It extracts the event waveforms related to each cluster, thus forming an "event matrix". Its columns correspond to the cluster's event numbers and its rows to the event waveform duration. Applying singular vector decomposition, the fundamental singular value will correspond to the glitch. To clean the signal from the glitches, we clean the signal from the corresponding singular value and reconstruct the new, deglitched waveforms. An example of the detected glitches is shown in Fig. S5-4.

Discrete Wavelet Transform: Using the Haar wavelet that is suited for sudden amplitude changes

in the time series data (i.e., glitches), this method decomposes the RAW signal into different frequency bands whose range depend on the data length. The decomposed signal in each of these frequency bands is then tested against amplitude spikes, using a threshold condition based on the moving median of the absolute local extrema. If the threshold is exceeded, the corresponding value is corrected taking into account its neighboring absolute local extrema that do not exceed this threshold. The reconstruction of the corrected decomposition coefficients returns the deglitched data. An example of such glitch removal is presented in Fig. S5-1. Fig. S5-5 shows three spectrograms comparing the original data, the wavelet-deglitched data, and their difference for a period of 28 hours. This method is labeled "MPS" in the Supplementary Material 4.

All methods have been proven to detect and remove glitches, yet no method has been demonstrated to outperform all others. The optimization of each method and their final application to the recorded data is therefore still a work in progress.

#	Glitch LMST	VBB			SP		
		U	V	W	Z	2	3
1	Sol 194, 00:38:57	x	x	x	-	x	x
2	Sol 194, 03:08:45	x	x	x	-	-	-
3	Sol 194, 03:16:25	x	x	x	-	x	x
4	Sol 194, 03:52:16	x	x	x	-	-	-
5	Sol 194, 04:17:37	-	-	-	x	-	-
6	Sol 194, 04:22:36	x	x	x	x	-	-
7	Sol 194, 04:43:40	-	-	-	x	-	-
8	Sol 194, 05:19:42	x	x	x	-	-	x
9	Sol 195, 05:49:03	-	-	-	x	-	-
10	Sol 194, 05:50:54	x	x	x	-	-	-
11	Sol 194, 07:24:31	x	x	x	-	x	-
12	Sol 194, 07:37:44	x	x	x	-	-	x
13	Sol 194, 08:36:19	x	x	x	-	-	x
14	Sol 194, 21:53:49	x	x	x	-	x	x
15	Sol 194, 22:40:14	x	x	x	-	-	-
16	Sol 194, 23:53:20	x	x	x	-	-	-
17	Sol 195, 01:27:02	x	x	x	-	x	x
18	Sol 195, 02:48:46	-	-	-	x	-	-
19	Sol 195, 03:08:51	x	x	x	-	-	-
20	Sol 195, 03:11:51	x	x	x	-	x	x
21	Sol 195, 04:29:35	x	x	x	-	-	-
22	Sol 195, 04:39:16	-	-	-	x	-	-
23	Sol 195, 05:45:06	x	x	x	-	-	-
24	Sol 195, 06:25:07	-	-	-	x	-	-
25	Sol 195, 17:22:09	x	x	x	x	x	x
26	Sol 195, 17:45:09	x	x	x	x	x	x
27	Sol 195, 20:59:44	x	x	x	-	-	x
28	Sol 195, 21:34:02	x	x	x	-	x	x
29	Sol 195, 22:38:17	x	x	x	-	-	-
30	Sol 195, 23:40:12	x	x	x	-	-	-

Table S5-1. Glitches detected by eye for both SEIS' very broad-band (VBB) and short-period (SP) sensors, recorded on sols 194 and 195 (2019-06-13T13:09:00 to 2019-06-15T14:30:00). The recording rate was 20 and 10 samples per second for VBB and SP, respectively. Listed are only glitches with an amplitude larger than 1e-7 m/s for at least one out of the six components. LMST, Local Mean Solar Time in hh:mm:ss. We note that glitches visible on VBB and not SP do not exclude the presence of these glitches on SP, as they may be below the SP noise floor that is higher for longer periods (>1s).

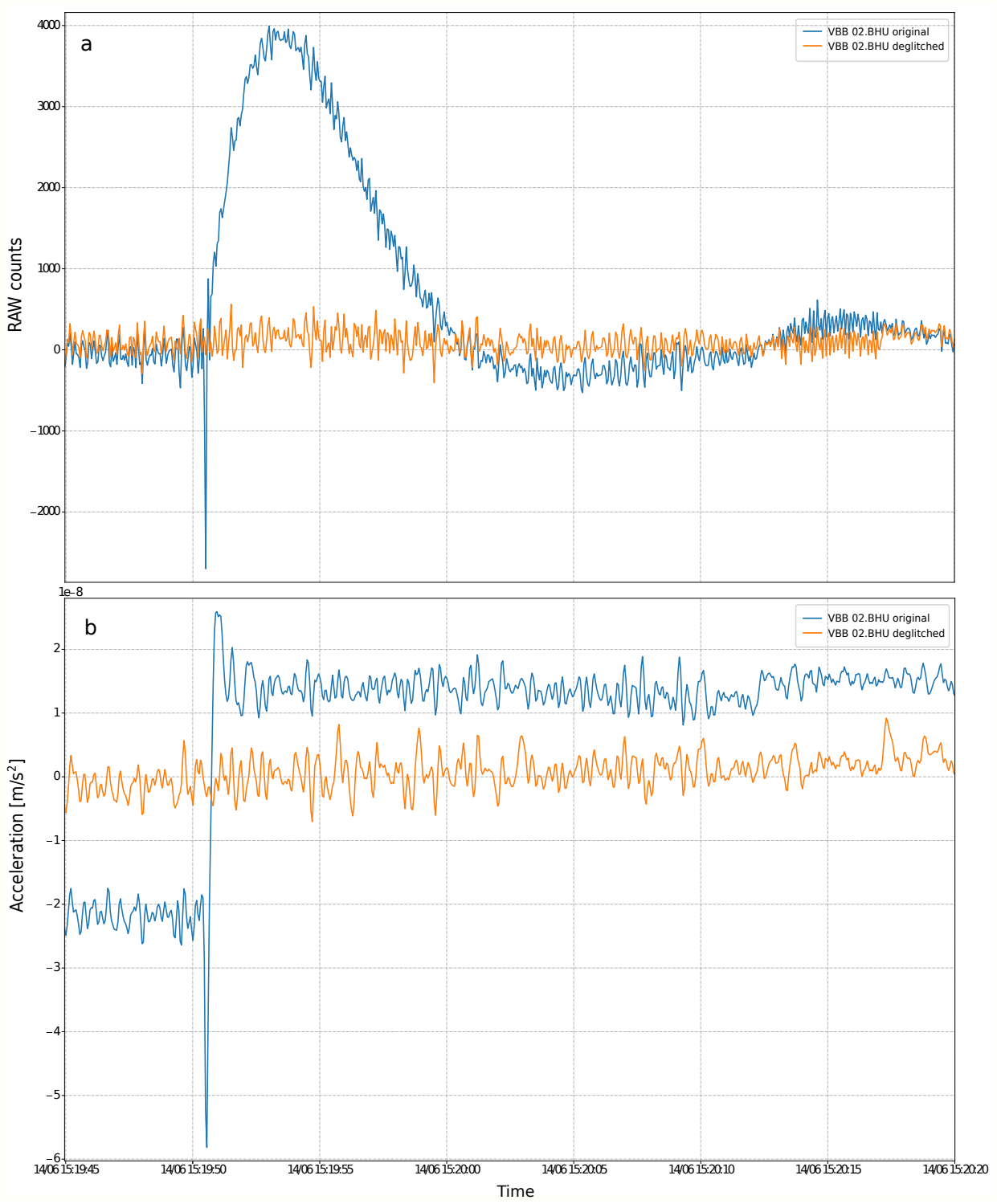

Figure S5-1. Top: 20 samples per second data of VBB U-component in original RAW (blue, glitch 17 in Tab. S5-1) and deglitched RAW (orange). Deglitching was performed using the Discrete Wavelet Transform (see text for details). Bottom: Like top, but with the instrument response removed to show acceleration and subsequent 1 Hz low-pass filtering (second order Butterworth). Note especially the acceleration step in the original data that is absent after deglitching.

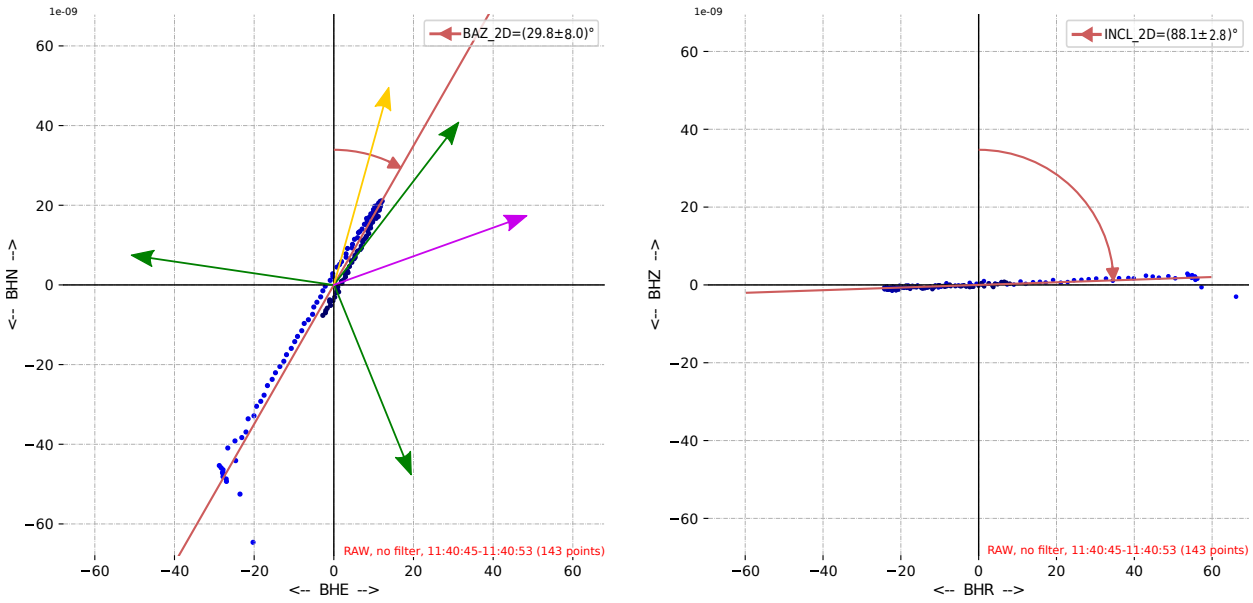

Figure S5-2. Polarization plot of a VBB glitch (glitch 14 in Table S5-1). Left, horizontal plane; right, radial-vertical plane. The apparent particle motion is highly linear (rectilinearity>0.95) and confined within the horizontal plane. The glitch back-azimuth, *BAZ_2D*, is (29.8+8.0)° and pointing towards one foot of SEIS' leveling system located at 37°, suggesting a nano-settling of this foot into the surface according to glitch model (2). Green arrows=direction of feet of SEIS' leveling system; yellow arrow=direction of tether connection between SEIS and the InSight lander (also direction of Load Shunt Assembly, LSA); purple arrow=direction of HP^3 instrument.

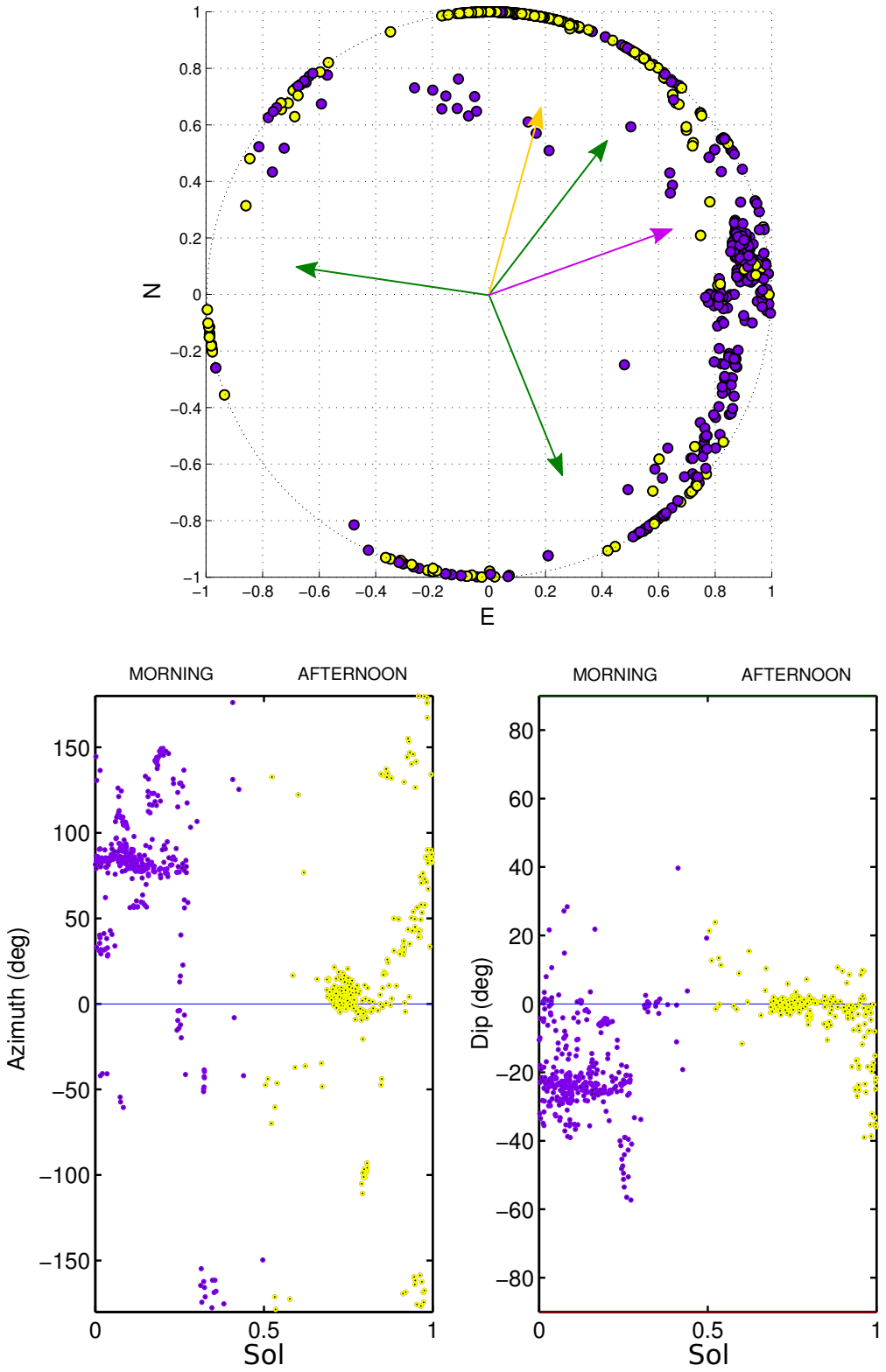

Figure S5-3. Top: Polarization plot of recorded VBB glitches over a period of 21 days in April 2019. Most polarizations are near horizontal with those from the East dipping at 20-30°. Purple (predominantly easterly) occur in morning; yellow (predominantly northerly) in afternoon. Colored arrows, same as in Fig. S5-2 left panel. Bottom: Azimuth and dip angles as a function of time of Martian day (sol), with color coding as in top.

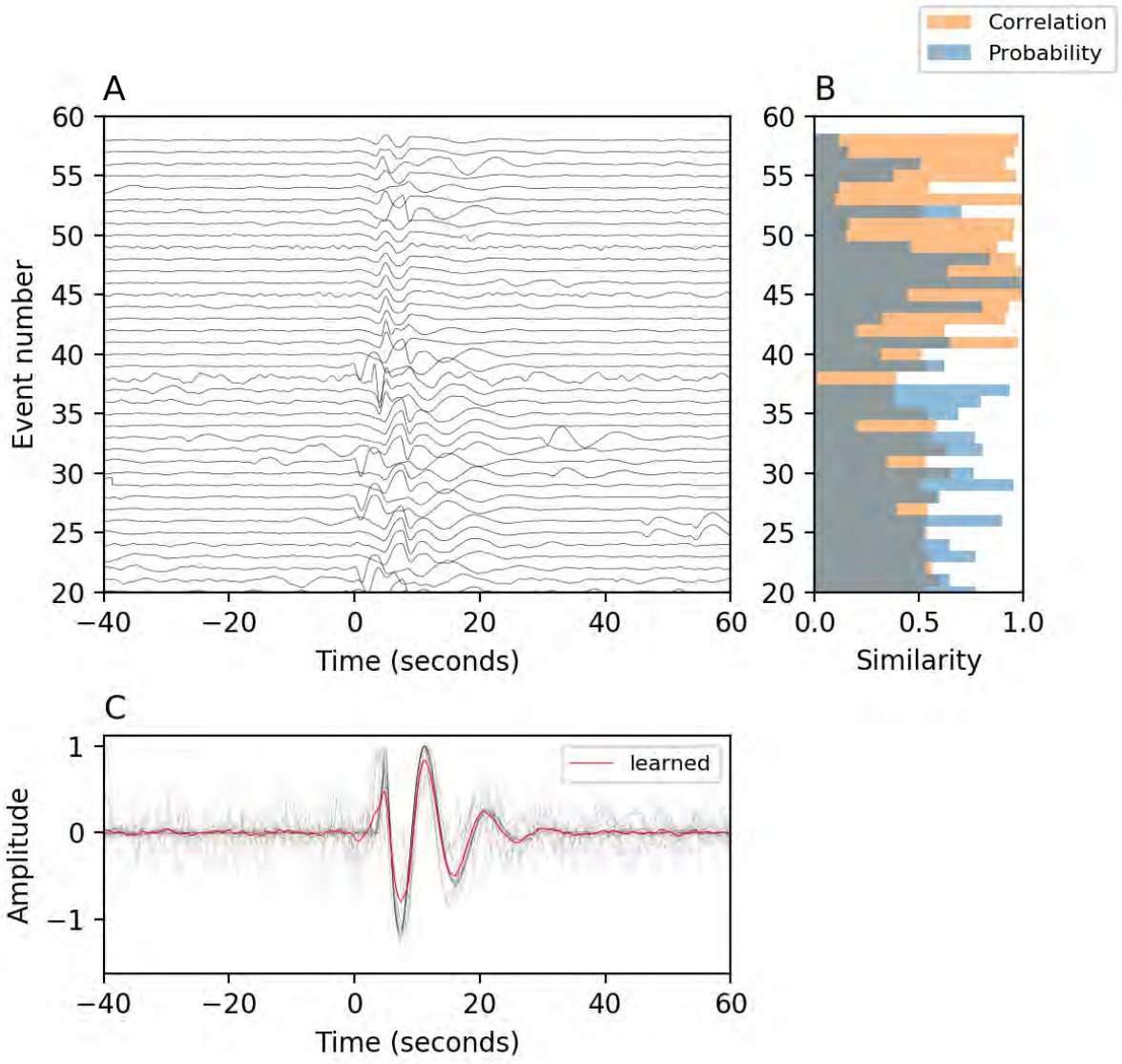

Figure S5-4. Learned waveform plot related to the glitch cluster computed via the Deep Scattering Network approach. Upper left: aligned glitch waveforms that were extracted. Upper right: correlations and similarities amongst the extracted glitches. Bottom: superposed glitch waveforms compared to the learned glitch waveform (derivative plus Butterworth band-pass filtered between 0.01Hz-0.9Hz).

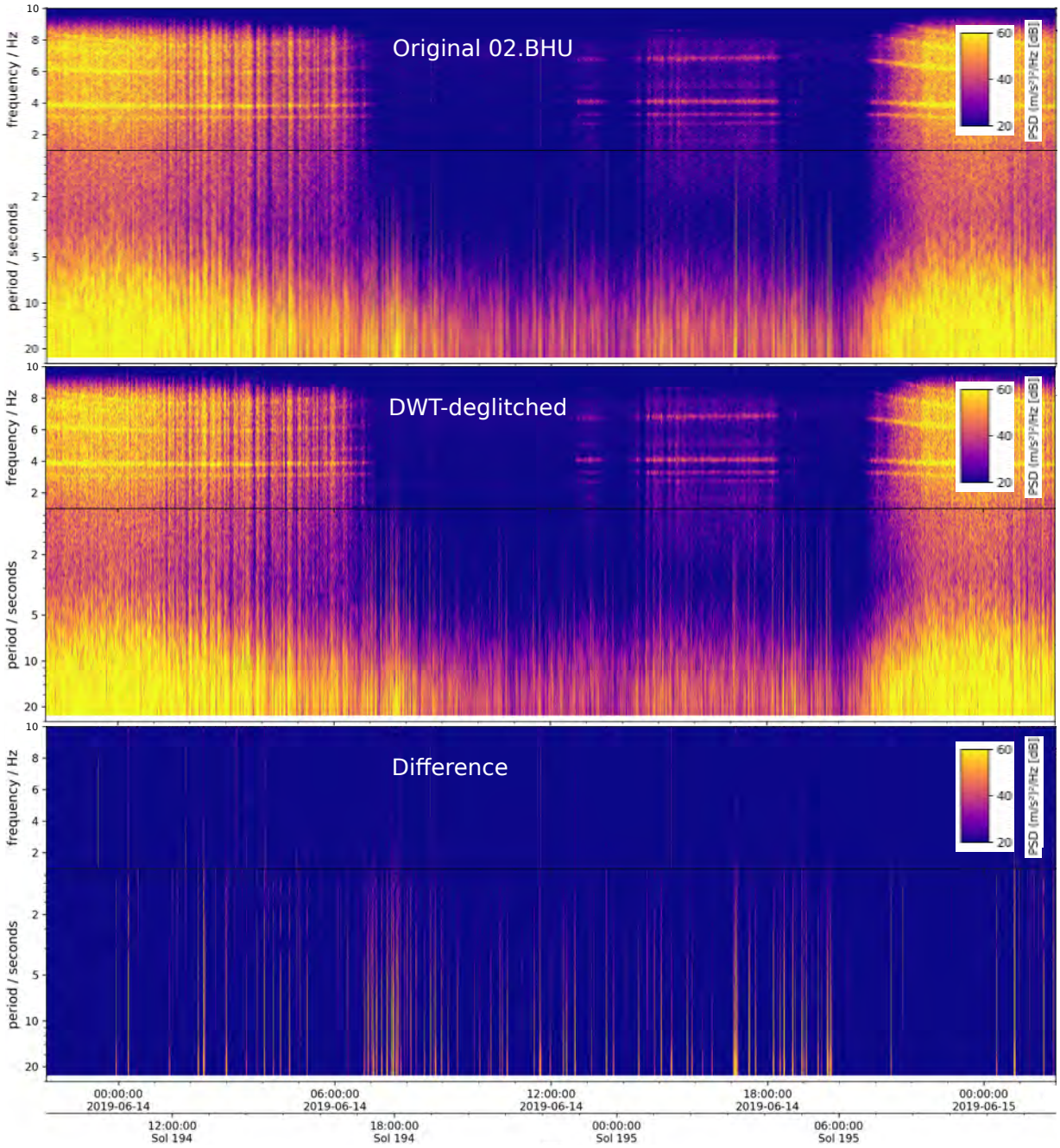

Figure S5-5. Spectrograms from UTC 2019-06-13, 10 p.m. to 2019-06-15, 2 a.m. (parts of sols 194 and 195). Top: original RAW data of VBB U-component. Middle: same as top, but with glitches removed/attenuated using the Discrete Wavelet Transform (DWT, see text for details). Bottom: Difference between top and middle panel showing that many, but not all, glitches have been removed/attenuated, especially in the lower frequency ranges.

Supplement Tables

Model A1

Depth (m)	Vp (m/s)	Vs (m/s)	Rho (kg/m3)
0	104,01	59,85	1172,38
0,1	116,05	66,78	1175,94
0,2	125,22	72,05	1179,36
0,3	132,74	76,38	1182,65
0,4	139,19	80,09	1185,82
0,5	144,86	83,36	1188,87
0,6	149,95	86,29	1191,81
0,7	154,59	88,96	1194,66
0,8	158,85	91,41	1197,4
0,9	162,81	93,69	1200,05
1	166,51	95,82	1202,61
1 to 10	750	316,23	2600

Model A2

Depth (m)	Vp (m/s)	Vs (m/s)	Rho (kg/m3)
0	107,07	61,62	1174,34
0,1	119,42	68,73	1177,91
0,2	128,82	74,14	1181,33
0,3	136,53	78,58	1184,63
0,4	143,13	82,38	1187,8
0,5	148,95	85,72	1190,86
0,6	154,16	88,73	1193,81
0,7	158,91	91,46	1196,66
0,8	163,27	93,97	1199,41
0,9	167,33	96,3	1202,06
1	171,11	98,48	1204,63
1,1	174,67	100,53	1207,11
1,2	178,03	102,47	1209,51
1,3	181,22	104,3	1211,84
1,4	184,26	106,05	1214,09
1,5	187,16	107,72	1216,28
1,5 to 10	770	324,66	2600

Model A3

Depth (m)	Vp (m/s)	Vs (m/s)	Rho (kg/m3)
0	108,99	62,91	1173,89
0,1	121,55	70,16	1177,46
0,2	131,1	75,68	1180,88
0,3	138,94	80,2	1184,18
0,4	145,66	84,08	1187,35
0,5	151,57	87,49	1190,41
0,6	156,87	90,55	1193,36
0,7	161,69	93,33	1196,2
0,8	166,13	95,89	1198,95
0,9	170,25	98,27	1201,6
1	174,1	100,49	1204,17
1,1	177,72	102,58	1206,65
1,2	181,14	104,56	1209,05
1,3	184,38	106,43	1211,38
1,4	187,46	108,21	1213,63

1,5	190,41	109,91	1215,81
1,6	193,23	111,54	1217,93
1,7	195,94	113,1	1219,98
1,8	198,54	114,6	1221,98
1,9	201,05	116,05	1223,91
2	203,48	117,45	1225,79
2 to 10	830	349,96	2600

Model A4

Depth (m)	Vp (m/s)	Vs (m/s)	Rho (kg/m3)
0	110,57	63,79	1175,58
0,1	123,28	71,12	1179,15
0,2	132,94	76,7	1182,58
0,3	140,86	81,27	1185,88
0,4	147,64	85,18	1189,06
0,5	153,61	88,62	1192,12
0,6	158,97	91,71	1195,07
0,7	163,84	94,52	1197,92
0,8	168,32	97,11	1200,67
0,9	172,48	99,51	1203,33
1	176,37	101,75	1205,9
1,1	180,02	103,86	1208,39
1,2	183,47	105,85	1210,79
1,3	186,74	107,74	1213,12
1,4	189,86	109,53	1215,37
1,5	192,83	111,25	1217,56
1,6	195,68	112,89	1219,68
1,7	198,41	114,47	1221,74
1,8	201,04	115,98	1223,73
1,9	203,57	117,44	1225,67
2	206,01	118,85	1227,56
2,1	208,38	120,22	1229,39
2,2	210,67	121,54	1231,16
2,3	212,89	122,82	1232,89
2,4	215,04	124,06	1234,58
2,5	217,14	125,27	1236,22
2,5 to 10	850	358,39	2600

Model A5

Depth (m)	Vp (m/s)	Vs (m/s)	Rho (kg/m3)
0	111,5	64,45	1176,22
0,1	124,27	71,84	1179,79
0,2	133,98	77,45	1183,22
0,3	141,94	82,05	1186,52
0,4	148,76	85,98	1189,7
0,5	154,75	89,45	1192,77
0,6	160,13	92,56	1195,72
0,7	165,02	95,38	1198,57
0,8	169,52	97,98	1201,33
0,9	173,69	100,4	1203,98
1	177,59	102,65	1206,55
1,1	181,26	104,77	1209,04
1,2	184,72	106,77	1211,45

1,3	188	108,67	1213,78
1,4	191,13	110,47	1216,03
1,5	194,11	112,19	1218,22
1,6	196,97	113,84	1220,34
1,7	199,71	115,43	1222,4
1,8	202,34	116,95	1224,4
1,9	204,88	118,42	1226,34
2	207,34	119,84	1228,22
2,1	209,71	121,21	1230,05
2,2	212	122,53	1231,83
2,3	214,23	123,82	1233,56
2,4	216,39	125,07	1235,25
2,5	218,49	126,28	1236,89
2,6	220,54	127,47	1238,49
2,7	222,53	128,62	1240,04
2,8	224,47	129,74	1241,56
2,9	226,36	130,83	1243,03
3	228,21	131,9	1244,47
3 to 10	870	366,82	2600

Model A6

Depth (m)	Vp (m/s)	Vs (m/s)	Rho (kg/m3)
0	112,06	64,87	1177,2
0,1	124,86	72,28	1180,77
0,2	134,59	77,91	1184,2
0,3	142,56	82,52	1187,51
0,4	149,38	86,47	1190,69
0,5	155,38	89,94	1193,75
0,6	160,76	93,06	1196,71
0,7	165,65	95,89	1199,57
0,8	170,16	98,5	1202,32
0,9	174,33	100,92	1204,98
1	178,23	103,18	1207,55
1,1	181,9	105,3	1210,04
1,2	185,36	107,3	1212,45
1,3	188,65	109,2	1214,78
1,4	191,77	111,01	1217,04
1,5	194,75	112,74	1219,23
1,6	197,61	114,39	1221,35
1,7	200,35	115,98	1223,41
1,8	202,98	117,5	1225,41
1,9	205,52	118,97	1227,35
2	207,98	120,39	1229,24
2,1	210,35	121,77	1231,07
2,2	212,64	123,1	1232,85
2,3	214,87	124,38	1234,59
2,4	217,03	125,63	1236,27
2,5	219,13	126,85	1237,91
2,6	221,17	128,03	1239,51
2,7	223,16	129,19	1241,07
2,8	225,1	130,31	1242,58
2,9	226,99	131,4	1244,06

3	228,84	132,47	1245,5
3,1	230,65	133,52	1246,91
3,2	232,41	134,54	1248,28
3,3	234,14	135,54	1249,62
3,4	235,83	136,52	1250,92
3,5	237,49	137,48	1252,2
3,5 to 10	910	383,69	2600

Model A7

Depth (m)	Vp (m/s)	Vs (m/s)	Rho (kg/m3)
0	112,98	65,37	1179,2
0,1	125,85	72,82	1182,77
0,2	135,62	78,47	1186,21
0,3	143,63	83,1	1189,52
0,4	150,47	87,06	1192,71
0,5	156,5	90,55	1195,78
0,6	161,9	93,67	1198,75
0,7	166,81	96,52	1201,6
0,8	171,32	99,13	1204,36
0,9	175,51	101,55	1207,03
1	179,42	103,82	1209,61
1,1	183,1	105,94	1212,1
1,2	186,57	107,95	1214,51
1,3	189,86	109,86	1216,85
1,4	193	111,67	1219,11
1,5	195,99	113,4	1221,3
1,6	198,85	115,06	1223,43
1,7	201,6	116,64	1225,49
1,8	204,24	118,17	1227,5
1,9	206,78	119,65	1229,44
2	209,24	121,07	1231,33
2,1	211,61	122,44	1233,16
2,2	213,91	123,77	1234,95
2,3	216,14	125,06	1236,68
2,4	218,31	126,32	1238,37
2,5	220,41	127,53	1240,02
2,6	222,46	128,72	1241,62
2,7	224,45	129,87	1243,18
2,8	226,4	131	1244,7
2,9	228,29	132,09	1246,18
3	230,14	133,16	1247,62
3,1	231,95	134,21	1249,03
3,2	233,72	135,23	1250,4
3,3	235,45	136,23	1251,74
3,4	237,14	137,21	1253,05
3,5	238,8	138,17	1254,33
3,6	240,43	139,11	1255,58
3,7	242,02	140,03	1256,8
3,8	243,58	140,94	1257,99
3,9	245,12	141,83	1259,15
4	246,63	142,7	1260,29
4 to 10	930	392,12	2600

Model A8

Depth (m)	Vp (m/s)	Vs (m/s)	Rho (kg/m3)
0	113,26	65,5	1174,84
0,1	126,13	72,94	1178,41
0,2	135,9	78,6	1181,83
0,3	143,92	83,23	1185,13
0,4	150,77	87,2	1188,31
0,5	156,81	90,68	1191,37
0,6	162,21	93,81	1194,32
0,7	167,13	96,66	1197,17
0,8	171,66	99,27	1199,92
0,9	175,85	101,7	1202,57
1	179,78	103,97	1205,14
1,1	183,46	106,1	1207,62
1,2	186,94	108,11	1210,03
1,3	190,24	110,02	1212,35
1,4	193,38	111,83	1214,61
1,5	196,37	113,57	1216,79
1,6	199,24	115,22	1218,91
1,7	201,99	116,82	1220,97
1,8	204,64	118,35	1222,96
1,9	207,19	119,82	1224,9
2	209,66	121,25	1226,78
2,1	212,04	122,62	1228,61
2,2	214,34	123,96	1230,39
2,3	216,58	125,25	1232,12
2,4	218,75	126,51	1233,8
2,5	220,86	127,73	1235,44
2,6	222,91	128,91	1237,03
2,7	224,91	130,07	1238,59
2,8	226,86	131,19	1240,1
2,9	228,76	132,29	1241,57
3	230,61	133,37	1243,01
3,1	232,43	134,42	1244,41
3,2	234,2	135,44	1245,78
3,3	235,93	136,44	1247,12
3,4	237,63	137,42	1248,42
3,5	239,29	138,39	1249,7
3,6	240,92	139,33	1250,94
3,7	242,52	140,25	1252,15
3,8	244,09	141,16	1253,34
3,9	245,63	142,05	1254,5
4	247,14	142,92	1255,64
4,1	248,62	143,78	1256,75
4,2	250,08	144,63	1257,83
4,3	251,52	145,46	1258,89
4,4	252,93	146,27	1259,93
4,5	254,31	147,07	1260,95
4,5 to 10	990	417,42	2600

Model A9

Depth (m)	Vp (m/s)	Vs (m/s)	Rho (kg/m3)

0	113,6	65,95	1179,23
0,1	126,49	73,43	1182,81
0,2	136,27	79,1	1186,25
0,3	144,28	83,76	1189,56
0,4	151,13	87,73	1192,75
0,5	157,15	91,23	1195,82
0,6	162,55	94,37	1198,78
0,7	167,47	97,22	1201,64
0,8	171,98	99,84	1204,4
0,9	176,17	102,27	1207,07
1	180,08	104,54	1209,64
1,1	183,76	106,68	1212,14
1,2	187,23	108,69	1214,55
1,3	190,52	110,6	1216,88
1,4	193,65	112,42	1219,15
1,5	196,64	114,16	1221,34
1,6	199,5	115,82	1223,47
1,7	202,24	117,41	1225,53
1,8	204,88	118,94	1227,53
1,9	207,43	120,42	1229,48
2	209,88	121,84	1231,37
2,1	212,25	123,22	1233,2
2,2	214,55	124,56	1234,99
2,3	216,78	125,85	1236,72
2,4	218,94	127,11	1238,41
2,5	221,05	128,33	1240,05
2,6	223,09	129,51	1241,66
2,7	225,08	130,67	1243,21
2,8	227,02	131,8	1244,73
2,9	228,92	132,9	1246,21
3	230,76	133,97	1247,66
3,1	232,57	135,02	1249,07
3,2	234,34	136,04	1250,44
3,3	236,06	137,05	1251,78
3,4	237,75	138,03	1253,09
3,5	239,41	138,99	1254,37
3,6	241,03	139,93	1255,61
3,7	242,63	140,86	1256,83
3,8	244,19	141,76	1258,03
3,9	245,72	142,65	1259,19
4	247,22	143,53	1260,33
4,1	248,7	144,39	1261,44
4,2	250,16	145,23	1262,53
4,3	251,58	146,06	1263,6
4,4	252,99	146,87	1264,64
4,5	254,37	147,68	1265,66
4,6	255,73	148,47	1266,66
4,7	257,07	149,24	1267,64
4,8	258,39	150,01	1268,6
4,9	259,69	150,76	1269,54
5	260,97	151,51	1270,47

5 to 10	1030	434,29	2600

Supplement Table 1 : Nine preliminary models with increasing depth for the regolith to bedrock discontinuity from inversion results jointly made with HP3 and compliance data (models A). Depths are 1m, 1.5m, 2m, 2.5m, 3m, 3.5m, 4m, 4.5m, 5m. Depth(z), Vp(z), Vs(z) and $\rho(z)$ are given in first to forth columns above the bedrock layer assumed homogeneous below the transition.

Model B1

Depth (m)	Vp (m/s)	Vs (m/s)	Rho (kg/m3)
0	130	75	1400
0,1	130	75	1400
0,1	155,36	89,27	1172,67
0,2	170,37	97,9	1176,08
0,3	182,86	105,08	1179,36
0,4	193,68	111,3	1182,52
0,5	203,3	116,82	1185,57
0,6	211,99	121,82	1188,5
0,7	219,96	126,4	1191,34
0,8	227,33	130,63	1194,07
0,9	234,21	134,58	1196,72
1	240,67	138,3	1199,27
1 to 10	690	290,93	2600

Model B2

Depth (m)	Vp (m/s)	Vs (m/s)	Rho (kg/m3)
0	130	75	1400
0,1	130	75	1400
0,1	165,97	95,17	1173,86
0,2	182,02	104,37	1177,27
0,3	195,38	112,03	1180,56
0,4	206,94	118,66	1183,72
0,5	217,22	124,55	1186,77
0,6	226,51	129,88	1189,71
0,7	235,02	134,76	1192,54
0,8	242,9	139,28	1195,28
0,9	250,25	143,5	1197,93
1	257,16	147,46	1200,49
1,1	263,68	151,19	1202,96
1,2	269,86	154,74	1205,35
1,3	275,74	158,11	1207,67
1,4	281,37	161,34	1209,92
1,5	286,75	164,42	1212,1
1,5 to 10	710	299,36	2600

Model B3

Depth (m)	Vp (m/s)	Vs (m/s)	Rho (kg/m3)
0	130	75	1400
0,1	130	75	1400
0,1	172,46	99,34	1175,86
0,2	189,15	108,95	1179,28
0,3	203,04	116,96	1182,57
0,4	215,06	123,88	1185,74
0,5	225,75	130,04	1188,8
0,6	235,41	135,6	1191,74
0,7	244,26	140,7	1194,58
0,8	252,45	145,42	1197,33
0,9	260,09	149,82	1199,98
1	267,27	153,96	1202,54
1,1	274,05	157,86	1205,02
1,2	280,47	161,56	1207,42
1,3	286,59	165,09	1209,74

1,4	292,43	168,45	1211,99
1,5	298,03	171,68	1214,17
1,6	303,41	174,78	1216,28
1,7	308,59	177,76	1218,33
1,8	313,58	180,64	1220,32
1,9	318,41	183,41	1222,26
2	323,08	186,11	1224,13
2 to 10	730	307,8	2600

Model B4

Depth (m)	Vp (m/s)	Vs (m/s)	Rho (kg/m3)
0	130	75	1400
0,1	130	75	1400
0,1	176,38	101,65	1178,03
0,2	193,47	111,5	1181,45
0,3	207,69	119,69	1184,75
0,4	220	126,79	1187,93
0,5	230,93	133,09	1190,99
0,6	240,82	138,79	1193,94
0,7	249,88	144,01	1196,78
0,8	258,26	148,84	1199,53
0,9	266,08	153,35	1202,19
1	273,43	157,58	1204,75
1,1	280,36	161,57	1207,24
1,2	286,94	165,36	1209,64
1,3	293,2	168,97	1211,96
1,4	299,18	172,42	1214,22
1,5	304,91	175,72	1216,4
1,6	310,41	178,89	1218,52
1,7	315,71	181,95	1220,57
1,8	320,82	184,89	1222,57
1,9	325,75	187,74	1224,51
2	330,53	190,49	1226,39
2,1	335,17	193,16	1228,22
2,2	339,66	195,75	1229,99
2,3	344,03	198,27	1231,72
2,4	348,29	200,72	1233,4
2,5	352,43	203,11	1235,04
2,5 to 10	770	324,66	2600

Model B5

Depth (m)	Vp (m/s)	Vs (m/s)	Rho (kg/m3)
0	130	75	1400
0,1	130	75	1400
0,1	178,84	103,37	1174,73
0,2	196,14	113,37	1178,14
0,3	210,54	121,69	1181,43
0,4	223,01	128,9	1184,6
0,5	234,08	135,3	1187,65
0,6	244,1	141,09	1190,59
0,7	253,27	146,39	1193,43
0,8	261,77	151,3	1196,17
0,9	269,69	155,88	1198,82

1	277,13	160,18	1201,38
1,1	284,16	164,24	1203,85
1,2	290,82	168,09	1206,25
1,3	297,16	171,76	1208,57
1,4	303,22	175,26	1210,82
1,5	309,03	178,61	1212,99
1,6	314,6	181,84	1215,11
1,7	319,97	184,94	1217,15
1,8	325,15	187,93	1219,14
1,9	330,15	190,82	1221,07
2	334,99	193,62	1222,95
2,1	339,69	196,34	1224,77
2,2	344,24	198,97	1226,55
2,3	348,67	201,53	1228,27
2,4	352,98	204,02	1229,95
2,5	357,18	206,44	1231,58
2,6	361,27	208,81	1233,17
2,7	365,26	211,12	1234,72
2,8	369,16	213,37	1236,23
2,9	372,97	215,57	1237,7
3	376,7	217,73	1239,13
3 to 10	790	333,09	2600

Model B6

Depth (m)	Vp (m/s)	Vs (m/s)	Rho (kg/m3)
0	130	75	1400
0,1	130	75	1400
0,1	181,22	104,82	1179,61
0,2	198,8	114,98	1183,04
0,3	213,42	123,44	1186,35
0,4	226,07	130,76	1189,52
0,5	237,32	137,26	1192,59
0,6	247,48	143,14	1195,54
0,7	256,79	148,53	1198,39
0,8	265,41	153,51	1201,14
0,9	273,45	158,16	1203,8
1	281	162,53	1206,37
1,1	288,13	166,65	1208,86
1,2	294,89	170,56	1211,27
1,3	301,32	174,28	1213,6
1,4	307,47	177,84	1215,85
1,5	313,36	181,24	1218,04
1,6	319,01	184,51	1220,16
1,7	324,46	187,66	1222,22
1,8	329,71	190,7	1224,21
1,9	334,79	193,64	1226,15
2	339,7	196,48	1228,04
2,1	344,46	199,23	1229,87
2,2	349,08	201,91	1231,65
2,3	353,57	204,5	1233,38
2,4	357,95	207,03	1235,06
2,5	362,2	209,49	1236,7

2,6	366,35	211,89	1238,3
2,7	370,4	214,24	1239,85
2,8	374,36	216,52	1241,37
2,9	378,22	218,76	1242,85
3	382	220,95	1244,29
3,1	385,7	223,09	1245,69
3,2	389,33	225,18	1247,06
3,3	392,88	227,24	1248,4
3,4	396,36	229,25	1249,7
3,5	399,78	231,23	1250,98
3,5 to 10	810	341,53	2600

Model B7

Depth (m)	Vp (m/s)	Vs (m/s)	Rho (kg/m3)
0	130	75	1400
0,1	130	75	1400
0,1	184,93	107	1179,41
0,2	202,86	117,38	1182,84
0,3	217,78	126,01	1186,14
0,4	230,7	133,48	1189,32
0,5	242,17	140,12	1192,38
0,6	252,54	146,12	1195,33
0,7	262,04	151,62	1198,18
0,8	270,83	156,71	1200,93
0,9	279,04	161,45	1203,59
1	286,74	165,91	1206,16
1,1	294,01	170,12	1208,65
1,2	300,91	174,11	1211,05
1,3	307,48	177,91	1213,38
1,4	313,75	181,54	1215,64
1,5	319,76	185,01	1217,83
1,6	325,53	188,35	1219,95
1,7	331,09	191,57	1222
1,8	336,45	194,67	1224
1,9	341,63	197,67	1225,94
2	346,64	200,57	1227,82
2,1	351,5	203,38	1229,65
2,2	356,22	206,11	1231,43
2,3	360,8	208,76	1233,16
2,4	365,26	211,34	1234,85
2,5	369,6	213,85	1236,49
2,6	373,84	216,3	1238,08
2,7	377,97	218,69	1239,64
2,8	382,01	221,03	1241,15
2,9	385,95	223,31	1242,63
3	389,81	225,54	1244,07
3,1	393,59	227,73	1245,47
3,2	397,29	229,87	1246,84
3,3	400,91	231,97	1248,18
3,4	404,46	234,02	1249,48
3,5	407,95	236,04	1250,76
3,6	411,37	238,02	1252

3,7	414,73	239,96	1253,22
3,8	418,03	241,88	1254,4
3,9	421,28	243,75	1255,57
4	424,47	245,6	1256,7
4 to 10	830	349,96	2600

Model B8

Depth (m)	Vp (m/s)	Vs (m/s)	Rho (kg/m3)
0	130	75	1400
0,1	130	75	1400
0,1	185,92	107,57	1177,72
0,2	203,93	117,99	1181,14
0,3	218,91	126,66	1184,44
0,4	231,89	134,17	1187,61
0,5	243,42	140,84	1190,67
0,6	253,84	146,87	1193,62
0,7	263,38	152,39	1196,47
0,8	272,22	157,51	1199,21
0,9	280,46	162,28	1201,87
1	288,2	166,76	1204,43
1,1	295,51	170,98	1206,92
1,2	302,44	174,99	1209,32
1,3	309,04	178,81	1211,64
1,4	315,35	182,46	1213,9
1,5	321,38	185,95	1216,08
1,6	327,18	189,31	1218,2
1,7	332,77	192,54	1220,25
1,8	338,15	195,66	1222,25
1,9	343,36	198,67	1224,18
2	348,4	201,58	1226,06
2,1	353,28	204,41	1227,89
2,2	358,02	207,15	1229,67
2,3	362,63	209,82	1231,4
2,4	367,11	212,41	1233,08
2,5	371,47	214,93	1234,71
2,6	375,73	217,4	1236,31
2,7	379,88	219,8	1237,86
2,8	383,94	222,15	1239,37
2,9	387,9	224,44	1240,85
3	391,78	226,68	1242,28
3,1	395,57	228,88	1243,69
3,2	399,29	231,03	1245,05
3,3	402,93	233,14	1246,39
3,4	406,51	235,2	1247,69
3,5	410,01	237,23	1248,96
3,6	413,45	239,22	1250,21
3,7	416,83	241,18	1251,42
3,8	420,14	243,1	1252,61
3,9	423,41	244,98	1253,77
4	426,61	246,84	1254,9
4,1	429,77	248,66	1256,01
4,2	432,87	250,46	1257,1

4,3	435,93	252,23	1258,16
4,4	438,94	253,97	1259,2
4,5	441,9	255,69	1260,21
4,5 to 10	850	358,39	2600

Model B9

Depth (m)	Vp (m/s)	Vs (m/s)	Rho (kg/m3)
0	130	75	1400
0,1	130	75	1400
0,1	187,06	108,56	1177,69
0,2	205,18	119,07	1181,11
0,3	220,26	127,82	1184,41
0,4	233,32	135,4	1187,58
0,5	244,91	142,13	1190,64
0,6	255,4	148,22	1193,59
0,7	265	153,79	1196,44
0,8	273,89	158,95	1199,18
0,9	282,19	163,76	1201,84
1	289,98	168,28	1204,4
1,1	297,33	172,55	1206,89
1,2	304,3	176,6	1209,29
1,3	310,94	180,45	1211,61
1,4	317,29	184,13	1213,87
1,5	323,36	187,66	1216,05
1,6	329,2	191,04	1218,17
1,7	334,82	194,3	1220,22
1,8	340,24	197,45	1222,22
1,9	345,47	200,49	1224,15
2	350,54	203,43	1226,03
2,1	355,45	206,28	1227,86
2,2	360,22	209,05	1229,64
2,3	364,86	211,74	1231,36
2,4	369,37	214,35	1233,05
2,5	373,76	216,9	1234,68
2,6	378,04	219,39	1236,28
2,7	382,22	221,81	1237,83
2,8	386,3	224,18	1239,34
2,9	390,29	226,5	1240,82
3	394,19	228,76	1242,25
3,1	398,01	230,98	1243,65
3,2	401,75	233,15	1245,02
3,3	405,41	235,27	1246,36
3,4	409,01	237,36	1247,66
3,5	412,53	239,41	1248,93
3,6	415,99	241,41	1250,18
3,7	419,39	243,39	1251,39
3,8	422,73	245,32	1252,58
3,9	426,01	247,23	1253,74
4	429,24	249,1	1254,87
4,1	432,41	250,94	1255,98
4,2	435,54	252,75	1257,06
4,3	438,61	254,54	1258,13

4,4	441,64	256,3	1259,16
4,5	444,62	258,03	1260,18
4,6	447,56	259,73	1261,18
4,7	450,46	261,41	1262,15
4,8	453,32	263,07	1263,11
4,9	456,13	264,71	1264,05
5	458,91	266,32	1264,96
5 to 10	870	366,82	2600

Supplement Table 2 : Nine preliminary models with increasing depth for the regolith to bedrock discontinuity from inversion results jointly made with only compliance data (models B), assuming a 10 cm Vp=130 m/s surface-crust layer. Depths are 1m, 1.5m, 2m, 2.5m, 3m, 3.5m, 4m, 4.5m, 5m. Depth(z) , Vp(z), Vs(z) and ρ(z) are given in first to forth column above the bedrock layer assumed homogeneous below the transition.

	parameter	**minimum value**	**maximum value**	**best fit**
layer 1	S-wave velocity	1.76 km/s	2.11 km/s	1.97 km/s
	thickness	7.87 km	11.38 km	9.65 km
	vp/vs ratio	1,60	2,10	1,823
halfspace	S-wave velocity	2.28 km/s	2.86 km/s	2.69 km/s
	vp/vs ratio	1,60	2,10	2,095

Supplement Table 3: Minimum, Maximum and best fit values for the two layers model found from Receiver-Function analysis